AD
A/03434

‖‖‖ 1.0   ‖4.5 ‖2.8 ‖2.5
           ‖5.0 ‖3.2 ‖2.2
           ‖5.6 ‖3.6
           ‖4.0 ‖2.0
‖‖‖ 1.1
                        ‖1.8
‖‖‖1.25 ‖‖1.4 ‖1.6

LEVEL II

AD A103434

ANALYSIS AND DESIGN OF SUPERSONIC AIRCRAFT BASED ON
INVISCID NONLINEAR EULERIAN EQUATIONS

Part I Rotational Euler Solutions with Explicit Shock Fitting

GRUMMAN AEROSPACE CORPORATION
BETHPAGE, NEW YORK 11714

DTIC
ELECTE
AUG 2 8 1981
S
D
H
15

OCTOBER 1980

FLIGHT DYNAMICS LABORATORY
AIR FORCE WRIGHT AERONAUTICAL LABORATORIES
AIR FORCE SYSTEMS COMMAND
WRIGHT-PATTERSON AIR FORCE BASE, OHIO 45433

80 8 28 043

NOTICE

When Government drawings, specifications, or other data are used for any purpose other than in connection with a definitely related Government procurement operation, the United States Government thereby incurs no responsibility nor any obligation whatsoever; and the fact that the Government may have formulated, furnished, or in any way supplied the said drawings, specifications, or other data, is not to be regarded by implication or otherwise as in any manner licensing the holder or any other person or corporation, or conveying any rights or permission to manufacture, use, or sell any patented invention that may in any way be related thereto.

This report has been reviewed by the Office of Public Affairs (ASD/PA) and is releasable to the National Technical Information Service (NTIS). At NTIS, it will be available to the general public, including foreign nations.

This technical report has been reviewed and is approved for publication.

K.S. Nagaraj
Project Engineer

LOWELL C. KEEL, Maj, USAF
Ch, Aerodynamics & Airframe Branch
Aeromechanics Division

FOR THE COMMANDER

PETER J. BUTKEWICZ
Colonel, USAF
Chief, Aeromechanics Division

"If your address has changed, if you wish to be removed from our mailing list, or if the addressee is no longer employed by your organization please notify AFWAL/FIMM, W-PAFB, OH 45433 to help us maintain a current mailing list".

Copies of this report should not be returned unless return is required by security considerations, contractual obligations, or notice on a specific document.

REPORT DOCUMENTATION PAGE	READ INSTRUCTIONS BEFORE COMPLETING FORM

1. REPORT NUMBER AFWAL-TR-80-3110, Part I	2. GOVT ACCESSION NO. AD-A103 434	3. RECIPIENT'S CATALOG NUMBER

4. TITLE (and Subtitle) ANALYSIS AND DESIGN OF SUPERSONIC AIRCRAFT BASED ON INVISCID NONLINEAR EULERIAN EQUATIONS. Part I. Rotational Euler Solutions with Explicit Shock Fitting	5. TYPE OF REPORT & PERIOD COVERED Final Report 1 October 1977 — through 1 April 1979
	6. PERFORMING ORG. REPORT NUMBER RE-623

7. AUTHOR(s) M. J. Siclari F. Marconi	8. CONTRACT OR GRANT NUMBER(s) F33615-77-C-3126

9. PERFORMING ORGANIZATION NAME AND ADDRESS Grumman Aerospace Corporation Bethpage, New York 11714	10. PROGRAM ELEMENT, PROJECT, TASK AREA & WORK UNIT NUMBERS Project 2404 10 32

11. CONTROLLING OFFICE NAME AND ADDRESS Flight Dynamics Laboratory (AFWAL/FIM) Air Force Wright Aeronautical Laboratories Wright-Patterson Air Force Base, Ohio 45433	12. REPORT DATE October 1980
	13. NUMBER OF PAGES 108

14. MONITORING AGENCY NAME & ADDRESS(if different from Controlling Office)	15. SECURITY CLASS. (of this report) Unclassified
	15a. DECLASSIFICATION/DOWNGRADING SCHEDULE

16. DISTRIBUTION STATEMENT (of this Report)

Approved for public release; distribution unlimited.

17. DISTRIBUTION STATEMENT (of the abstract entered in Block 20, if different from Report)

18. SUPPLEMENTARY NOTES

19. KEY WORDS (Continue on reverse side if necessary and identify by block number)

Supersonic Flow   Conical Flow
Euler Equations   Computational Fluid Dynamics
Shock Fitting   Supersonic Wing Aerodynamics

20. ABSTRACT (Continue on reverse side if necessary and identify by block number)

A computer program has been developed to compute the inviscid supersonic flow over delta wings and smooth wing-body configurations. A second-order accurate predictor-corrector finite-difference scheme is used to integrate the three dimensional Euler equations in regions of continuous flow. Bow shock and crossflow-induced embedded shocks are explicitly computed as discontinuities which simultaneously satisfy the characteristic and the Rankine-Hugoniot conditions. In computing the flow about complex wing cross sections, the use of appropriate conformal mappings were an important factor in developing a computational mesh capable of resolving the large flow gradients that are inevitable in the vinicity of wing leading edges. Geometry programs were developed to supply the appropriate geometric boundary conditions necessary to compute complex wing cross sections.

DD FORM 1473   EDITION OF 1 NOV 55 IS OBSOLETE
1 JAN 73
S/N 0102-014-6501

406165

New starting solutions were developed that were more appropriate to thin-wing cross sections. In the initial stage of development, the flow about conical wings was computed for a two-fold purpose. Conical Euler solutions would be used as starting conditions for conical wing-bodies and three dimensional wings and the conical problem would uncover potential problem areas in the computation of these flows without the added complexity of geometrical variations. The conical problem led to the development of special techniques to resolve the vortical layer that inevitably develops on the body surface. Typical results are shown for subsonic and supersonic leading edge delta wings and wing-body combinations. These results are also compared to linearized and nonlinear potential flow theories as well as available experimental data.

FOREWORD

CONTENTS

LIST OF ILLUSTRATIONS

LIST OF ILLUSTRATIONS (contd)

SUMMARY

A computer program has been developed to compute the inviscid supersonic
flow over delta wings and smooth wing-body configurations. A second-order
accurate predictor-corrector finite-difference scheme is used to integrate the
three dimensional Euler equations in regions of continuous flow. Bow shock
and crossflow-induced embedded shocks are explicitly computed as discontinui-
ties which simultaneously satisfy the characteristic and the Rankine-Hugoniot
conditions. In computing the flow about complex wing cross sections, the use
of appropriate conformal mappings were an important factor in developing a
computational mesh capable of resolving the large flow gradients that are inevi-
table in the vicinity of wing leading edges.

Geometry programs were developed to supply the appropriate geometric
boundary conditions necessary to compute complex wing cross sections. New
starting solutions were developed that were more appropriate to thin-wing cross
sections.

In the initial stage of development, the flow about conical wings was com-
puted for a two-fold purpose. Conical Euler solutions would be used as start-
ing conditions for conical wing-bodies and three dimensional wings and the
conical problem would uncover potential problem areas in the computation of
these flows without the added complexity of geometrical variations.

The conical problem led to the development of special techniques to resolve
the vortical layer that inevitably develops on the body surface.

Typical results are shown for subsonic and supersonic leading edge delta
wings and wing-body combinations. These results are also compared to lin-
earized and nonlinear potential flow theories as well as available experimental
data.

ix

SECTION I

INTRODUCTION

The standard assumptions made in order to predict the flow about thin wings at supersonic Mach numbers and moderate angles of attack (i.e. linearized potential flow) preclude the prediction of some of the basic fluid dynamics of these flows. Specifically, the formation of supercritical crossflow regions in the vicinity of the leeward wing leading edge. The assumptions of small-perturbation linearized potential flow theory can not predict supercritical crossflow regions, and thus any embedded shocks which might result due to recompression. Consequently, aerodynamic design engineers who are keenly aware of of the shortcomings and restrictions of applying linearized design and analysis tools to supersonic problems avoid possible nonlinear areas by striving to contour their wings at design points (i.e. lift coefficients) that fall primarily within the realm of linearized flow (e.g. $C_L \sim .2$). Unfortunately, this becomes an increasingly difficult task as highly cambered wings are sometimes required to achieve specific design and maneuver goals. It has been found and noted in the past that optimum wings that have been designed with linearized methods often fall short of their design goals (Reference 1) when tested experimentally. These shortcomings have often been blamed on unaccounted-for viscous boundary layer effects. On the other hand, some very important inviscid aspects of the flow have been neglected (e.g., crossflow-induced embedded shocks). The nonlinear inviscid behavior of the flow can shed light on the boundary layer behavior (i.e. shock-induced boundary layer separation). Thus, with the somewhat unreliable predictability of linearized methods, experimental wind tunnel testing is currently the final and often expensive determinant in the design of a supersonic wing.

In Reference 2 and 3, a computer code was developed primarily for computing the three-dimensional inviscid hypersonic flow over space shuttle configurations by integrating the nonlinear Eulerian equations of motion and explicitly

1

computing shock waves. It was shown that pressure and force data could be successfully predicted for this type of vehicle, thus significantly reducing the amount of wind tunnel testing necessary in the vehicle development. It is the intent of the present study to apply procedures similar to those developed in Reference 3 to supersonic vehicles. The code described in Reference 3 contained several drawbacks in that it lacked sufficient geometric detail for modeling contemporary complex supersonic wing geometries. In addition, the procedure had never been tested on thin-wing geometries in supersonic flow where typically very large gradients of pressure and Mach number can be generated in the vicinity of wing leading edges. An important step in computing the flow about complex wings is to select the appropriate conformal mapping necessary to generate an accurate grid line or computational mesh arrangement in the transversel plane, perpendicular to the marching direction. This procedure was first used by Moretti (Reference 2) for three-dimensional flow and was shown to be a significant factor in generating accurate and reliable results.

SECTION II

PROBLEM DEFINITION

Figure 1 shows a sketch of the type of flow field under consideration. Initially, conical wings will be considered because of the geometrical simplification of reducing the full three-dimensional problem to only two spatial coordinates. In addition, the nature of conical geometries makes it possible to study the effect of cross sectional perturbations on the spanwise pressure distribution. In subsequent sections, the conical solutions to the Euler equations will be used as starting conditions for three-dimensional wings.

The nature of a conical flowfield is dominated by the "crossflow" Mach number. The crossflow velocity is defined to be that velocity that is tangential to a spherical surface whose origin is the apex of the conical wing. Figure 2 shows a sketch of the cross-sectional plane of a delta wing. At zero angle of attack, the crossflow about a symmetrical wing will stagnate at the wing leading edge (see Figure 2a), rapidly accelerate about the upper and lower surfaces and then stagnate at the upper and lower symmetry planes. At angles of attack greater than zero, the crossflow stagnation point moves slightly to the windward side of the leading edge. The resulting crossflow undergoes a larger expansion and can attain supercritical values on the upper surface, thus forming a supersonic crossflow region (see Figure 2b). The crossflow must stagnate in the leeward symmetry plane and, if the crossflow becomes sufficiently supercritical, a "crossflow shock" is generated on the upper surface or leeward side of the wing. The crossflow shock facilitates the turning of the three-dimensional velocity vector or streamline in the direction of the leeward symmetry plane, thus satisfying the symmetry plane crossflow stagnation boundary condition. The crossflow shock is a normal shock at the body in order to satisfy the flow tangency body boundary condition, thus delineating the supercritical crossflow region from its subcritical counterpart.

3
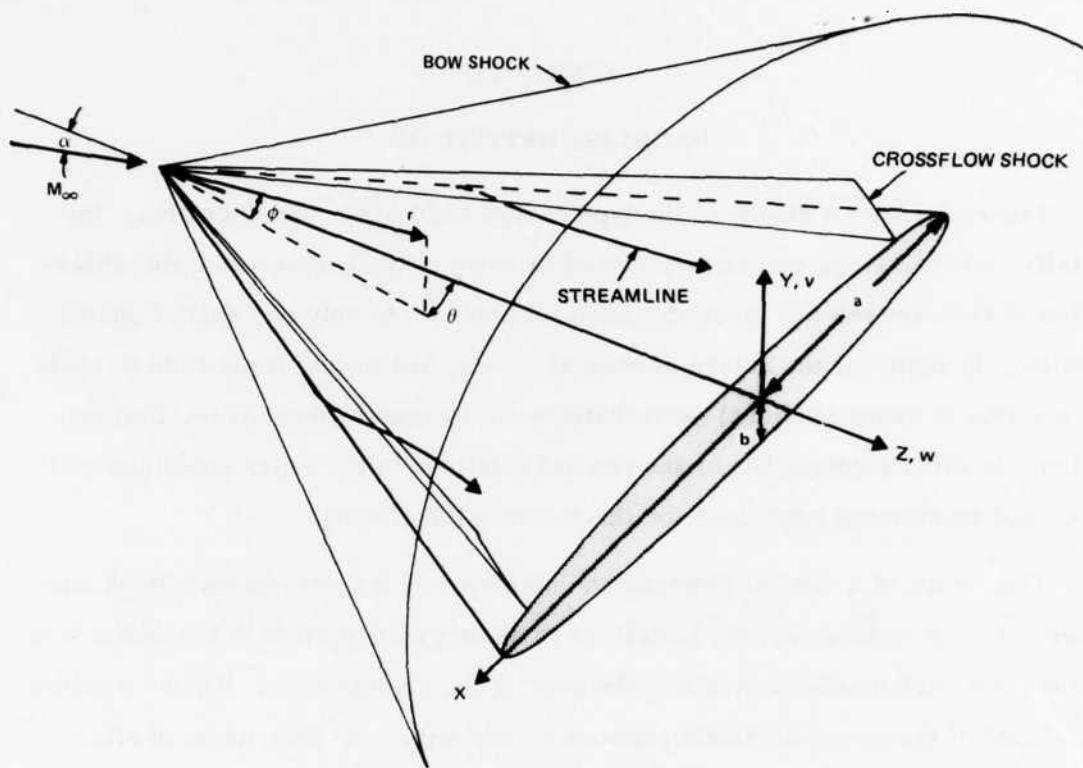
Figure 1   Sketch of Supersonic Flowfield About Elliptic Cone
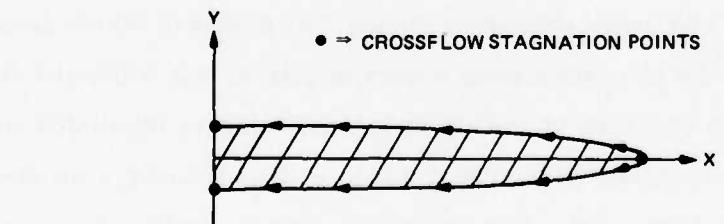
(a) ZERO ANGLE OF ATTACK
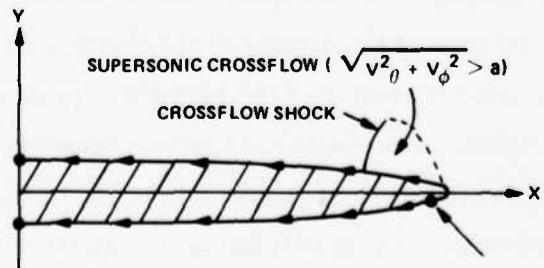
(b) ANGLES OF ATTACK GREATER THAN ZERO

Figure 2   Sketch of Crossflow Stagnation Streamlines and Supersonic Crossflow Region

R80-1248-001W

4

The problem of computing the external flow about a supersonic wing is completely defined by the wing geometry, the free stream Mach number and angle of attack, and an initial starting solution which satisfies the local boundary conditions. A finite difference marching technique can then be applied to integrate the governing partial differential equations in an assumed axial marching direction (Z). The only restriction is that the axial Mach number must remain supersonic and that the Courant-Friedrichs-Lewy (CFL) stability condition must be satisfied in marching from one station to another.

In order to apply the boundary condition at the wing surface (i.e., vanishing of the normal velocity), the surface and all its first derivatives must be defined. Therefore an analytic definition of the geometry is needed, with continuous first derivatives. The second derivatives of the body geometry appear explicitly in the present formulation of the problem, but continuity is not necessary.

The governing equations were defined in a Cartesian coordinate system, thus giving no special consideration to the conical flow problem. In the marching procedure each cross sectional geometry is mapped into a near circle, thus developing an accurate computational mesh. For the conical flow problem, the mappings exhibit conical similitude in the computational plane and thus the axial derivatives will vanish if a conical flow solution has been achieved.

5

SECTION III

COMPUTATIONAL GRID: CONFORMAL MAPPINGS

The definition of a computational grid is one of the most crucial steps in the building of a numerical technique. The concept of using conformal mappings to develop the computational mesh in three-dimensional supersonic flow problems was originally proposed by Moretti (Reference 2).

Three coordinate systems or spaces will be referred to: the physical space (x, y, z), a mapped space $(r, \theta, \mathfrak{z})$, and a computational space (X, Y, Z); see Figure 3. The coordinate system in the physical space is Cartesian and defines the three velocity components that are to be computed. The governing equations are written in the physical space and then all derivatives are transformed into the computational space where the mesh points are at uniform intervals ΔX, ΔY, ΔZ.

Each $\mathfrak{z}$ = constant plane in the mapped space is obtained by conformally mapping cross sections in the physical space into near circles in the mapped space. The region bounded by the body and the bow shock becomes an annulus in the mapped space. The corresponding computational space is obtained by normalizing the radial distance between body and shock (X-direction) and the circumferential distance between the two symmetry planes (Y-direction); see Figure 4. The mapped space serves three purposes. First, it distributes the body mesh points (which are evenly spaced in the computational plane) so that the necessary resolution is obtained in regions of large curvature where truncation error may otherwise become too large. Second, the mapping makes the body and bow shock positions single-value functions, $r = b\,(\theta, \mathfrak{z})$ and $r = \bar{c}\,(\theta, \mathfrak{z})$ in the mapped plane. Third, since shock waves embedded in the flow-field become mesh lines, an accurate and stable computation is contingent upon the shape of the crossflow shock not differing significantly from a $\theta =$ constant mesh line. This enables one to define a number of regions in the

6

(a) PHYSICAL SPACE

(b) MAPPED SPACE

(c) COMPUTATIONAL SPACE
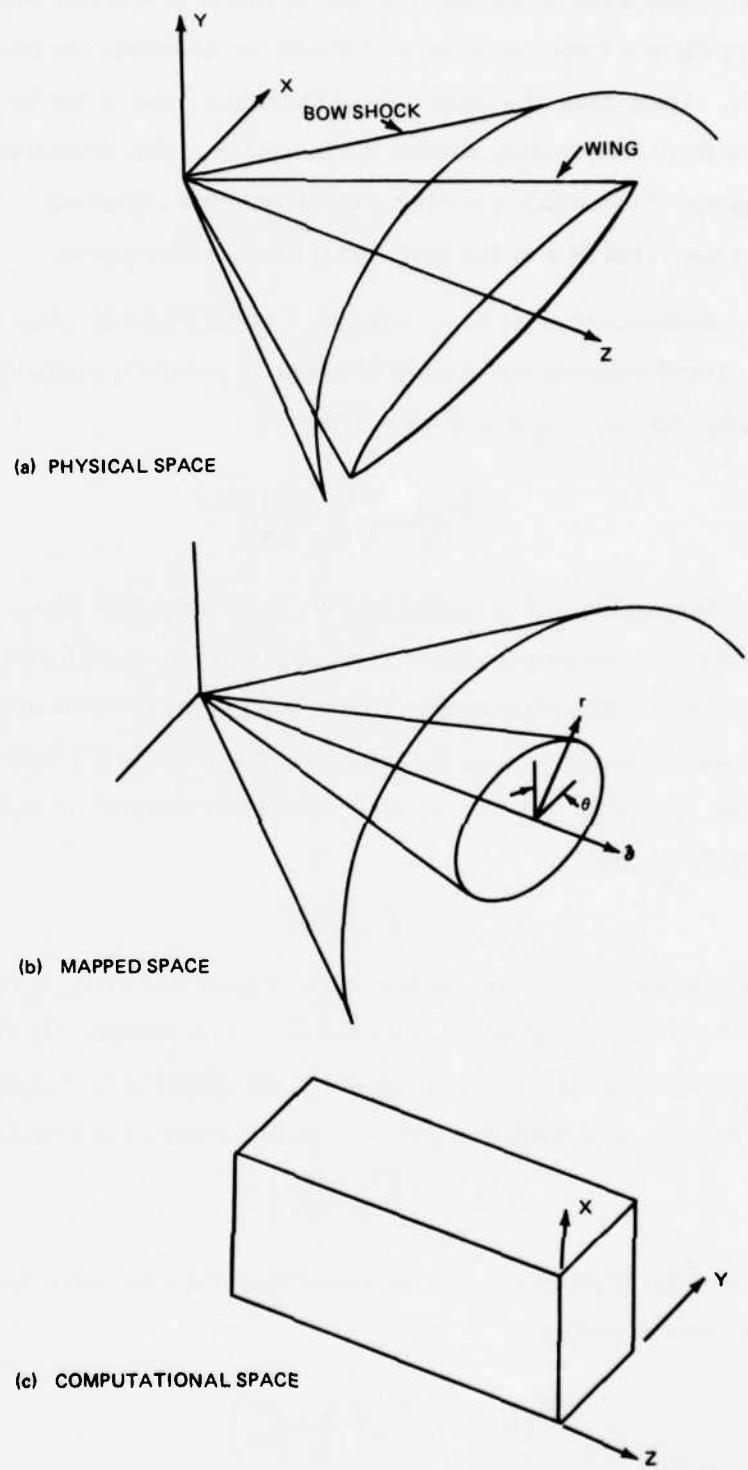
Figure 3 Three Spaces and Associated Coordinate Systems

R80-1248-002W

7

computational space when more than one shock exists in a cross section. The dotted lines in Figure 4 are extensions of shocks to complete the boundaries of these regions. The points on either side of these portions of the boundaries are allowed to pass information across the boundary. The crossflow surfaces (i.e., extensions of crossflow shocks) are defined as $\theta =$ constant. The constant taken is the value of θ at the last radial point on the shock.

Now, the transformation $(r, \theta, \mathfrak{d}) \rightarrow (x, y, z)$ is considered. The mapping that has been found suitable for cambered wings is simply a single Karman-Trefftz transformation, which may be written:

$$\frac{\zeta - 1}{\zeta + 1} = \left(\frac{W - W^*}{W + \overline{W}^*} \right)^{\delta / \pi} \tag{1}$$

where $\zeta = re^{i\theta}$ (mapped space variable) and $W = x + iy$ (physical space variable). W^* is the position of the singularity of the mapping in the physical space, $W^* = x^* + iy^*$ (Figure 5). The singularity of the mapping must be placed near the wing leading edge in order to map the wing cross section into a near circle. The singularity should be on the wing cross sectional camber or mean line; this condition defines y^* and

$$x^* = \sqrt{x_T{}^2 - R_c^2} \tag{2}$$

where $x_T =$ coordinate of the wing leading edge (Figure 5) and R_c is the radius of curvature of the wing leading edge. The power δ / π of equation (1) is, in general, the external angle of the corner of which the mapping is intended to eliminate. In the case of a blunt wing, $\delta = 2\pi$, and therefore equation (1) becomes

$$\frac{\zeta - 1}{\zeta + 1} = \left(\frac{W - W^*}{W + \overline{W}^*} \right)^2 \tag{3}$$

In order to compute W from ζ (i.e., to invert this mapping) care must be taken to choose the proper root of

$$\left(\frac{\zeta - 1}{\zeta + 1} \right)^{1/2} = \left(\frac{W - W^*}{W + \overline{W}^*} \right) \tag{4}$$

8
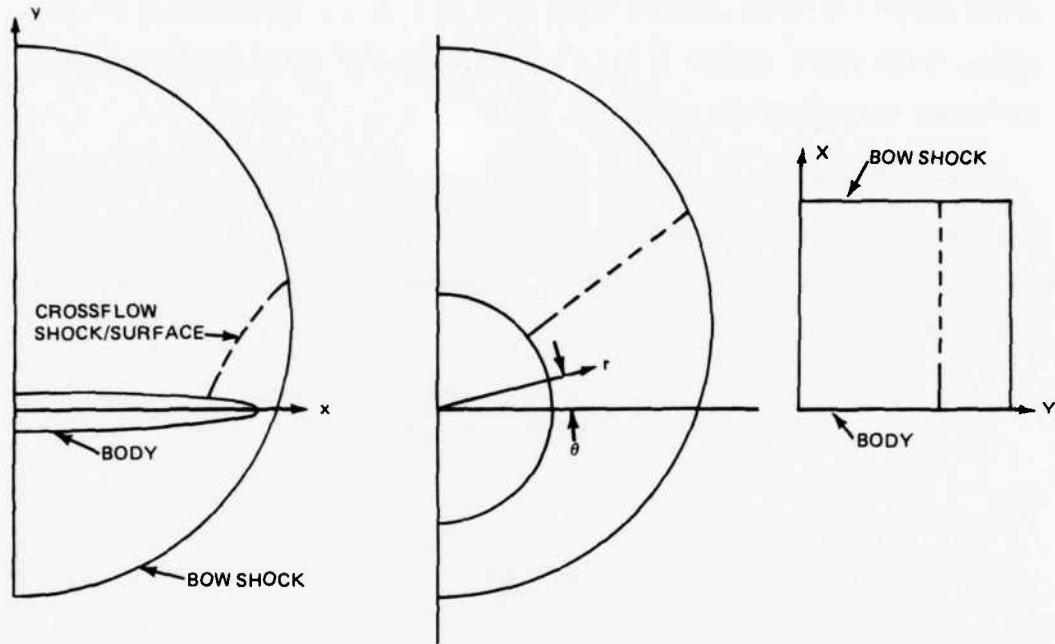
Figure 4   Cross Section in Three Spaces
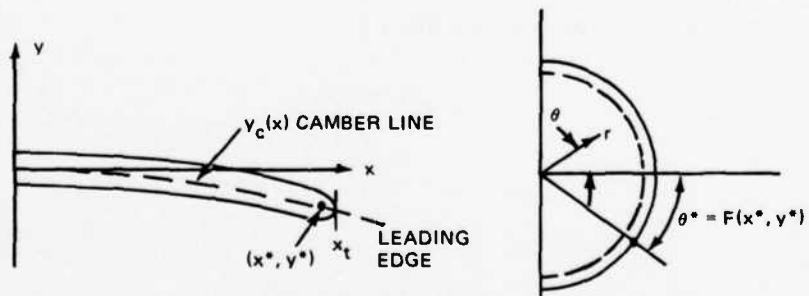
Figure 5   Conformal Mappings for Cambered Wing

The root selection was determined by first locating the singular point in the mapped space θ^* (Figure 5) and selecting the root of equation (4) such that points with $\theta > \theta^*$ in the mapped space have $y > y_c$ in the physical space (i.e., points on the upper surface of the wing in the mapped space are on the upper surface of the wing in the physical space).

In order to transform the derivatives in the governing equations from the physical space to the computational space, the first and second derivatives of all the transformations are needed. The derivatives r_x, r_y, θ_x, and θ_y can be calculated as follows:

$$W_\zeta = \frac{(\overline{W}^* + W^*)}{(\zeta + 1)(\zeta - 1)(W - W^*)(W + \overline{W}^*)} \tag{5}$$

and

$$\zeta_w = \frac{1}{W_\zeta} \tag{6}$$

If $\zeta = u + iv$, where $u = r\cos\theta$ and $v = r\sin\theta$, then

$$u_x = \mathrm{Re}(\zeta_w)$$

$$v_x = \mathrm{Im}(\zeta_w)$$

and from the Cauchy-Riemann conditions,

$$u_y = -v_x$$

$$v_y = u_x$$

then

$$r_x = (uu_x + vv_x)/r \qquad \text{(a)}$$

$$r_y = (uu_y + vv_y)/r \qquad \text{(b)}$$

$$\theta_x = (uv_x - vu_x)/r^2 \qquad \text{(c)}$$

$$\theta_y = (uv_y - vu_y)/r^2 \qquad \text{(d)}$$

$$\tag{7}$$

10

For the $\eth$ derivatives of the mappings, the following results are obtained:

$$W_{\eth} = \overline{W}_{\eth}^{*} \frac{(W - W^{*})}{(\overline{W}^{*} + W^{*})} + \frac{W_{\eth}^{*}(W + \overline{W}^{*})}{\overline{W}^{*} + W^{*}}$$

$$x_{\eth} = \mathrm{Re}(W_{\eth})$$

$$y_{\eth} = \mathrm{Im}(W_{\eth}) \tag{8}$$

where

$$\overline{W}_{\eth}^{*} = x_{\eth}^{*} + iy_{\eth}^{*}$$

$$\overline{W}_{\eth}^{*} = x_{\eth}^{*} - iy_{\eth}^{*}$$

Where $x_{\eth}^{*} = x_{z}^{*}$, $y_{\eth}^{*} = y_{z}^{*}$ since $z = \eth$ and $z_{\eth} = 1$. Now, since r, θ, $\eth$ are independent coordinates, it follows that $r_{\eth} = \theta_{\eth} = 0$. Therefore:

$$r_{\eth} = r_x x_{\eth} + r_y y_{\eth} + r_z z_{\eth} = 0$$

and

$$\theta_{\eth} = \theta_x x_{\eth} + \theta_y y_{\eth} + \theta_z z_{\eth} = 0$$

Solving for r_z and θ_z, the following results are obtained:

$$r_z = - (r_y y_{\eth} + r_x x_{\eth}) \tag{a}$$

$$\theta_z = - (\theta_y y_{\eth} + \theta_x x_{\eth}^{*}) \tag{b}$$

$$(9)$$

The second derivatives of this transformation, needed for the body point calculation, are derived in a similar fashion.

The singularity of this mapping is located inside the body so that the mappings are never evaluated at singular points. It is not necessary that the mappings be conformal but it has been found that conformal mappings give the best results in terms of mesh point distribution. It is also not necessary that r, θ, $\eth$ be orthogonal coordinates and, in general, they are not.

These mappings (Eq. (1)) use simple algebraic expressions and their coefficients are defined explicitly so that transformation from one space to another takes a minimum of time. Considerable work has been done to develop conformal

11

mappings that can map arbitrary cross sections into circles or near circles (Reference 4). These generalized mappings offer a greater flexibility than the mappings used herein, but would require a large increase in computational time.

Some examples of the mesh generation in the physical space are shown in Figure 6 for elliptical and cambered wing cross sections. The mappings yield the highest mesh density in the vicinity of the leading edge.

With the mapped plane completely defined, the transformation between the computational space and the mapped space $(X, Y, Z) \rightarrow (r, \theta, \delta)$ is required. Consider a cross section $(Z = \delta = \text{constant})$ with multiple shock waves, e.g., (Figure 7) bow shock, wing shock and tail shock, plus two crossflow shocks. The computational plane is divided into IC regions in the Y direction, and LC regions in the X direction. They are ordered as in Figure 4. The body is described by $r = B(Y, Z)$ and a wing-type shock as $r = \overline{C}_\ell(Y, Z)$ for $\ell = 1 \rightarrow LC$ ($\ell = LC$ being the bow shock). Similarly, the crossflow shocks are described as $\theta = H_i(X, Z)$ for $i = 1 \rightarrow IC + 1$ ($i = 1$ is the bottom symmetry plane and $i = IC + 1$ is the top symmetry plane). These surfaces are shocks for some range of X and Y, and arbitrary (dividing) surfaces for other values of X and Y, as described previously.

Now define LC + 1 surfaces such that:

$$C_1(Y, Z) = B(Y, Z)$$

$$C_\ell(Y, Z) = \overline{C}_{\ell-1}(Y, Z) \quad (\ell = 2, 3 \ldots LC + 1)$$

The transformation to the computational plane then can be written as:

$$X = (r - C_\ell)/(C_{\ell+1} - C_\ell) \quad \text{(a)}$$

$$Y = (\theta - H_i)/(H_{i+1} - H_i) \quad \text{(b)} \qquad (10)$$

$$Z = \delta \qquad \text{(c)}$$

12

(a)
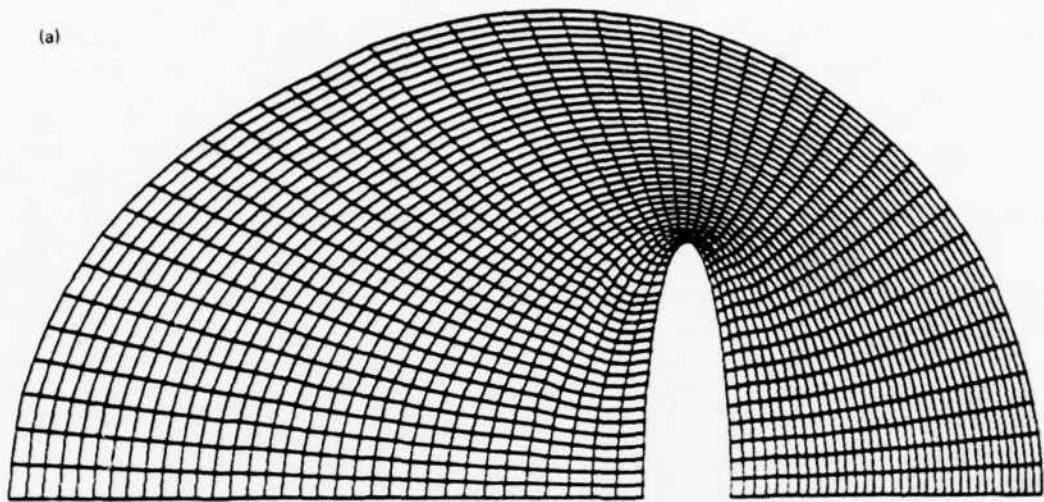
(b)
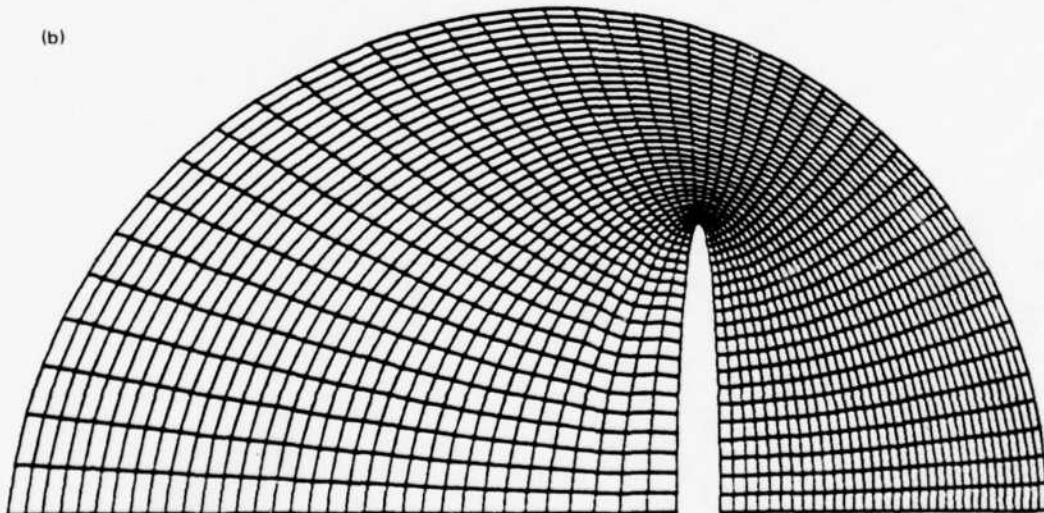
1248-78(1/2)W

Figure 6 Grids Generated Using Mappings for Several Wing Cross Sections

13

(c)
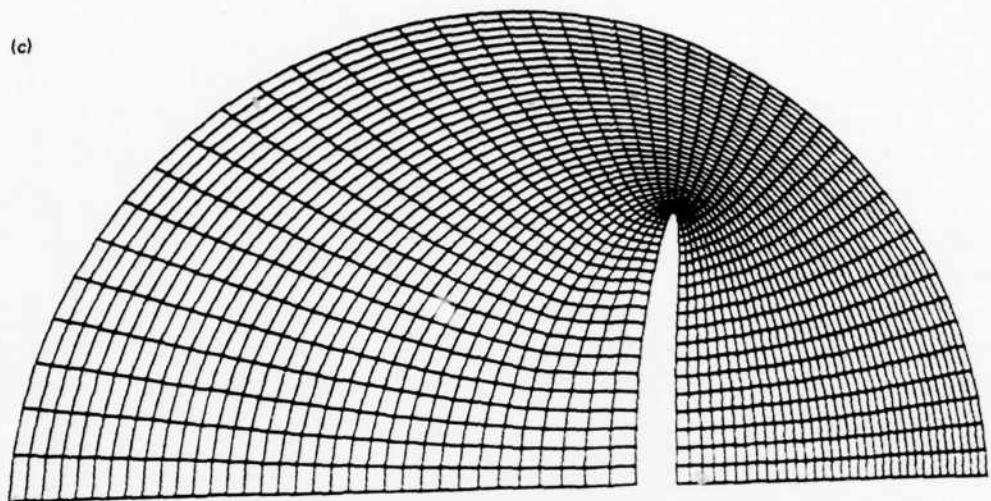
(d)
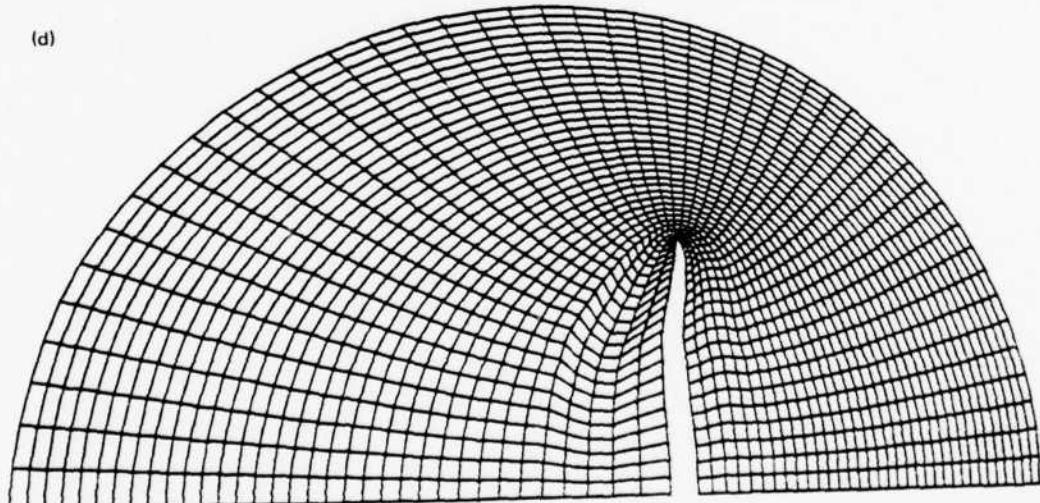
1248-78(2/2)W

Figure 6 (Concluded)

14

R80-1248-004W
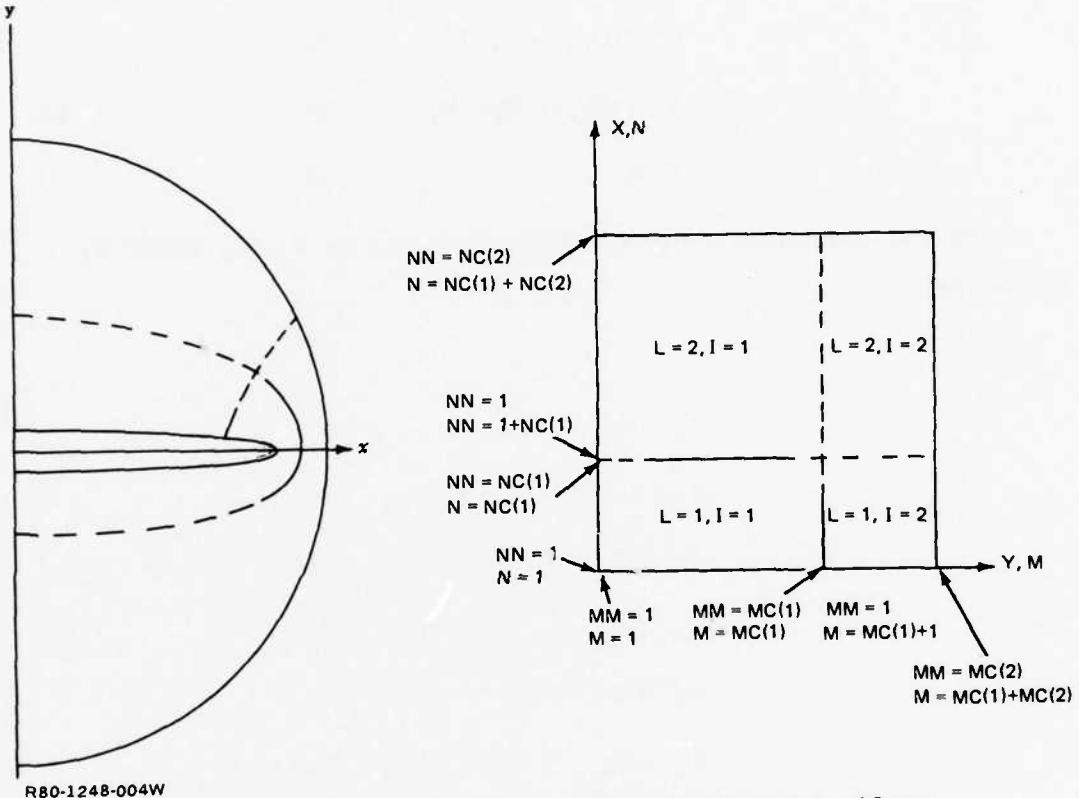
Figure 7   Cross Sectional Shock Pattern in Mapped and Computational Spaces

15

The coordinates X, Y, Z are not orthogonal. The boundary C_ℓ in the mapped plane becomes $X = 0$ in region ℓ and $C_{\ell+1}$ becomes $X = 1$. Similarly, the IC regions in the Y-direction in the computational plane are bounded by $Y = 0$ and $Y = 1$.

Inverting this transformation yields the result:

$$r = X(C_{\ell+1} - C_\ell) + C_\ell \qquad (a)$$

$$\theta = Y(H_{i+1} - H_i) + H_i \qquad (b) \qquad\qquad (11)$$

$$\mathfrak{z} = Z \qquad (c)$$

Again, the derivatives of this transformation, X_r, X_θ, $X_\mathfrak{z}$, Y_r, Y_θ and $Y_\mathfrak{z}$, are needed.

First

$$r_X = (C_{\ell+1} - C_\ell) \qquad (a)$$

$$r_Y = (C_{Y_{\ell+1}} - C_{Y_\ell})\, X + C_{Y_\ell} \qquad (b)$$

$$r_Z = (C_{Z_{\ell+1}} - C_{Z_\ell})\, X + C_{Z_\ell} \qquad (c)$$

$$\theta_X = (H_{X_{\ell+1}} - H_{X_i})\, Y + H_{X_i} \qquad (d) \qquad\qquad (12)$$

$$\theta_Y = (H_{i+1} - H_i) \qquad (e)$$

$$\theta_Z = (H_{Z_{i+1}} - H_{Z_i})\, Y + H_{Z_i} \qquad (f)$$

$$\mathfrak{z}_X = 0 \qquad (g)$$

$$\mathfrak{z}_Y = 0 \qquad (h)$$

$$\mathfrak{z}_Z = 1 \qquad (i)$$

The Jacobian of the transformation is defined as:

$$J \equiv \frac{\partial(r,\ \theta,\ \mathfrak{z})}{\partial(X, Y, Z)} \equiv \begin{vmatrix} r_X & r_Y & r_Z \\ \theta_X & \theta_Y & \theta_Z \\ \mathfrak{z}_X & \mathfrak{z}_Y & \mathfrak{z}_Z \end{vmatrix}$$

16

and thus

$$X_r = \frac{1}{J} \left[\frac{\partial(X, \theta, \delta)}{\partial(X, Y, Z)} \right] \qquad \text{(a)}$$

$$Y_r = \frac{1}{J} \left[\frac{\partial(Y, \theta, \delta)}{\partial(X, Y, Z)} \right] \qquad \text{(b)}$$

$$X_\theta = \frac{1}{J} \left[\frac{\partial(r, X, \delta)}{\partial(X, Y, Z)} \right] \qquad \text{(c)}$$

$$Y_\theta = \frac{1}{J} \left[\frac{\partial(r, Y, \delta)}{\partial(X, Y, Z)} \right] \qquad \text{(d)}$$ (13)

$$X_\delta = \frac{1}{J} \left[\frac{\partial(r, \theta, X)}{\partial(X, Y, Z)} \right] \qquad \text{(e)}$$

$$Y_\delta = \frac{1}{J} \left[\frac{\partial(r, \theta, Y)}{\partial(X, Y, Z)} \right] \qquad \text{(f)}$$

After some algebraic manipulations the above derivatives can be written in the following form:

$$X_r = 1. / [\delta + X D_1 \delta_Y + D_1 C_{Y_\ell}] \qquad \text{(a)}$$

$$Y_r = D_1 X_r \qquad \text{(b)}$$

$$Y_\theta = 1. / [\Delta + Y D_2 \Delta_X - D_2 H_{x1}] \qquad \text{(c)}$$

$$X_\theta = D_2 Y_\theta \qquad \text{(d)}$$

$$X_\delta = - \frac{[X \delta_Z + X \delta_Y D_3 + C_{Z_\ell} + C_{Y_\ell} D_3]}{[\delta + X D_4 \delta_Y + C_{Y_\ell} D_4]} \qquad \text{(e)}$$ (14)

$$Y_\delta = D_3 + D_4 X_\delta \qquad \text{(f)}$$

where

$$\delta = C_{\ell+1} - C_\ell \qquad \text{(a)}$$

$$\delta_Y = C_{Y_{\ell+1}} - C_{Y_\ell} \qquad \text{(b)}$$

$$\delta_Z = C_{Z_{\ell+1}} - C_{Z_\ell} \qquad \text{(c)}$$

$$\Delta = H_{i+1} - H_i \qquad \text{(d)}$$

17

$$\Delta_X = H_{X_{i+1}} - H_{X_i} \qquad \text{(e)}$$

$$\Delta_Z = H_{Z_{i+1}} - H_{Z_i} \qquad \text{(f)} \qquad\qquad (15)$$

$$D_1 = -(Y\Delta_X - H_{X_i})/\Delta \qquad \text{(g)}$$

$$D_2 = -(X\delta_Y + C_{Y_\ell})/\delta \qquad \text{(h)}$$

$$D_3 = -(H_{Z_i} + Y\Delta_Z)/\Delta \qquad \text{(i)}$$

$$D_4 = -(H_{X_i} + Y\Delta_X)/\Delta \qquad \text{(j)}$$

This transformation is a modification of the one used previously by Moretti to solve numerical problems (e.g., see Reference 5). Singularities occur when $C_\ell = C_{\ell+1}$ or $H_i = H_{i+1}$ and when $J = 0$. The former occurs when two shocks intersect. This matter will be discussed in the section on "Treatment of Shocks". The latter case occurs when the mesh lines X = constant and Y = constant become parallel in the physical plane. This can occur for certain locations of crossflow shocks. However this problem can be overcome by either modifying the conformal mappings so that the cross section in the mapped plane is "more circular," or by using a crossflow shock-type surface (which acts like an extension to a crossflow shock) to control the shape of the mesh lines.

All shocks are defined in the mapped plane as $r = \bar{c}(\theta, \eth)$ and $\theta = h(r, \eth)$, so that $\bar{C}(Y, Z) = \bar{c}[\theta(X_s, Y, Z), \eth], H(X, Z) = h[r(X, Y_s, Z), \eth]$ (where X_s and Y_s are either 0 or 1) and their derivatives $\bar{C}_Y, \bar{C}_Z, H_X$ and H_Z must be calculated. The body is defined in the physical plane and an iterative procedure is needed to describe the body as $r = b(\theta, \eth)$ from which $B(Y, Z)$ can be computed. From the derivatives $b_\theta, b_\eth, \bar{c}_\theta, \bar{c}_\eth, h_\eth$ and h_r, the calculation of $B, \bar{C}, B_Z$, and $\bar{C}_Z$ proceeds as follows.

Using the notation of equations (11, 12 and 13), define

$$c_1 \equiv b(\theta, \eth)$$

$$c_\ell \equiv \bar{c}_{\ell-1}(\theta, \eth)$$

18

then

$$C_{X_\ell} = c_{\theta_\ell} [H(X_s, Z)_{i+1} - H(X_s, Z)_i]$$

$$H_{X_i} = h_{r_i} [C(Y_s, Z)_{\ell+1} - C(Y_s, Z)_\ell] \tag{16}$$

Where again X_s (the value of X at the shock C_ℓ) and Y_s (the value of Y at the shock H_i) are 0 or 1.

$$C_{Z_\ell} = c_{\delta_\ell} + c_{\theta_\ell} \theta_Z \tag{a}$$

$$\theta_Z = Y(H_Z(X_s, Z)_{i+1} - H_Z(X_s, Z)_i) + H_Z(X_s, Z)_i \tag{b}$$

$$H_{Z_i} = h_{\delta_i} + h_{r_i} r_Z \tag{c}$$

$$r_Z = X[C_Z(Y_s, Z)_{\ell+1} - C_Z(Y_s, Z)_\ell] + C_Z(Y_s, Z)_\ell \tag{d}$$

(17)

At the points $X = X_s$ and $Y = Y_s$ at a cross section Z, these equations result in a set of simultaneous linear equations for $H_Z(X_s, Z)$ and $C_Z(Y_s, Z)$:

$$C_Z(Y_s, Z)_\ell = \frac{c_{\theta_\ell}[Y_s(h_{\delta_{i+1}} - h_{\delta_i}) - h_{\delta_i}] + c_{\delta_\ell}}{1 - c_{\theta_\ell}[Y_s(h_{r_{i+1}} - h_{r_i}) - h_{r_i}]} \tag{18}$$

whereas $H_Z(X_s, Z)$ can be computed from equations (16). For all other points, equation (16) is used to compute $C_Z(Y, Z)$ and $H_Z(X, Z)$.

Now the computational plane and its boundaries are completely defined so that, for any mesh point (X, Y, Z) in the computational plane, the corresponding point (x, y, z) in the physical plane and all the necessary transformation derivatives can be computed.

SECTION IV

COMPUTATION OF REGIONS OF CONTINUOUS FLOW

In the physical plane (x, y, z) the Euler equations are:

$$wP_z + \gamma w_z = -(uP_x + vP_y + \gamma u_x + \gamma v_y) \qquad \text{(a)}$$

$$wu_z = -(uu_x + vu_y + TP_x) \qquad \text{(b)}$$

$$wv_z = -(uv_x + vv_y + TP_y) \qquad \text{(c)} \qquad (19)$$

$$TP_z + ww_z = -(uw_x + vw_y) \qquad \text{(d)}$$

$$wS_z = -(uS_x + vS_y) \qquad \text{(e)}$$

where $T = \overline{T}/\overline{T}_\infty$, $P = \ln(\overline{p}/\overline{p}_\infty)$, $S = (\overline{S} - \widetilde{S}_\infty)/c_{v_\infty}$ and all velocities are nondimensionalized with respect to $\sqrt{p_\infty/\rho_\infty}$ (the barred quantities are dimensional), $x = \overline{x}/\overline{\ell}$, $y = \overline{y}/\overline{\ell}$, $z = \overline{z}/\overline{\ell}$ ($\overline{\ell}$ is an arbitrary length).

The equation of state for an ideal gas becomes:

$$\ln(T) = P\frac{(\gamma - 1)}{\gamma} + \frac{S}{\gamma} \qquad (20)$$

The dependent variables are P, S and the Cartesian velocity components u, v, w (Figure 1). Transforming all derivatives to the computational plane, the following results are obtained.

$$f_x = f_X X_x + f_Y Y_x + f_Z Z_x \qquad \text{(a)}$$

$$f_y = f_X X_y + f_Y Y_y + f_Z Z_y \qquad \text{(b)} \qquad (21)$$

$$f_z = f_X X_z + f_Y Y_z + f_Z Z_z \qquad \text{(c)}$$

where f is the vector (P, u, v, w, S) and

$$X_x = X_r r_x + X_\theta \theta_x + X_\vartheta \vartheta_x \qquad \text{(a)}$$

$$X_y = X_r r_y + X_\theta \theta_y + X_\vartheta \vartheta_y \qquad \text{(b)} \qquad (22)$$

$$X_z = X_r r_z + X_\theta \theta_z + X_\vartheta \vartheta_z \qquad \text{(c)}$$

Similar expressions can be written for the Y and Z derivatives. The derivatives of (X, Y, Z) with respect to $(r, \theta, \mathfrak{z})$ and $(r, \theta, \mathfrak{z})$ with respect to (x, y, z) have already been discussed in the previous section.

Combining equations (19a) and (19e), the following form of the Euler equations is obtained which are used in the present solution.

$$P_Z = (a_{11}P_X + a_{12}u_X + a_{13}v_X + a_{14}w_X + b_{11}P_Y + b_{12}u_Y + b_{13}v_Y + b_{14}w_Y) \quad \text{(a)}$$

$$u_Z = -(a_{21}P_X + a_{22}u_X + b_{21}P_Y + b_{22}u_Y) \quad \text{(b)}$$

$$v_Z = -(a_{31}P_X + a_{33}v_X + b_{31}P_Y + b_{33}v_Y) \quad \text{(c)}$$

$$w_Z = -(a_{41}P_X + a_{42}u_X + a_{43}v_X + a_{44}W_X + b_{41}P_Y + b_{42}u_Y + b_{43}v_Y + b_{44}w_Y) \quad \text{(d)}$$

$$S_Z = -(a_{55}S_X + b_{55}S_Y) \quad \text{(e)}$$

$$(23)$$

where the coefficients appearing in equations (23) are defined in Appendix A.

At a data plane, $Z = Z_0 = $ constant, all the quantities on the right side of equations (23) are known and therefore the derivative f_Z can be computed and used to predict the dependent variables at $Z = Z_0 + \Delta Z$.

The step size ΔZ in the marching direction must satisfy the CFL (Courant-Friedrichs-Lewy) condition for stability (Reference 6). If $\lambda_{X\pm}$ are the characteristic slopes in the X, Z plane and $\lambda_{Y\pm}$ are the characteristic slopes in the Y, Z plane, the stability criterion is written as follows:

$$\Delta Z_{X^+} = \Delta X/\lambda_{X^+} \qquad \Delta Z_{Y^+} = \Delta Y/\lambda_{Y^-}$$

$$\Delta Z_{X^-} = \Delta X/\lambda_{X^-} \qquad \Delta Z_{Y^-} = \Delta Y/\lambda_{Y^-}$$

$$(24)$$

Each of these quantities is evaluated for every mesh point at the station $Z = Z_0$, and ΔZ is taken as 70% of the minimum of all of these ΔZ values.

A modified MacCormack, two-level, predictor-corrector finite-difference scheme (Reference 7) is used to integrate equations (23). It can be proved that the MacCormack scheme is accurate to second order for a linear system of equations, so that the truncation error is of the form:

21

$$\frac{\partial^2 f}{\partial \ell^3} \, \Delta \ell^3$$

where ℓ is a length in the physical plane. In regions where $\partial^3 f / \partial \ell^3$ is large, the mappings tend to assure $\Delta \ell \to 0$ so that the truncation error remains small, while keeping the total number of grid points to a minimum.

Equations (23) can be written in the following general form

$$f_Z = [A] f_X + [B] f_Y \tag{25}$$

where, as previously defined, f is the vector (P, u, v, w, S) and [A] and [B] are matrices of the coefficients of equations (23). With these equations, the MacCormack scheme proceeds as follows.

Level one:

$$f_Z(Z_0) = [A] f_X + [B] f_Y \qquad \text{(all quantities evaluated at } Z_0) \tag{a}$$

$$\tilde{f} = f(Z_0) + f_Z(Z_0) \Delta Z \qquad (\tilde{f} \text{ is the predicted value}) \tag{b}$$

Level two: $\hspace{9cm}$ (26)

$$\tilde{f}_Z = [\tilde{A}] \tilde{f}_X + [\tilde{B}] \tilde{f}_Y \qquad \text{(all dependent variables evaluated} \tag{c}$$
$$\text{with the predicted values and all}$$
$$\text{independent variables are}$$
$$\text{evaluated at } Z = Z_0 + \Delta Z)$$

$$f(Z_0 + \Delta Z) = (\tilde{f} + f(Z_0) + \tilde{f}_Z \Delta Z)/2 \tag{d}$$

The f_X derivatives are taken one sided in the positive X-direction in level one, the f_Y derivatives in the positive Y-direction. For level two the direction of these derivatives is reversed.

This procedure defines all the dependent variables at interior points of the computational plane $(1 < NN < NC(L)$ and $1 < MM < MC(I))$, Figure 7. The body point calculation and the shock point calculation will be discussed later. However, note there that all imbedded shock points have two mesh points associated

22

with them, one for the low pressure side and one for the high pressure side, both having the same position in the physical plane (Figure 7). The low pressure side of all shocks is computed following the MacCormack scheme and taking X and Y derivatives into the low pressure region in both levels. The low pressure side of the bow shock ((NN = NC(L), L = LC)) is defined by the given free-stream conditions.

The points on the symmetry planes (MM = 1, I = 1 and MM = MC (I), I = IC) are computed using the same scheme and the symmetry conditions $P_Y = v_Y = w_Y = S_Y = 0$ and $u = 0$. The points on the internal boundaries that are not shock points are also computed using the MacCormack scheme. In level one, the points NN = 1 and MM = 1 are computed, taking the difference between NN = 1, NN = 2 and MM = 1, MM = 2 for the X and Y derivatives, respectively. After level one, quantities at NC (L) and MC (L) are updated (i.e., $f(NC(L), M)_L = f(1, M)_{L+1}$ and $f(N, MC(I))_I = f(N, 1)_{I+1}$). In level two the points on the other side of the surfaces, NN = NC (L) and MM = MC (I), are computed and afterward the points NN = 1 and MM = 1 are updated.

A careful study of the numerical results initially generated for thin, supersonic wings indicated that the gradients in the Cartesian velocity components u and v were very large, while the gradient in the velocity component in the directions of the computational space coordinates X and Y were much smaller. These velocity components are defined by:

$$\bar{u} = uI_x + vI_y + wI_z$$

$$\bar{v} = uJ_x + vJ_y + wJ_z$$

where $\vec{I} = \nabla X / |\nabla X|$ and $\vec{J} = \nabla Y / |\nabla Y|$

Solving for the two Cartesian velocity components u and v,

$$u = \frac{\begin{pmatrix} \bar{u} - wI_z & I_y \\ \bar{v} - wJ_z & J_y \end{pmatrix}}{DET} \tag{27}$$

23

and

$$v = \underbrace{\begin{pmatrix} I_x & \tilde{u} - wI_z \\ J_x & \tilde{v} - wJ_z \end{pmatrix}}_{DET} \tag{28}$$

where

$$DET = I_x J_y - J_x I_y$$

By analytically differentiating equations (27) and (28), the derivatives of the cartesian velocity components can be determined as a function of $\hat{u}$, $\hat{v}$ and their derivatives, which are evaluated numerically. It was found that numerically differencing $\hat{u}$ and $\hat{v}$, instead of u and v, reduced the truncation error of the total computation significantly.

It should be noted that $\hat{u}$ and $\hat{v}$ are the normal and tangential crossflow velocity components, respectively, on the surface of the body. Thus, $\hat{u}$ is constrained to vanish on the surface due to the flow tangency boundary condition. A comparison of the two sets of velocity components and their variation on the surface of an ellipse is shown in Figure 8. The improvements in the computed results are demonstrated in Figure 9 at zero angle of attack. A marked improvement in the results at angle of attack is demonstrated in Figure 10.

Special difference formulas must be used to avoid difficulties associated with entropy discontinuities (i.e., vortical singularities). These procedures will be discussed in a subsequent section.

The calculation of interior points is the most time consuming of this computation mainly because it is done many times. The scheme used here keeps the computational time to a minimum by keeping the total number of mesh points as small as possible.

24
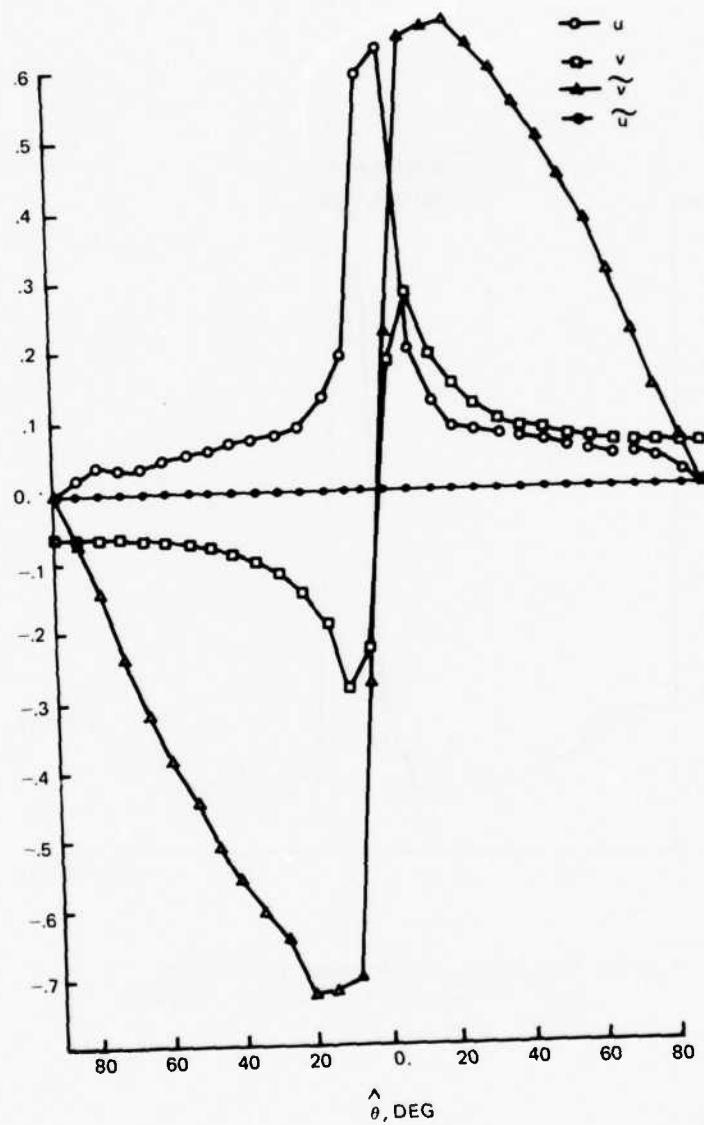
Figure 8   Surface Velocity Components, Elliptic Cone
(a/b = 14) δ_T = 20°, δ_p = 1.5°, M_∞ = .2 and
α = 0.°

R80-1248-006W

Figure 9   Computed Surface Pressures, Elliptic Cone
(a/b = 14) $\delta_T \approx 20°$, $\delta_p = 1.5°$, $M_\infty = 2.$, and
$\alpha = 0$.

26
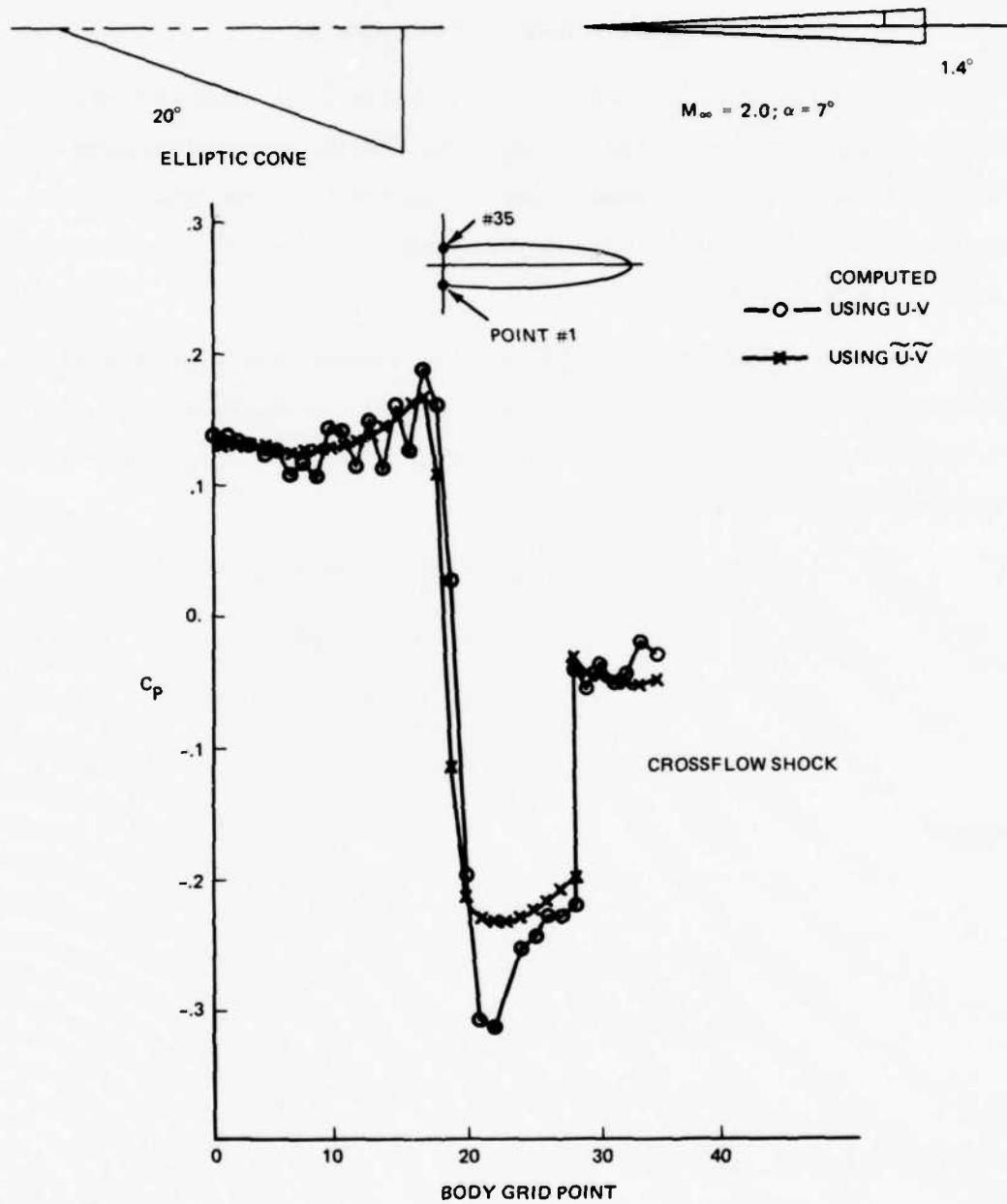
Figure 10 Comparison of Surface Pressure Distributions Using Two Different Sets of Dependent Variables

R80-1248-007W

SECTION V

BODY POINT COMPUTATION

The boundary condition at the vehicle surface is $\bar{u} = 0$, where $\bar{u}$ is the velocity normal to the body. The entropy at the body is computed by using equation (23e), as for any other mesh point. At the body, the coefficient of S_X (i.e., a_{55}) in equation (23e) vanishes so that this derivative does not affect the calculation of entropy on the body.

To compute the pressure on the body, the continuity and three momentum equations (23a, b, c, and d) and the body boundary condition are combined to write a compatibility equation along the characteristic (in the X, Z plane) reaching the wall from the flow field.

$$P_Z + a_{11}P_X + a_{12}u_X + a_{13}v_X + a_{14}w_X = R_1 \qquad \text{(a)}$$

$$u_Z + a_{21}P_X + a_{22}u_X = R_2 \qquad \text{(b)}$$

$$v_Z + a_{31}P_X + a_{33}v_X = R_3 \qquad \text{(c)} \qquad (29)$$

$$w_Z + a_{41}P_X + a_{42}u_X + a_{43}v_X + a_{44}w_X = R_4 \qquad \text{(d)}$$

where:

$$R_1 = -(b_{11}P_Y + b_{12}u_Y + b_{13}v_Y + b_{14}w_Y)$$

$$R_2 = -(b_{21}P_Y + b_{22}u_Y)$$

$$R_3 = -(b_{31}P_Y + b_{33}v_Y)$$

$$R_4 = -(b_{41}P_Y + b_{42}u_Y + b_{43}u_Y + b_{44}w_Y)$$

Substituting for a_{12}, a_{13} and a_{14} equation (29a) becomes

$$P_Z + a_{11}P_X + \frac{w^2\gamma X_\mathbf{z}}{A_1}\tau_X + \frac{w^2\gamma X_\mathbf{y}}{A_1}\sigma_X = R_1 \qquad (30)$$

where:

$$\tau = u/w \text{ and } \sigma = v/w$$

28

Taking the difference between the product of w with equation (29b) and u with equation (29b) and substituting for a_{33}, a_{43}, a_{42} and a_{44}, the following result is obtained.

$$w^2\tau_Z + P_X(wa_{21} - ua_{41}) + w^2\left(X_z + \frac{X_x\tau w^2}{A_1} - X_y\sigma\right)\tau_X$$
$$+ \frac{w^2\tau\gamma T}{A_1} X_y\,\sigma_X = wR_2 - uR_4 \tag{31}$$

Similarly, taking the difference between the product of w with equation (29c) and v with equation (29d) and substituting for a_{33}, a_{43}, a_{42} and a_{44}, the following result is obtained.

$$w^2\sigma_Z + P_X(wa_{31} - va_{41}) + w^2\left(X_z + \frac{X_y\sigma w^2}{A_1} + X_x\tau\right)\sigma_X$$
$$+ \frac{w^2\sigma\gamma T}{A_1} X_x\tau_X = wR_3 - vR_4 \tag{32}$$

The body boundary condition is $\bar{u} = 0$. Since X = constant is the body, this boundary condition can be written as

$$\bar{u} = uX_x + vX_y + wX_z = 0$$

or:

$$\tau X_x + \sigma X_y + X_z = 0 \tag{33}$$

Combining equations (30), (31), and (32) and using equation (33), the equation for the characteristic slopes can be written in the form

$$\lambda_{\pm} = \frac{-a_{14}T}{w} \pm \sqrt{\frac{a_{14}^2 T^2}{w^2} + \frac{\gamma T}{A_1}\left[\frac{(vX_y + uX_x)^2}{w^2} + X_y^2 + X_x^2\right]} \tag{34}$$

where λ_- is the slope of the characteristic reaching the wall from the flow field. The compatibility condition along this characteristic is:

$$\left[\lambda - \frac{\gamma T}{A_1 w}(uX_x + vX_y)\right](P_Z + \lambda P_X)$$
$$+ \frac{w^2\gamma}{A_1}(X_x\tau_Z + X_y\sigma_Z) + \frac{w^2\gamma\lambda}{A_1}(X_x\tau_X + X_y\sigma_X) = \frac{R}{\lambda} \tag{35}$$

29

where:

$$R = \left(\lambda - \frac{\gamma T}{A_1 w}(uX_x + vX_y)\right)R_1$$

$$+ \frac{X_x \gamma \lambda}{A_1}(wR_2 - uR_4) + \frac{X_y \gamma \lambda}{A_1}(wR_3 - uR_4)$$

The equation for the body can be written in the form:

$$F = r - B(Y, Z) \tag{36}$$

Thus the body boundary condition is:

$$\tau F_x + \sigma F_y + F_z = 0 \tag{37}$$

This equation holds for all values of Z, thus:

$$\sigma_Z F_y + \tau_Z F_x = -(F_{zZ} + \sigma F_{yZ} + \tau F_{xZ}) = \overline{R} \tag{38}$$

Now using equation (10a), equation (36) becomes:

$$F = r - B = (C_\ell - B)X \tag{39}$$

Thus, differentiating equation (39):

$$F_x = [(C_\ell)_x - B_x]X + (C_\ell - B)X_x \tag{a}$$
$$\tag{40}$$
$$F_y = [(C_\ell)_y - B_y]X + (C_\ell - B)X_y \tag{b}$$

and, for $X = 0$:

$$F_x = (C_\ell - B)X_x \tag{a}$$
$$\tag{41}$$
$$F_y = (C_\ell - B)X_y \tag{b}$$

Using equations (38) and (41) in equation (35), the following result is obtained:

$$P_z = \frac{\dfrac{R}{\lambda_+} - \dfrac{\gamma w^2}{A_1}\left[\dfrac{\overline{R}}{(C_\ell - B)} + \lambda_+(X_x \tau_X + X_y \sigma_X)\right]}{\left[\lambda_+ - \dfrac{\gamma T}{A_1}(\tau X_x + \sigma X_y)\right]} - \lambda_+ P_X \tag{42}$$

This equation is integrated with the same scheme used for interior points with the X-derivatives, computed using three-point end differencing away from the body.

30

To compute the velocity components on the body, an intrinsic frame $(\hat{I}, \hat{J}, \hat{K})$ is used with velocity components $(\bar{u}, \bar{v}, \bar{w})$. The vector $\hat{I}$ is the unit normal to the body, with $\hat{J}$ and $\hat{K}$ defined as follows:

$$\hat{I} = I_1\hat{i} + I_2\hat{j} + I_3\hat{k} \tag{a}$$

$$\hat{J} = (\hat{I} \times \hat{k})/|\hat{I} \times \hat{k}| = J_1\hat{i} + J_2\hat{j} + J_3\hat{k} \tag{b} \qquad (43)$$

$$\hat{K} = \hat{I} \times \hat{K} = K_1\hat{i} + K_2\hat{j} + K_3\hat{k} \tag{c}$$

where $\hat{i}$, $\hat{j}$ and $\hat{k}$ are defined in Figure 4. The x and y momentum equations are used to compute $\bar{v}$ as follows. Equations (29b) and (29c) are integrated using the MacCormack scheme to obtain u and v and then $\bar{v}$ is obtained from the equation

$$\bar{v} = uJ_1 + vJ_2 \tag{44}$$

From the integrated form of the energy equation, the $\bar{w}$ component of velocity can be obtained:

$$\bar{w} = \sqrt{2H_0 - \frac{2\gamma T}{\gamma - 1} - \bar{v}^2} \tag{45}$$

where T is computed from P and S and the equation of state (19). The three Cartesian velocity components are:

$$u = \bar{v}J_1 + \bar{w}K_1 \tag{a}$$

$$v = \bar{v}J_2 + \bar{w}K_2 \tag{b} \qquad (46)$$

$$w = \bar{v}J_3 + \bar{w}K_3 \tag{c}$$

SECTION VI

TREATMENT OF SHOCKS

In this section, the computation of grid points on the high pressure side of all shock waves and the detection of embedded shocks will be discussed. In this area, we draw systematically from Moretti's extensive research on the treatment of shock waves (Reference 8 and 9).

The bow shock, all wing-type shocks (i.e., embedded shocks which, in general, originate near the body and move toward the bow shock and are caused by canopies, wings and vertical tails, see Figure 11) and crossflow shocks in the flowfield are computed as discontinuities satisfying the Rankine-Hugoniot conditions. The bow shock and wing-type shocks are defined in the mapped plane by $r = \bar{c}(\theta, \mathcal{z})$ and the crossflow shocks by $\theta = h(r, \mathcal{z})$. At a data plane Z_0, all dependent variables are known and, in addition, the quantities $\bar{c}$, $\bar{c}_\theta$, $\bar{c}_\mathcal{z}$, h, h_r, $h_\mathcal{z}$ are also known. Using equations (16 to 18) $C(Y, Z_0)$, C_Y, C_Z, $H(X, Z_0)$, H_X and H_Z are computed for all the shocks in the flowfield. At $Z_0 + \Delta Z$, the positions of the shock points can be computed by using:

$$C(Y, Z_0 + \Delta Z) = C(Y, Z_0) + C_Z(Y, Z_0) \Delta Z \qquad \text{(a)}$$

$$\qquad\qquad\qquad\qquad\qquad\qquad\qquad\qquad\qquad\qquad\qquad (47)$$

$$H(X, Z_0 + \Delta Z) = H(X, Z_0) + H_Z(X, Z_0) \Delta Z \qquad \text{(b)}$$

Then $C_Y(Y, Z_0 + \Delta Z)$ and $H_X(X, Z_0 + \Delta Z)$ are computed using central differences. With these quantities and equations (16) $\bar{c}$, $\bar{c}_\theta$, h and h_r can be computed at $Z = Z_0 + \Delta Z$.

After the first level of the MacCormack scheme, the predicted values of the dependent variables on the low pressure side of all shocks are computed (the variables on the low pressure side of the bow shock being the constant free stream values). With the low pressure side of the shocks known, the high pressure side is computed by an iterative process.
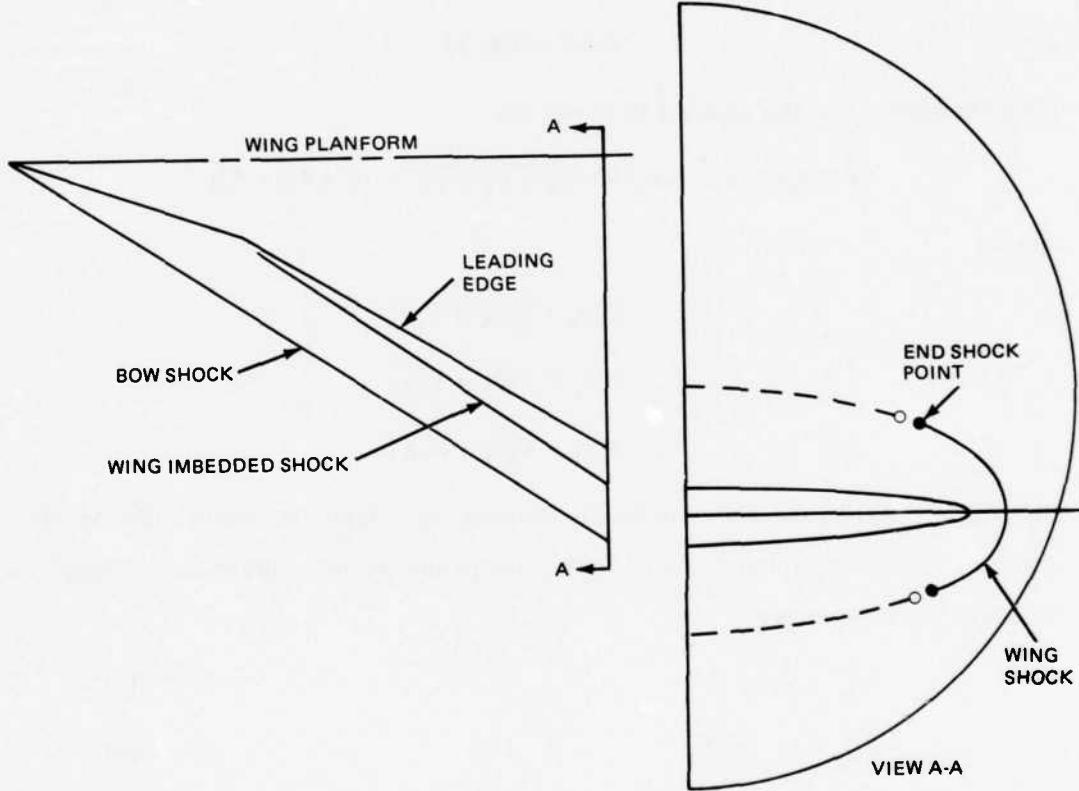
R80-1248-008W

Figure 11 Wing Shock Point Detection

A value of h_{∂} or $\bar{c}_{\partial}$ is guessed, between the values corresponding to an infinitely weak shock and the value which gives a subsonic axial Mach number. Once this guess is made, the normal to the shock can be defined. Let

$$F \equiv r - \bar{c}(\theta, \partial)$$

or

$$F \equiv \theta - h(r, \partial)$$

Then the normal to the shock $\hat{I}$ is given by:

$$\hat{I} = (F_x \hat{i} + F_y \hat{j} + F_z \hat{k}) / \sqrt{F_x^2 + F_y^2 + F_z^2} = I_1 \hat{i} + I_2 \hat{j} + I_3 \hat{k}$$

where:

$$F_x = F_r r_x + F_\theta \theta_x + F_\partial \partial_x$$

$$F_y = F_r r_y + F_\theta \theta_y + F_\partial \partial_y$$

$$F_z = F_r r_z + F_\theta \theta_z + F_\partial \partial_z$$

With the normal to the shock defined, the Rankine-Hugoniot conditions can be applied. Using the subscripts 1 for the low pressure side and 2 for the high pressure side, we have:

$$V_{n_1} = \vec{V}_1 \cdot \hat{I} \tag{a}$$

$$M_{n_1} = V_{n_1}/\sqrt{\gamma T_1} \tag{b}$$

$$\rho_2/\rho_1 = [M_{n_1}^2 (\gamma + 1)/2.]/[1 + M_{n_1}^2 (\gamma - 1)/2.] \tag{c} \qquad (48)$$

$$p_2/p_1 = [(\gamma + 1)/(\gamma - 1) \rho_2/\rho_1 - 1.]/[(\gamma + 1)/(\gamma - 1) - \rho_2/\rho_1] \tag{d}$$

$$T_2/T_1 = [T_1(p_2/p_1)]/(\rho_2/\rho_1) \tag{e}$$

$$\vec{V}_{T_2} = \vec{V}_{T_1} - V_{n_1} \hat{I} \tag{f}$$

where M_n and V_n are the Mach number and velocity normal to the shock and $\vec{V}_T$ is the velocity tangent to the shock.

34

An intrinsic coordinate system is defined at the shock with the three direc-
tions $(\hat{I}, \hat{J}, \hat{K})$, coordinates (ξ, η, ω) and velocities $(\bar{u}, \bar{v}, \bar{w})$ such that $\hat{I}$ is normal
to the shock and:

$$\hat{K} = (\hat{I} \times \hat{k})/|\hat{I} \times \hat{k}| = K_1\hat{i} + K_2\hat{j} + K_3\hat{k}$$

$$\hat{J} = \hat{I} \times \hat{K} = J_1\hat{i} + J_2\hat{j} + J_3\hat{k}$$

In the ξ, ω plane, the characteristic that intersects the shock from the high
pressure side has a slope:

$$\frac{d\xi}{d\omega} = \lambda = \frac{(\bar{u}\tilde{w} + a\sqrt{\tilde{u}^2 + \tilde{w}^2 - a^2})}{(\tilde{w}^2 - a^2)} \tag{49}$$

A point (*) in the Z_0 data plane is where the characteristic originates. The
characteristic slope at the shock point is first evaluated and then the position
of the (*) point is computed using the relations:

$$\omega^* = -\Delta Z/(K_3 + \lambda I_3) \tag{a}$$

$$\xi^* = \lambda \omega^* \tag{b}$$

$$x^* = x_{SH} + \xi^* I_1 + \omega^* K_1 \tag{c}$$

$$y^* = y_{SH} + \xi^* I_2 + \omega^* K_2 \tag{d}$$

(50)

where the subscript SH refers to quantities at the shock at $Z_0 + \Delta Z$. Depen-
dent variables at the (*) point are obtained by linear interpolation. A value of
the pressure on the high pressure side of the shock is computed using the com-
patibility equation along the characteristic:

$$\beta = \gamma \tilde{w}^2/[a\sqrt{\tilde{u}^2 + \tilde{w}^2 - a^2}] \tag{a}$$

$$\lambda = (\bar{u}\tilde{w} + a\sqrt{\bar{u}^2 + \tilde{w}^2 - a^2})/(\tilde{w}^2 - a^2) \tag{b}$$

$$R = \frac{[(\bar{u} - \lambda\tilde{w})(\tilde{v}P_\eta + \gamma\bar{v}_\eta) - (\gamma\tilde{v}\tilde{u}_\eta)\gamma\tilde{v}\tilde{w}_\eta]}{a\sqrt{\bar{u}^2 + \tilde{w}^2 - a^2}} \tag{c}$$

(51)

$$d\tau = \tilde{u}^*/\tilde{w}^* - \tilde{u}_{SH}/\tilde{w}_{SH} \tag{d}$$

$$P_{SH} = P^* + R\omega^* - \beta d\tau \tag{e}$$

$$p_2 = e^{P_{SH}} \tag{f}$$

35

where β, λ, and R are averaged between the * point and the shock point. The iteration is continued until this value of pressure agrees with that computed from the Rankine-Hugoniot conditions for some value of $\bar{c}_{\delta}$ or h_{δ}. For weak shocks, this iteration may converge to a pressure ratio $p_2/p_1 < 1$; in these cases the value of $\bar{c}_{\delta}$ or h_{δ} which gives $p_2/p_1 = 1$ is taken.

Crossflow shock points at the body must satisfy the body boundary condition, that is, the velocity normal to the body on the high pressure side of the shock must vanish. This implies that the shock normal, at the body, must be perpendicular to the body normal. This condition gives a relationship between h_{δ} and h_r at the body:

$$h_r = (F_H - h_{\delta} F_{Bz})/F_r \tag{52}$$

where:

$$F_H = F_{Bx}\theta_x + F_{By}\theta_y + F_{Bz}\theta_z$$

$$F_r = F_{Bx}r_x + F_{By}r_y + F_{Bz}r_z$$

and F_{Bx}, F_{By}, F_{Bz} are x, y, z derivatives of $F_B = r - b(\theta,\delta)$ and $r = b(\theta,\delta)$ defines the body.

After the second level of the MacCormack scheme, the corrected, final values of the dependent variables on the low pressure side of the imbedded shocks, the values of $\bar{c}_{\delta}$ and h_{δ} computed after the first level, and the Rankine-Hugoniot conditions are used to compute the final values of the dependent variables on the high pressure side of the shocks.

The first problem encountered when one treats imbedded shocks as discontinuities is their detection. There have been a number of techniques proposed (see Reference 9). One of the earliest procedures has been found to be well suited for the type of shocks encountered in this problem.

Crossflow shocks and wing-type shocks are detected in very similar ways. For crossflow shocks, the pressure distribution is monitored in the Y-direction and, for wing-type shocks, the pressure distribution is monitored in the X-direction. At a data plane $Z = Z_0$, the maximum pressure gradient P_X for

36

wing-type shocks and P_Y for crossflow shocks is located. Then a third order polynomial is fit through the four mesh points adjacent to the maximum gradient. This polynomial takes the form:

$$\chi = a_0 P^3 + a_1 P^2 + a_2 P + a_3$$

where

$$\chi = X \text{ (for wing-type shocks)}$$

$$\chi = -Y \text{ (for crossflow shocks)}$$

and the coefficients a_0, a_1, a_2 and a_3 are computed by matching the curve fit to the four mesh points. The condition used to determine the origin of a shock is $d\chi/dP = 0$, which implies $dP/d\chi \rightarrow \infty$. Applying this condition to equation (24) yields an equation for P_ℓ of the form:

$$P_\ell = \frac{-a_1 \pm \sqrt{a_1^2 - 3a_0 a_2}}{a_0}$$

When $\sqrt{a_1^2 - 3a_0 a_2} = 0$, this equation has one real root. When this condition is satisfied, a shock is inserted in the flow field at $X_\ell = a_0 P_\ell^3 + a_1 P_\ell^2 + a_2 P_\ell + a_3$.

Crossflow shocks are assumed to originate on the body, so that the pressure distribution is monitored in the Y-direction on $X = 0$ (the body). Once a shock is found on the body, monitoring is begun at increasing values of X = constant.

In general, it is not known at what value of Y the first shock point on a wing-type shock will be found, so that the maximum pressure gradient P_X at all values of Y must be tested until the first shock point is detected. Once a wing-type shock is detected, additional shock points are sought at the grid points adjacent to the end shock points.

SECTION VII

STARTING SOLUTIONS

During the course of this study, several techniques were used to "start" the solution to the Euler equations. Early in the study, approximate Euler solutions for a circular cone at a small angle of attack (References 10 and 11) were employed to start the computation. The geometry was then deformed continuously to the desired conical wing.

Later in the study, linearized potential flow solutions for delta wings with subsonic leading edges were used and permitted the computation to start with the desired geometry. In the marching technique, the geometry was held invariant. These linearized potential flow solutions are described in the following section.

Another technique that was employed, for both conical and three dimensional wings, was to use an exact Euler solution to start the computation. For these cases, the geometry would also be continuously deformed. For example, a conical Euler solution would be used to start the computation for another conical wing. The geometry would start conically then be continuously deformed to another conical geometry.

1. LINEARIZED POTENTIAL FLOW THEORY

Since the supersonic flowfield about thin wings is of primary interest, a starting solution more representative of this type of flowfield was sought. As a first step in this direction, the linearized flow solution for the flow about thin elliptic cones with subsonic leading edge at zero angle of attack was used. This solution can be easily found in Reference 8 for linearized boundary conditions applied on the plane $Z = 0$.

The general solution for the entire Cartesian velocity field about the elliptic cone can be written in complex form as

$$u = \mathrm{Re} \left\{ \frac{-m^2}{1-m^2} \left[\tau \tan\theta + F(\theta, K) - E(\theta, K) \right] \right\}$$

$$v = \mathrm{Re} \left\{ \frac{m^2}{1-m^2} \left[\frac{1-\tau^2}{\tau^2-m^2} \right]^{1/2} \right\} \quad (53)$$

$$w = \mathrm{Re} \left\{ -m^2 / [m^2 - \tau^2]^{1/2} \right\}$$

where F and E are incomplete elliptic integrals of the first and second kind.

Also

$$K = \sqrt{1-m^2}$$

$$\theta = \sin^{-1} \left[\frac{1-\tau^2}{1-m^2} \right]^{1/2}$$

where τ is a complex variable defined by the transformations

$$\tau = \frac{2\epsilon}{1+\epsilon^2}$$

$$\epsilon = \frac{y + iz}{x + \sqrt{x^2 - y^2 - z^2}}$$

and m denotes the leading edge value of τ.

With these transformations, the entire flowfield about the elliptic cone can be defined up to the Mach cone where all disturbances vanish. Special consideration must be given to these expressions for the elliptic integrals in the symmetry planes $Z = 0$ and $y = 0$ because one or the other of the incomplete elliptic integrals reduce to the complete integral.

A computer subroutine was coded to compute this flowfield to be used as a starting solution for the nonlinear code. Several problems arose in trying to implement the solutions because of the singularities that exist at the leading edge due to the linearized boundary conditions. As a result, leading edge corrections had to be fitted to the linearized solution to obtain finite values of velocity and pressure at the leading edge (see Figure 12). The resulting solution then had to be modified in order to satisfy the exact nonlinear boundary conditions. The exact equation for the pressure also had to be used to be consistent with the nonlinear equations. The subroutine was then made compatible with the

ANALYTICAL
SOLUTION

MODIFIED SOLUTION
LEADING EDGE CORRECTED

$$U_{e_{mod}} = U_{e_s}$$
$$+ [U_e(m+\epsilon) - U_{e_s}]\left(\frac{X}{M}\right)$$

$$V_{e_{mod}} = V_e(m+\epsilon)\left(\frac{Y/X}{m}\right)$$

$$W_{e_{mod}} = W_e(m-\epsilon)\left(\frac{m-y/x}{m\,\epsilon}\right)$$
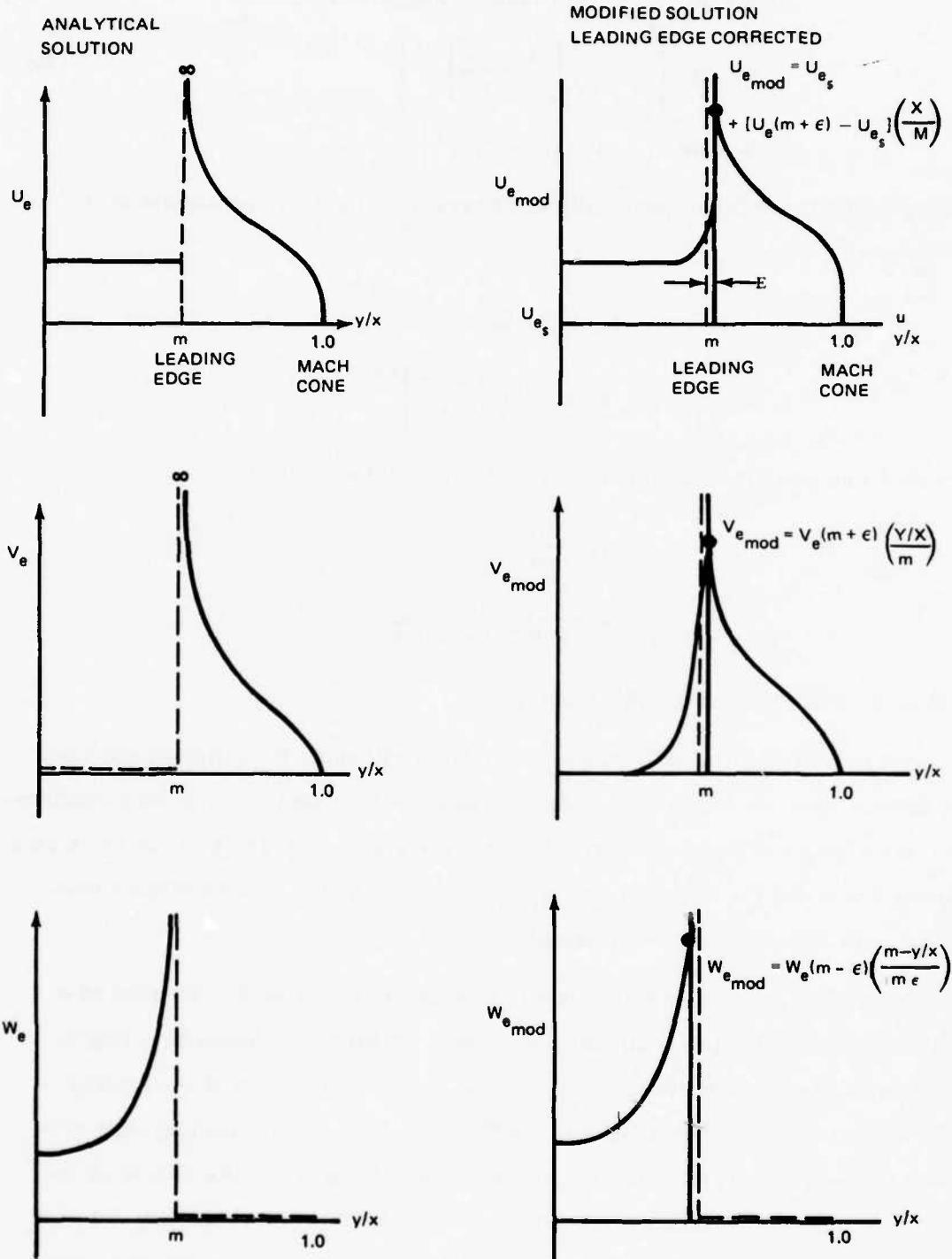
R80-1248-009W

Figure 12 Elliptical Cone Thickness Solution, Subsonic Leading Edge

40

nonlinear code for its starting solution. The shock was initially defined as the free-stream Mach cone about the elliptic cone.

In conjunction with the thickness solution, a lifting solution for a flat plate delta wing with subsonic leading edges can be found in Reference 12. The general solution for the entire Cartesian velocity field from the body to the Mach cone can also be expressed in complex form as,

$$
\begin{aligned}
u &= \mathrm{Re}\left[\left\{ \frac{m^2 \sin\alpha}{\beta E(K)} \right\} \{m^2 - \tau_2\}^{-1/2} \right] \\
v &= \mathrm{Re}\left[\left\{ \frac{\sin\alpha}{m\beta E(K)} \right\} \left\{ \frac{\tau}{(m^2 - \tau^2)^{1/2}} \right\} \right] \\
w &= \mathrm{Re}\left[\left\{ \frac{\sin\alpha}{E(K)} \right\} \left\{ \tau\left(\frac{1-\tau^2}{\tau^2 - m^2} \right)^{1/2} - E(\theta, K) \right\} \right]
\end{aligned}
\tag{54}
$$

This solution in linear combination with the solution for the velocity field about elliptic cones was used to represent an initial starting solution for the flow about a lifting delta wing. The Mach cone rotated at the angle of attack was used as an initial guess for the location and shape of the bow shock. In addition, leading edge corrections also were implemented to this solution to eliminate problems with the leading edge singularity associated with the linearized potential flow solution. To be consistent with Euler's equations, the exact expression for the pressure coefficient was used and the entire initial incremental entropy field was set to zero.

The useful aspect of employing a linearized starting solution is that lower free-stream Mach numbers and larger delta angles can be achieved which were not possible using the cone as a starting solution. In addition, as mentioned earlier, the entire entropy field developed gradually from the irrotational starting solution. This allowed for a better understanding of the development of the vortical singularities and their effect on the solution.

SECTION VIII

SPECIAL TECHNIQUES FOR CONICAL FLOW

1. CROSSFLOW SHOCK SHAPE

Several problems arose in the detection of crossflow shocks and in the transient shape of these shocks during the iterative marching technique used to obtain a conical solution to Euler's equations.

Figure 13 shows a schematic of a typical supersonic crossflow region. Since a crossflow shock can be detected anywhere along the sonic line between the symmetry plane and supersonic crossflow region, a shape criterion for the crossflow shock had to be imposed to ensure a stable computation.

The crossflow shock is located along the sonic line and its strength decays radially along this line. As the shock becomes weak, its shape basically follows the shape of the sonic line. The computational scheme assumes the shock is an M-grid line boundary (see Figure 14a). If weak crossflow shock points are detected whose shape significantly differs from the shape of an original M-grid line developed from the mapping, the original near orthogonality of the two-dimensional mesh will be disturbed, leading to an unstable computation and spurious numerical results. Thus, a shape criterion was imposed to eliminate this problem and retain a reasonable grid line arrangement. Crossflow shock shapes as shown in Fig. 14b promote a more stable computation.

During the iterative marching to a conical solution, certain transient and sometimes unstable phenomena occurred which were all associated with the vortical layer that builds up on the body surface. It was observed that the cross-flow shock point on the body would become displaced relative to the field shock points, as demonstrated by Figure 15a. Normally, the radial shock derivative at all field shock points is determined numerically using central difference formulae. It was found that this procedure, when implemented early during

42
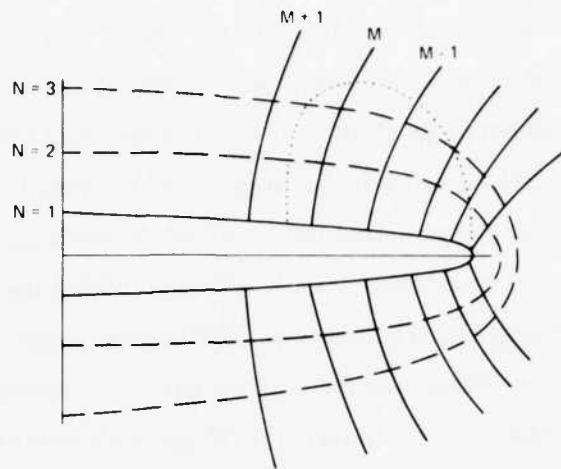
Figure 13 Grid Line Configuration Relative to Supercritical Region

(a) UNSTABLE GRID

(b) STABLE SHOCK SHAPE AND GRID
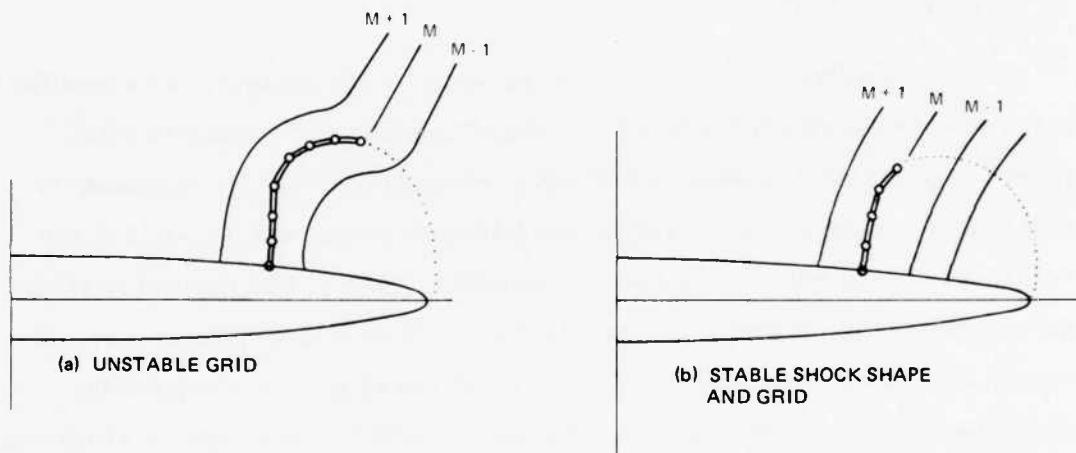
Figure 14 Detection of Stable Crossflow Shock Shape

(a) TRANSIENT SHOCK PRIOR TO CONVERGENCE

(b) INSTABILITY OF SHOCK DURING TRANSIENT
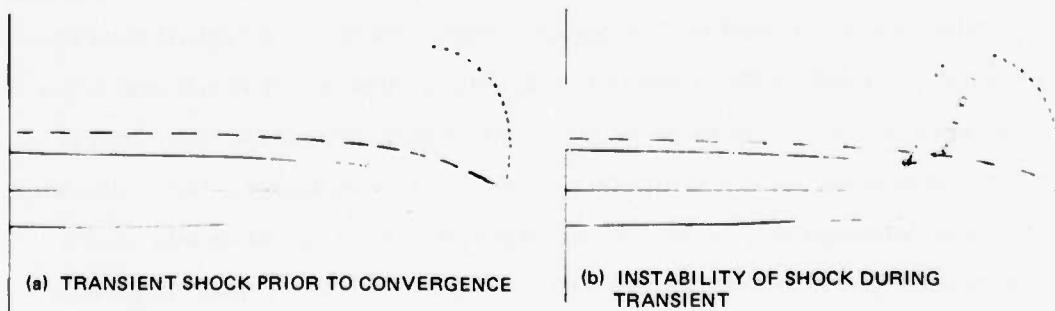
Figure 15 Shock Shapes During Iterative Process

43

the convergence process, could lead to an instability in the shock shape as demonstrated by Figure 15b. The field shock position would become unstable and travel into the supersonic region, become weak, and eventually fail to converge. It was determined later in the study that this problem was most probably caused by the buildup of a vortical layer on the body surface. This vortical layer cannot be resolved numerically without special consideration. Thus, it was necessary during the transient, while the shock points were moving to a converged location, to detach the field shock point derivatives from the location of the body shock point. An assumption on the direction of the shock normal in the cross sectional plane had to be prescribed. The shock normal in this plane was assumed to be tangential to the local N-grid line direction.

2. VORTICAL LAYER

Prior to convergence, certain problems arose in the pressure and crossflow Mach number distribution between the crossflow shock and symmetry plane. Severe oscillations developed in both pressure and crossflow Mach number in this region as soon as the crossflow shock became strong and approached convergence. To examine the problem, a numerical scheme was devised to allow the insertion of more grid points in this region. Two M-grid regions were assumed: one being the region between the windward symmetry plane and the crossflow shock, and the other being the region between the crossflow shock and leeward symmetry plane. Separating the grid into two regions allowed for different grid spacing in the two regions in the computational space. Thus, to investigate the problem between the crossflow shock and leeward symmetry plane, more points were inserted in this region. Figure 16 shows a typical distribution of pressure, crossflow Mach number, and entropy that would result just prior to convergence. Inserting more points in this region permitted resolution of any steep gradients. A large gradient in entropy was revealed. Near the shock, the entropy corresponded to the entropy being developed by the shock, and at the symmetry plane the entropy was still negligible. Thus, a wave in entropy was slowly traveling towards the leeward symmetry plane. The steep gradient in entropy was also causing the oscillations in both pressure and crossflow Mach

44
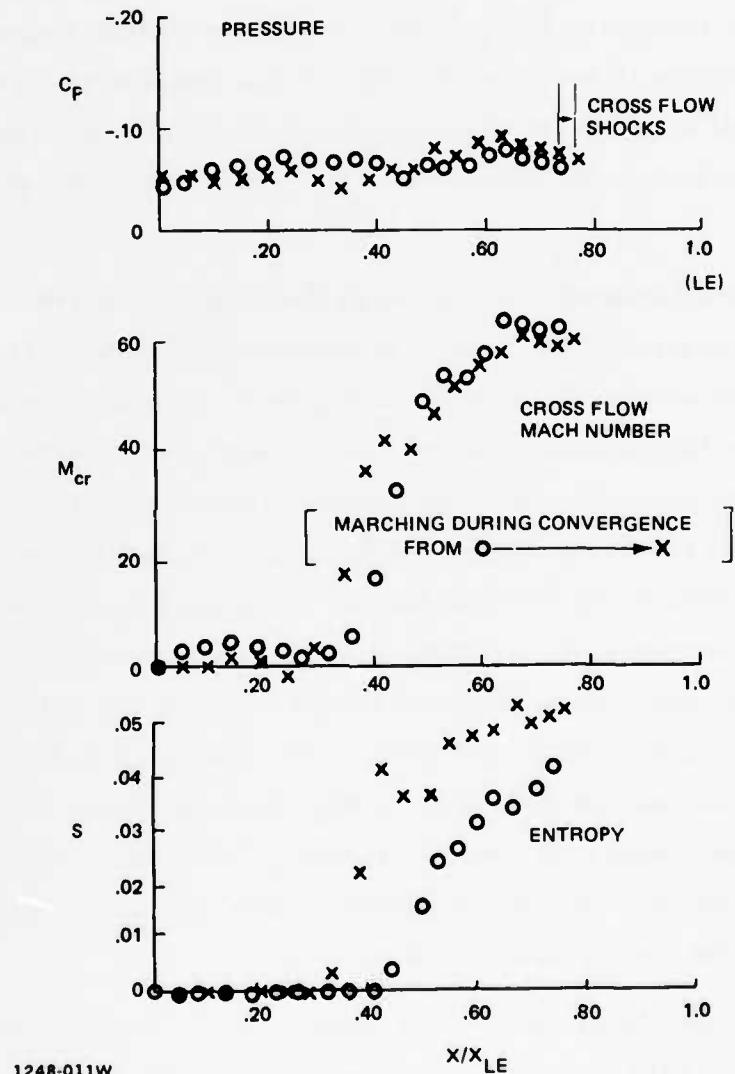
Figure 16 Development of Leeward Surface Vortical Layer, $M_\infty = 1.97$, $\theta = 18.39°$, $\delta = 3.17°$, $\alpha = 10°$.

1248-011W

45

number in this region. Since the body surface is a streamline, the entropy at
the shock must propagate to the symmetry plane, thus constituting the vortical
singularity. The computation was allowed to proceed in the hope that the en-
tropy would propagate to the symmetry plane, but the process turned out to be
too slow in converging since the entropy propagates at the crossflow velocity and
thus becomes an asymptotic process. Thus, a new computational technique
would be required to speed up this process, allowing the vortical singularity
to develop. In addition, a new computational technique would be required to
handle the vortical layer, and the discontinuity and large gradients in entropy
that would develop between the body surface and the first N-grid line off the
body.

Figure 17 shows a basic sketch of the vortical singularities and the entropy
field occurring with a crossflow shock. The entropy on the surface of the body
between the windward symmetry plane and low pressure side of the crossflow
shock comes from the stagnation streamline which originates at the bow shock.
The entropy on the body in Region II comes from the crossflow shock. A strong
vortical singularity is developed in the leeward symmetry plane on the body.
Here, the body surface is a streamline and the entropy must be equal to that
on the high pressure side of the crossflow shock. At the first field point in the
leeward symmetry plane, the entropy must be that corresponding to the entropy
of the streamline coming from the bow shock. At a high enough angle of attack,
a discrete bow shock does not exist in the leeward symmetry plane, and thus
the entropy is zero. Hence, the vortical singularity corresponds to the jump
in entropy on the body developed by the crossflow shock and the entropy, if any,
developed across the leeward plane bow shock point.

To resolve this singularity and to speed up the process of the entropy de-
velopment on the leeward symmetry plane from the crossflow shock, a new com-
putational technique was developed. This scheme is only imposed when the
crossflow shock attains maximum strength and is close to convergence. The
entropy on the body between the leeward symmetry plane and the crossflow
shock is set equal to the entropy at the crossflow shock. At the first N ring

46

1248-012W
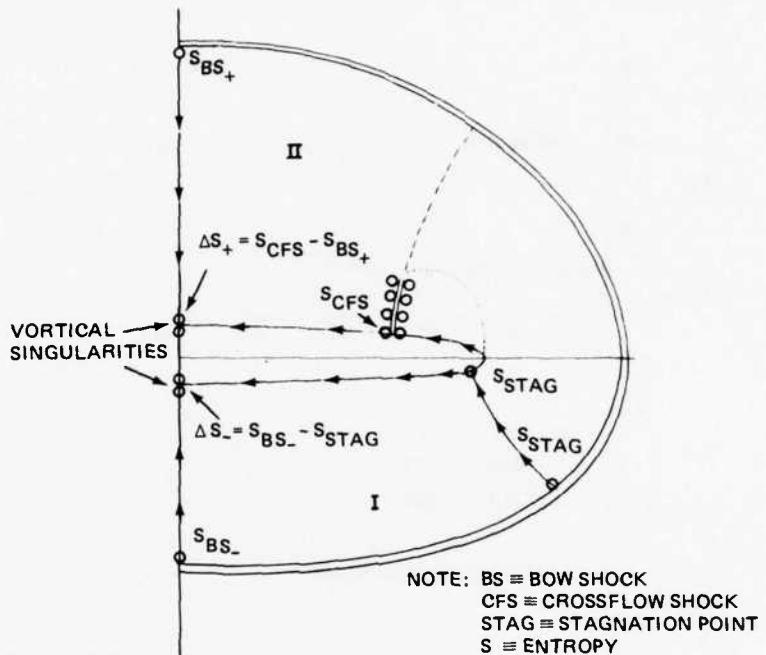
Figure 17 Basic Sketch of Flow Field

off the body, outward difference numerical derivatives in the radial direction
are used. The entropy on the body is undisturbed by the first field ring since
the coefficients of its normal derivatives are zero. The entropy at the field
ring is unaffected by the body entropy because of the windward differencing in
the radial direction at this ring. All other field points are still computed using
central difference formulas.

To eliminate the oscillations in pressure and cross flow developed as a re-
sult of the steep entropy gradient between the shock and symmetry plane, a one-
step numerical damping or artificial viscosity was imposed in this region.
Some typical results are shown in Figure 18 for the leeward side of the body.
As indicated by the figure, when this procedure was adopted the results im-
proved markedly. Both the pressure and crossflow are smooth and show no
oscillations. The entropy distribution shows a discrete jump, representing the
vortical singularity, from the body surface to the first field ring. In addition,
a discrete jump in radial velocity also occurs at the vortical singularity.

47
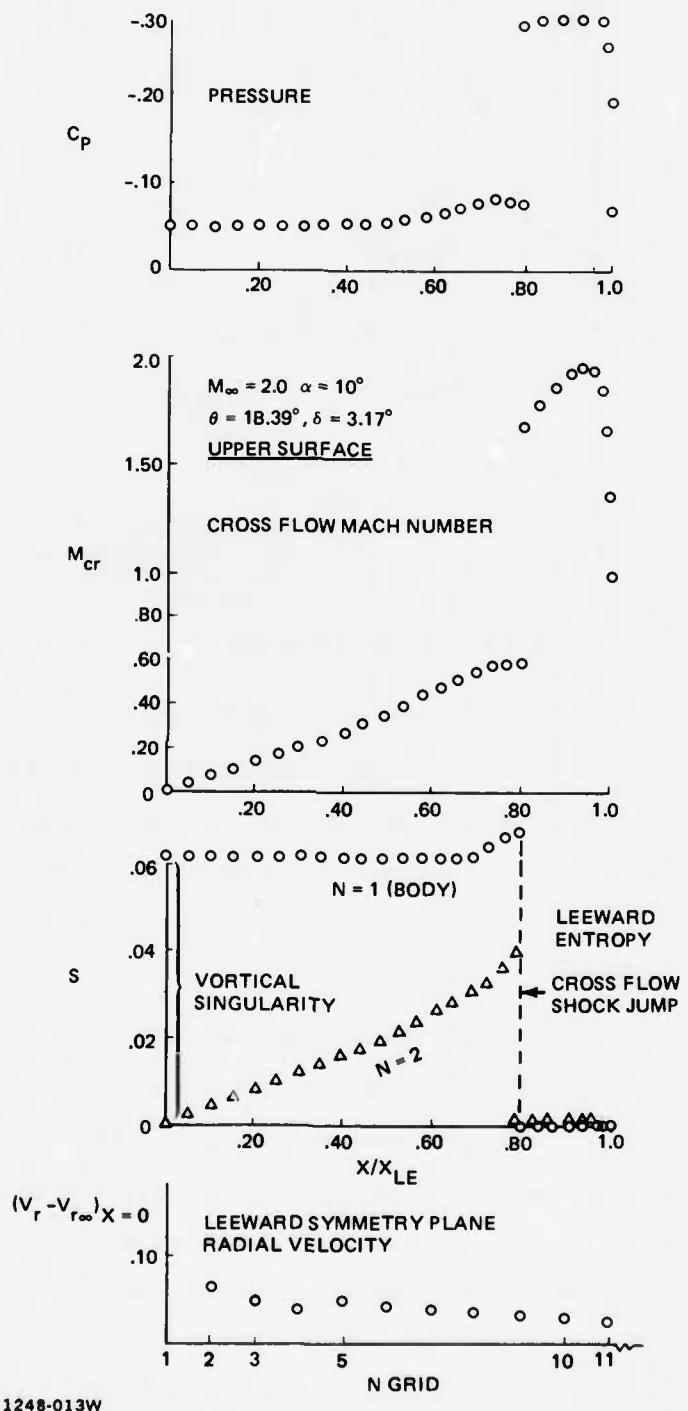
Figure 18   Improved Numerical Results

1248-013W

SECTION IX

GEOMETRY

1. ANALYTICAL SPANWISE CONICAL DEFINITION

A geometry definition based on simple conical parameters was developed and was found to be very useful in defining both conical and three-dimensional wings. The cross section was simply defined as the superposition of a span-wise thickness and camber distribution. The cross section was restricted to spanwise elliptical thickness and circular arc camber. In a subsequent section, a more flexible geometry package is described for general three-dimensional wings with chordwise definition.

In this analytical representation of the wing geometry, the geometric parameters are specified as parametric angles. Thus, a wing cross section can be entirely specified by five angles: δ_F, δ_E, δ_T, δ_{TC}, δ_P. The symbols δ_F, δ_E and δ_T represent planform angles defining the body lines of the delta wing, δ_P an angle controlling the centerline thickness variation, and δ_{TC} the leading edge camber angle in the cross sectional plane (see Figure 19). Cubic equations are used to curve fit the angles in the general form:

$$\delta(z) = a(z - z_0)^3 + b(z - z_0)^2 + c(z - z_0) + d$$

The spatial location of the body lines can then be simply defined as:

$$x = z \tan(\delta(z))$$

The thickness of the wing was assumed elliptical but was allowed to have an inboard flat section. The camber line, defined separately, was also allowed to have a flat inboard section with a circular arc camber line to the leading edge. To define the maximum camber and twist of the cross section, a leading edge camber angle is specified (δ_{TC}). The thickness and camber flats are defined separately and, thus, do not have to coincide. The wing cross sectional geometry was then simply defined by adding and subtracting the thickness to the camber line.

49

SIDE VIEW

PLANFORM

CROSS SECTION

THICKNESS

FLAT

ELLIPTICAL

x_E

x_T

CAMBER

FLAT

x_T

x_F

CIRCULAR ARC

δ_{TC}
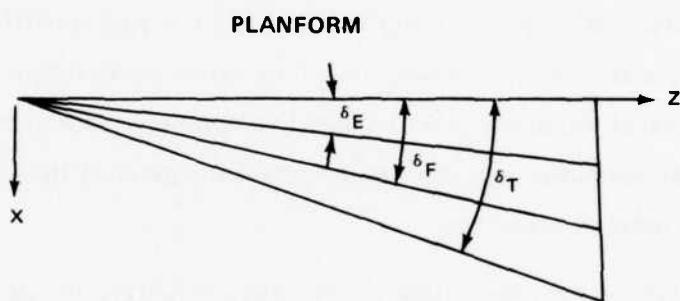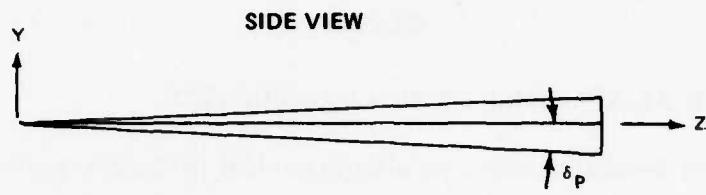
CONICAL CROSS SECTION
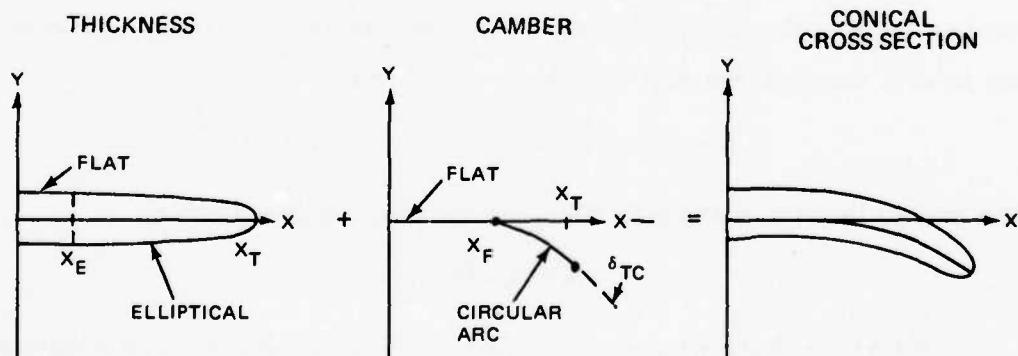
Figure 19 Geometrical Parameters Used in Defining Conical Wings

1248-014W

50

All first derivatives of the surface could then be defined analytically through the surface normal vector. The entire conical wing was then defined by three continuous wing sections. The geometry definition was flexible enough to allow the initial section to begin as a circular cone. The cone was then deformed continuously through two wing sections. The third section represented the invariant conical portion of the wing. The parametric definitions remained unchanged for all three wing sections, with only the coefficients of the cubic angle equations varying from one section to another.

As an example, for a simple three-dimensional elliptical cross section wing, the surface normals would be defined from the parametric cross section equation,

$$y = P_t(z) [x_T^2(z) - x^2]^{1/2}$$

where $P_t(z)$ is a cubic centerline thickness function and $X_T = z \tan \delta_T(z)$ where δ_T is a cubic planform angle function in Z. The surface in three dimensions can then be defined simply as,

$$F(x, y, z) = y - f(x, z)$$

and the surface normal vector as,

$$\vec{n} = (\hat{i}_y - f_x \hat{i}_x - f_z \hat{i}_z)/(1 + f_x^2 + f_z^2)^{1/2}$$

Figure 20a shows an example of the body line variation to achieve a cambered wing cross section. Figure 20b shows an example of the cross sectional deformation of a circular cone to an elliptical cross section. Figure 20c further shows the deformation from an elliptical to a cambered cross section.

It was a trivial task later in the study to add additional sections to the wing. The present capability of the geometry allows for variation from a circular cone to a conical wing, then an additional variation to a second conical wing.

51

BODY LINE DEFORMATION TO CONICAL WING
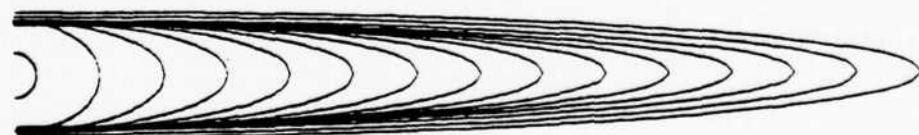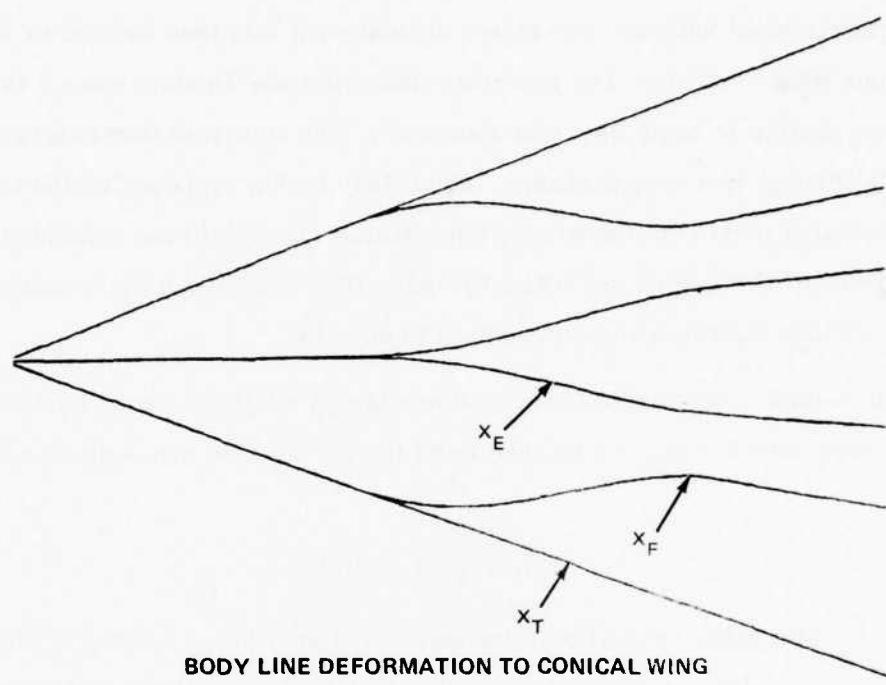
ELLIPTICAL CROSS SECTION

GENERAL CAMBERED WING

1248-015W

Figure 20 Wing Analytic Geometries

52

A wing-body capability was then added to the second conical wing section. This was achieved by allowing for a cubic body section that follows a body line. Thus, the last section of the wing can be a conical wing or wing-body. Figure 21 shows a sketch of the parameters that control the body development. Thus, this geometry package can be used for conical wings, conical wing-bodies, and, if done properly, for an entire three-dimensional wing-body vehicle. Figure 22 shows an example of the usage of this capability for computing a conical wing-body solution commencing with a conical wing cross section.

2. SURFACE PATCH GEOMETRY

The analytical geometry programs described in the previous section were an advantageous device for computing results for a variety of wing shapes where the geometrical parameters could be computed exactly and without numerical errors. Unfortunately, not all wing shapes fall into the category of these programs, and a more flexible geometry program was desirable.

A geometry program was desired which could analytically simulate very complex wing shapes with a minimum of errors. After some investigation, the bi-cubic surface patch formulation, developed in Reference 13 and put to practical use in describing aerodynamic vehicles in Reference 10, was found to be an adequate procedure. The equation for the Cartesian coordinates of a surface bi-cubic patch can be written, in terms of parametric variables u & w (using matrix notation) as (see Figure 23):

$$x = [u^3 \ u^2 \ u \ 1] \ [S_x] \begin{bmatrix} w^3 \\ w^2 \\ w \\ 1 \end{bmatrix} \quad \text{(a)}$$

$$y = [u^3 \ u^2 \ u \ 1] \ [S_y] \begin{bmatrix} w^3 \\ w^2 \\ w \\ 1 \end{bmatrix} \quad \text{(b)} \quad (55)$$

$$z = [u^3 \ u^2 \ u \ 1] \ [S_z] \begin{bmatrix} w^3 \\ w^2 \\ w \\ 1 \end{bmatrix} \quad \text{(c)}$$

53
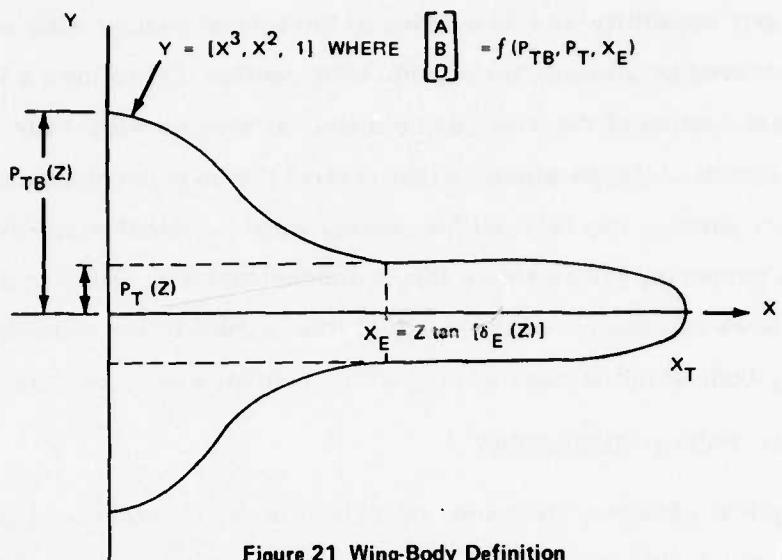
Figure 21 Wing-Body Definition
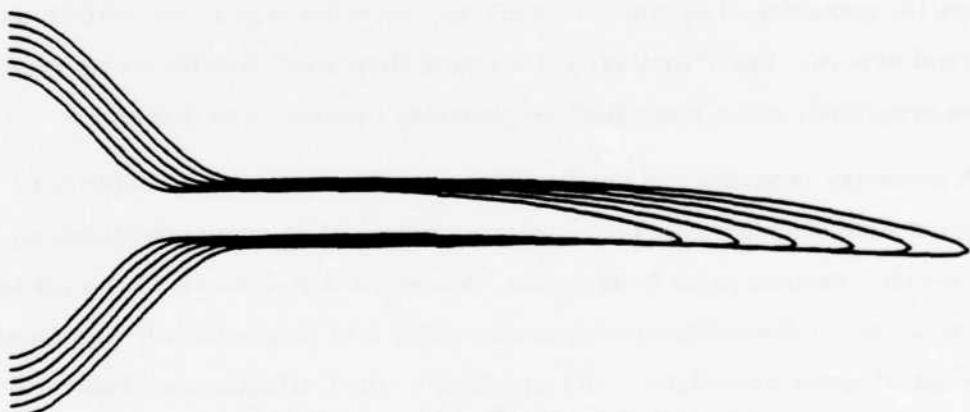
Figure 22 Example of Wing-Body Geometry Generation
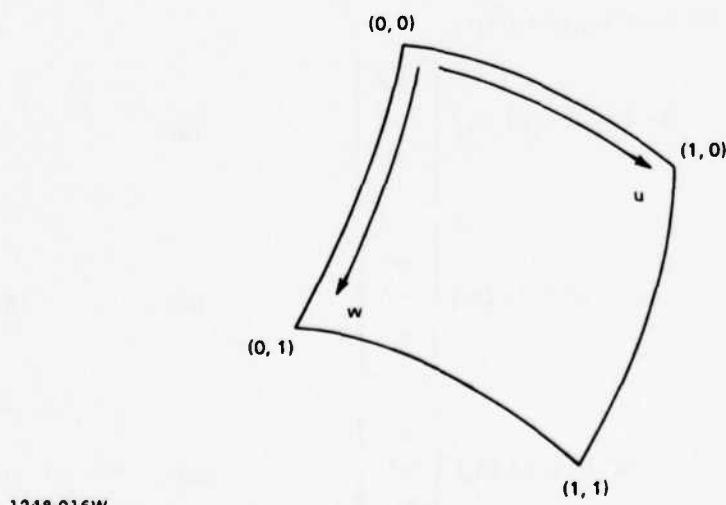
Figure 23 Bi-Cubic Surface Patch

1248-016W

54

where

$$S_i = M B_i M^t, \quad i = x, y, z$$

or, in vector notation,

$$V = [x \, y \, z] = USW^t$$

The boundary condition matrix B is a 4×4 matrix containing the four corner point spatial and derivative information. The matrix M is a constant matrix derived from the desired blending functions. The computer code described in Reference 10 uses the patch theory developed in Reference 12 for the geometry of complex aerodynamic vehicles. The code uses the Harris geometry input data format that is commonly used by aerodynamicists. The wing sections are defined chordwise for each span location. Spline fitting provides the necessary information for developing the boundary matrices B for each patch.

The computer code described in Reference 10 was extensively modified and incorporated into the finite difference code. The finite difference procedure requires the surface coordinate y and surface normal vector components at a given axial location z and span location x of the wing. Thus, with two of the Cartesian coordinates specified, equations (55a) and (55c) yield two simultaneous bicubic equations for u and w that must be solved iteratively. The solution is accomplished quickly by a Newton iterative method for two simultaneous equations and an error extrapolation scheme.

Thus, if

$$F(x, u, w) \equiv x - f(u, w)$$

$$G(u, w) \equiv z - g(u, w)$$

and   (56)

$$u_{i+1} = u_i + \delta$$

$$w_{i+1} = w_i + \epsilon$$

55

where

$$\delta = - \frac{\begin{pmatrix} F_i & F_{wi} \\ G_i & G_{wi} \end{pmatrix}}{\dfrac{\partial(F,G)_i}{\partial(u,w)}} \quad ; \quad \epsilon = \frac{\begin{pmatrix} F u_i & F_i \\ G u_i & G_i \end{pmatrix}}{\dfrac{\partial(F,G)_i}{\partial(u,w)}}$$

and u_i, w_i are an initial guess or subsequent iterations until a convergent solution has been attained.

Determining u and w explicitly defines the surface coordinates y from equation (55). The surface normals at the point are then determined by the cross product of the two tangent vectors given by

$$\vec{U}_t = \left[\frac{\partial x}{\partial u}, \ \frac{\partial y}{\partial u}, \ \frac{\partial z}{\partial u} \right]$$

$$\vec{W}_t = \left[\frac{\partial x}{\partial w}, \ \frac{\partial y}{\partial w}, \ \frac{\partial z}{\partial w} \right]$$

(57)

and

$$\vec{N} = \vec{U}_t \times \vec{W}_t$$

where

$$N_x = \begin{pmatrix} \dfrac{\partial y}{\partial u} & \dfrac{\partial z}{\partial u} \\ \dfrac{\partial y}{\partial w} & \dfrac{\partial z}{\partial w} \end{pmatrix} = \frac{\partial(y, z)}{\partial(u, w)}$$

$$N_y = \frac{\partial(z, x)}{\partial(u, w)}$$

$$N_z = \frac{\partial(x, y)}{\partial(u, w)}$$

In terms of practical usage, Figure 24 shows an example of a delta wing modeled using bi-cubic surface patches. Each patch equation requires a $(4 \times 4 \times 3)$ matrix of boundary condition information. The core requirements necessary to store all the patch matrices are beyond practicality. Thus, the patch matrices are written on an external device and only local blocks of patch matrices are stored in the vicinity of the axial station being currently computed.
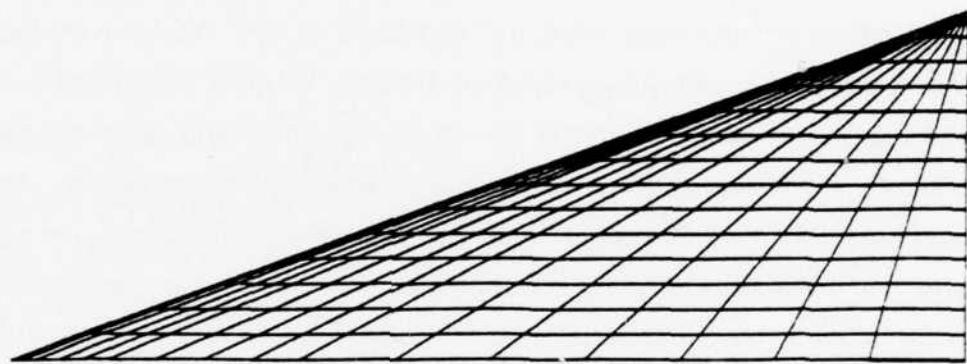
1248-017W

Figure 24 Panel Model of Delta Wing

SECTION X

## DISCUSSION OF RESULTS

1. CONVERGENCE

The axial variation of surface pressure, in the symmetry plane and at the wing tip, is shown in Figure 25; the geometry is a 6:1 elliptic cone, and the free stream conditions are $M_\infty = 1.97$, and $\alpha = 0$. The iteration was started at $Z = 0.1$ with a circular cone solution of half angle $18.39°$. The geometrical deformation expands and recompresses the flowfield between $Z = 0.1$ and $Z = 1.0$ and the geometry becomes conical at $Z = 1.2$. The symmetry plane and tip pressures are both converged at $Z = 4$. Figure 25 shows that these values continue to remain invariant. At zero angle of attack, the two pressure levels are a good indication of the convergence of the flowfield on the body. For these results, a 20×25 radial by circumferential grid was used. Figure 26 is a comparison of the computed spanwise pressure distribution with the experimental data of Jorgensen, Reference 7. In addition, the second order result of Van Dyke, Reference 15, is also shown.

At angles of attack high enough to produce a crossflow shock, the shock pressure jump and position were studied to determine convergence. Figure 27a shows the axial distribution of the surface pressure in the windward and leeward symmetry planes and the high and low pressure side of the crossflow shock. The configuration was the same 6:1 ellipse and the free stream conditions were $M_\infty = 1.97$ and $\alpha = 10°$. Figure 27a shows all these pressure levels to be converged after $Z = 3.0$. Figure 27b shows the cross sectional surface pressure distribution and geometry. For computations at angle of attack, a 25×35 grid was generally used. The results of the computations at the higher angles of attack ($\alpha \geq 10°$) exhibited pressure oscillations on the high-pressure side of the crossflow shock, as shown in Figure 27b and later in this section. These oscillations seem to be generated at the vortical singularity and move

58

R80-1248-018W
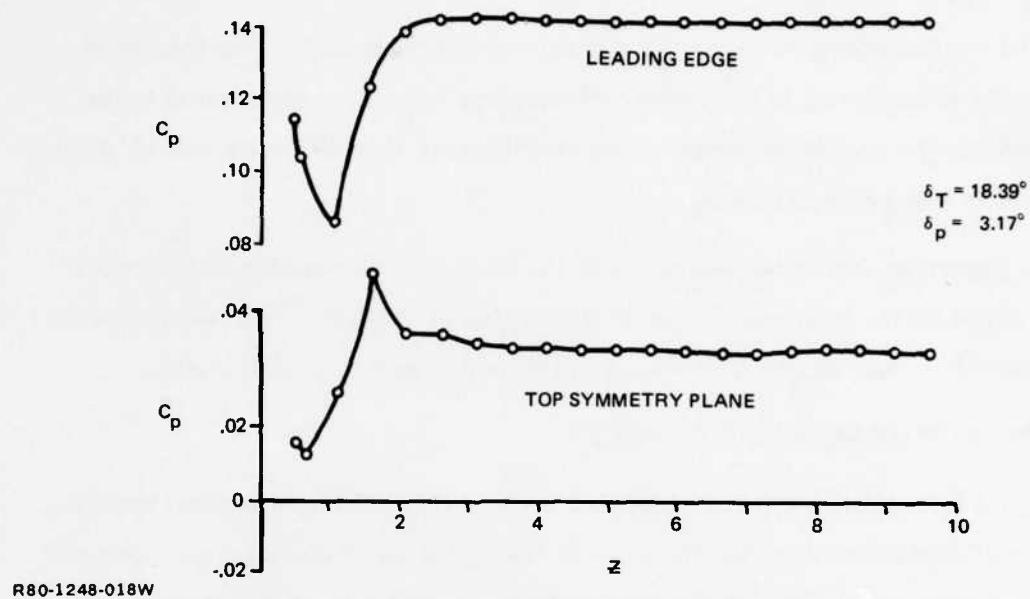
Figure 25 Axial Variation of Surface Pressure, Elliptic Cone (a/b = 6), M_∞ = 1.97, α = 0

R80-1248-019W
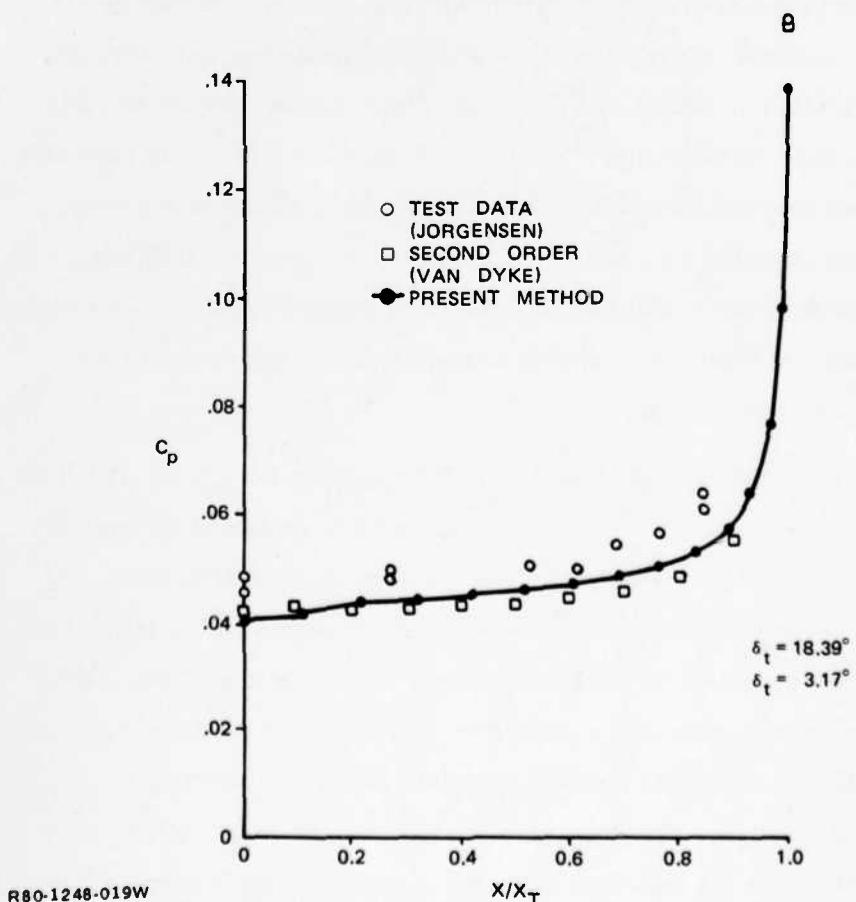
Figure 26 Comparison with Experimental Data and Second Order Theory, Elliptic Cone
(a/b = 6), M_∞ = 1.97, α = 0.

59

toward the crossflow shock as the computation is continued. The amount of difficulty encountered in the computation seems to be directly related to the strength of the crossflow shock. The resolution of this difficulty will be demonstrated in subsequent results.

Figure 28 shows the plan view of the wing and the position of the crossflow shock on the body which was first detected at $Z = 0.75$. The shock position approaches a conical ray at $Z = 2.3$ and thereafter remains on that ray.

2. EFFECT OF SPANWISE CAMBER

As a preliminary investigation of the possible effects of conical camber, the flowfields about several wings with various forms of circular arc spanwise camber were computed. In Figure 29, the computed spanwise pressure distributions are presented for a symmetrical elliptical wing, a wing with half semi-span circular arc camber, and a wing with circular arc camber over its entire semi-span at zero angle of attack and $M_\infty = 2.0$. Both camber lines terminate with a 20° leading edge camber angle. The conical camber effectively results in leading edge droop and thus reduces the effective angle of attack of the wing, resulting in a corresponding loss in lift. The pressure distribution of Figure 29 confirms this expected result with higher pressures being computed on the upper surface. The pressure distributions also indicate a slight movement of the stagnation point to the upper surface.

Figure 30 shows the computed pressure distributions for a wing with half semi-span circular arc camber and leading edge camber angles of 20° and 30°. Figure 31 shows the corresponding crossflow Mach number distributions. At 20° camber, a small region of supercritical flow is developed on the lower surface of the wing in the vicinity of the leading edge. At 30° camber, this region becomes more extensive, reaching a crossflow Mach number of 1.4 and causing a crossflow shock to form on the lower surface at a span location 10% inboard from the wing leading edge. This type of behavior brought on by rather large camber angles can cause the boundary layer to separate on the lower surface

60

(a) AXIAL DISTRIBUTION

(b) CROSS-SECTIONAL DISTRIBUTION

C_p

X WINDWARD SYMMETRY PLANE PRESSURE
O LEEWARD SYMMETRY PLANE PRESSURE
□ LOW PRESSURE SIDE OF SHOCK
● HIGH PRESSURE SIDE OF SHOCK

$\delta_p = 3.17$
$\delta_T = 18.39$

Y/XT

X/XT
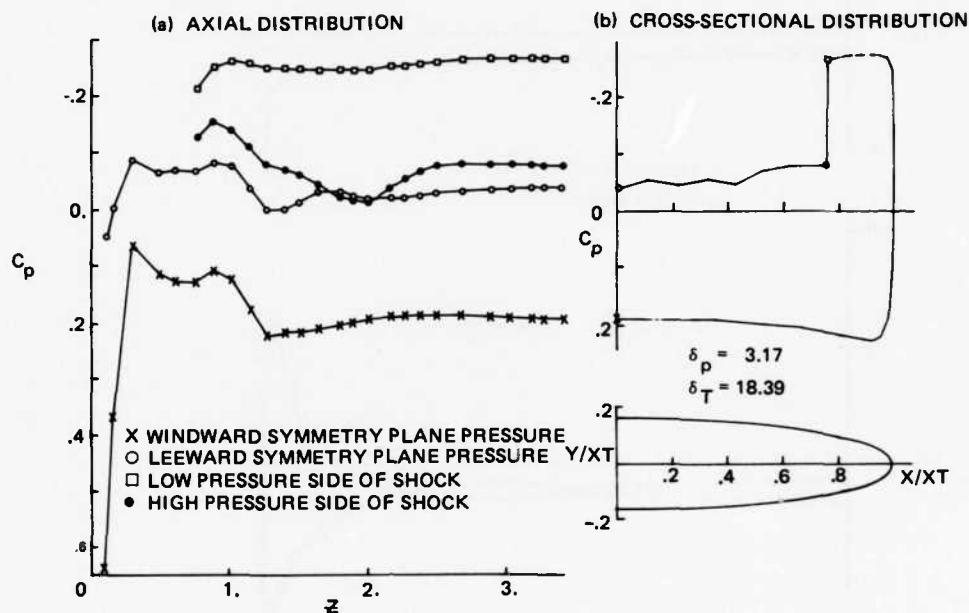
R80-1248-020W

Figure 27 Surface Pressure, Elliptic Cone
(a/b~6) $M_\infty = 1.97$, $\alpha = 10°$

X

WING LEADING EDGE

CONVERGED SHOCK
LOCATION, CONICAL RAY

CROSS FLOW SHOCK
LOCATION

Z
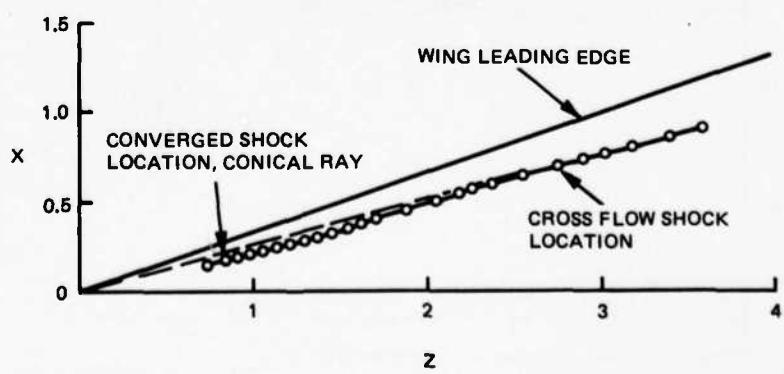
R80-1248-021W

Figure 28 Planform View of Wing and Surface Shock,
(a/b~6), $M_\infty = 1.97$, $\alpha = 0°$

61
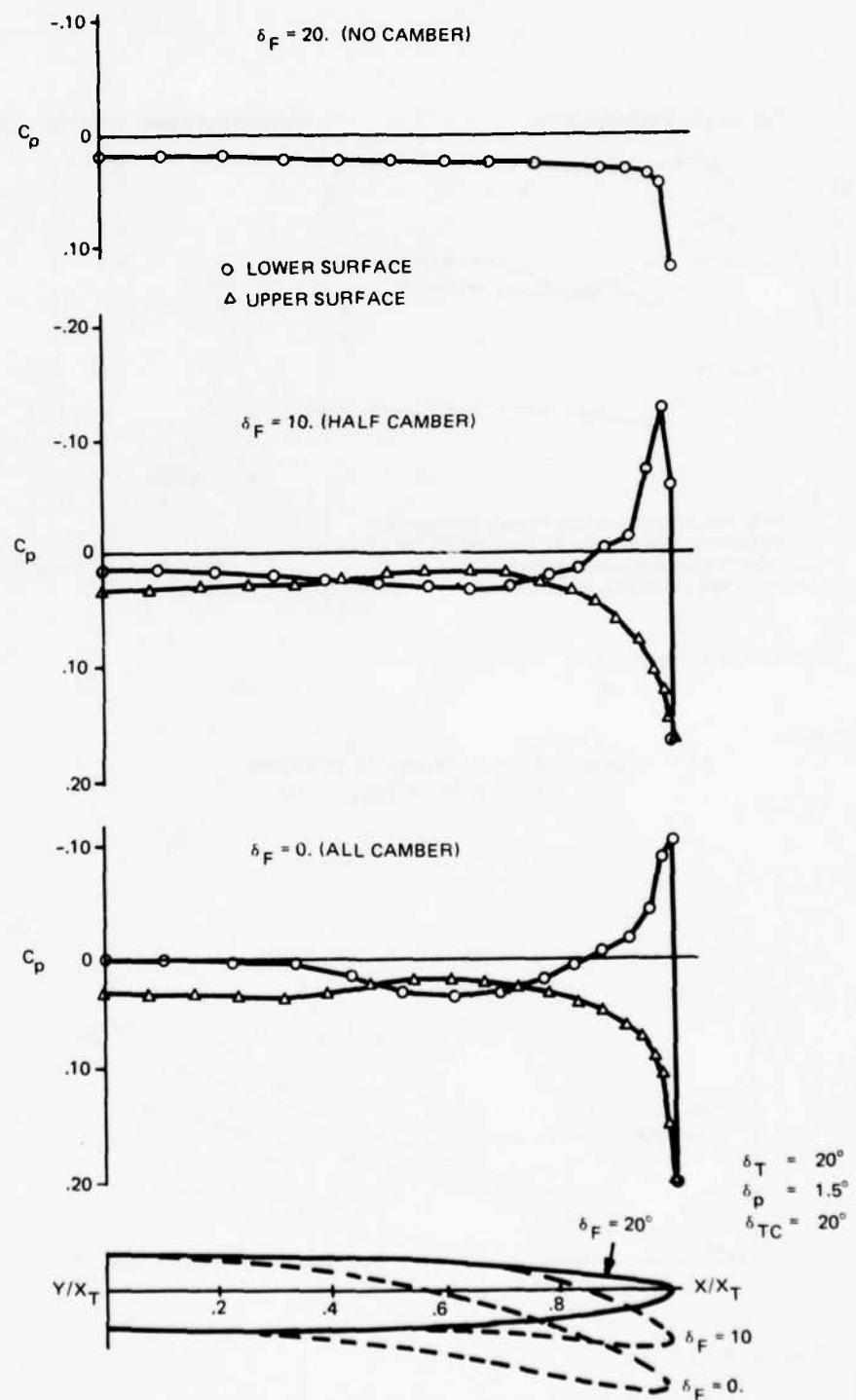
Figure 29 Effect of Spanwise Camber on Pressure Distribution, $M_\infty = 2, \alpha = 0$

R80-1248-022W

62
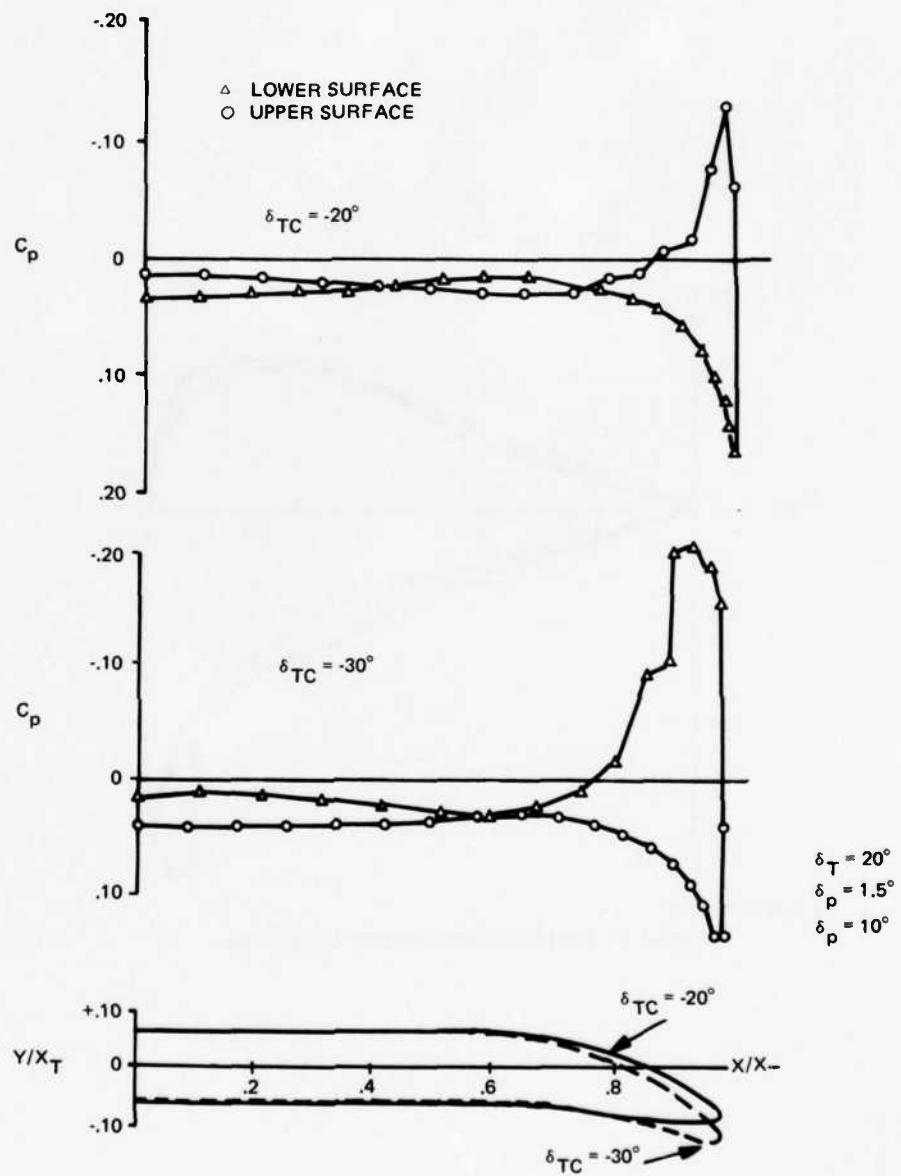
R80-1248-023W

Figure 30 Surface Pressure Comparison, $M_\infty = 2$, $\alpha = 0$

63

R80-1248-024W
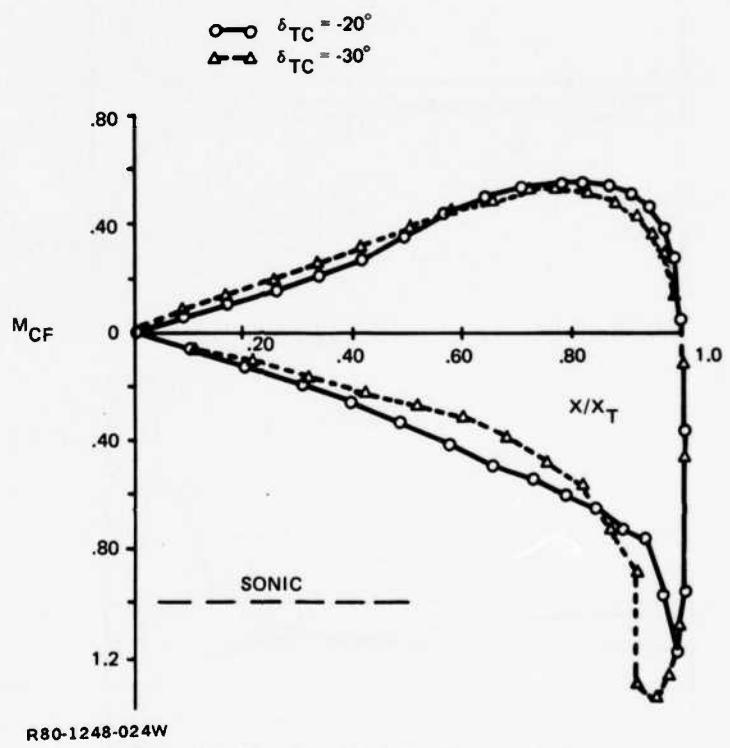
Figure 31 Crossflow Mach Number Comparison

64

of the wing at small angles of attack. Leading edge separation on the lower surface was detected experimentally in Reference 15.

Figures 32 and 33 show the effect of full semi-span circular arc camber on the spanwise pressure distribution for two wings with different cross-sectional thicknesses. Figure 32 shows a 14:1 elliptical wing at $\alpha = 3°$. The symmetrical wing develops a supercritical region on the upper surface and forms a small crossflow shock at the end of a rather steep compression. The effect of cambering the wing is to completely eliminate the suction peak and corresponding supercritical region in the vicinity of the leading edge. Figure 33 shows a similar result for an 18:1 elliptical wing at $\alpha = 2.5°$. The symmetrical wing in this case develops a somewhat stronger shock, which is located closer to the leading edge. Cambering this wing also completely eliminates the supercritical region near the leading edge. In both cases, a loss in lift accompanies the camber effect. An improvement in the drag characteristics might be expected as a result of a thrust acting on the forward-facing area of the wing, produced by the leading edge droop. In any event, an apparent delay in the formation of the crossflow shock is apparent.

3. COMPARISON WITH LINEARIZED POTENTIAL FLOW THEORY

The failure of linearized theory in the vicinity of the leading edge of wings is well known. Figures 34 and 35 show a comparison between the nonlinear computed results and the results of the linearized panel method of Reference 16. Overall good correlation is achieved at these low angles of attack except in the vicinity of the leading edge. In Figure 34 the linearized results depart sharply from the nonlinear at approximately 95% span. The symmetry plane pressures correlate reasonably well and the loading or Cp is in excellent agreement over most of the wing. In Figure 35 the agreement in pressures on the upper surface is not as good as for the thinner wing.

Figures 36 and 37 show the same conditions as Figures 34 and 35 but with spanwise camber. Linearized theory predicts the reduction of the upper surface pressures and is in excellent agreement with the nonlinear results. Some

65
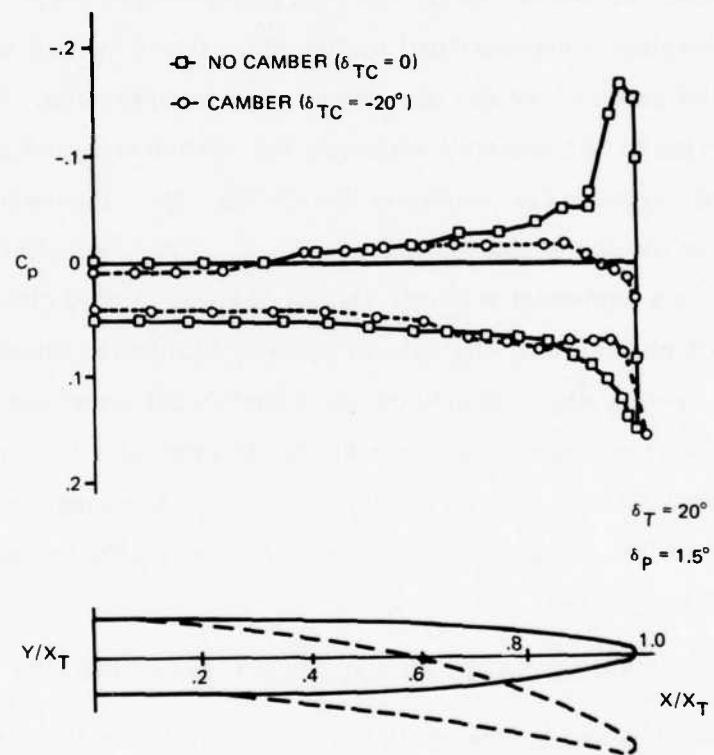
R80-1248-025W

Figure 32   Comparison of Lifting Pressure Distribution with and without Camber for
14:1 Elliptical Wing, M_∞ = 2.0, α = 3°

66
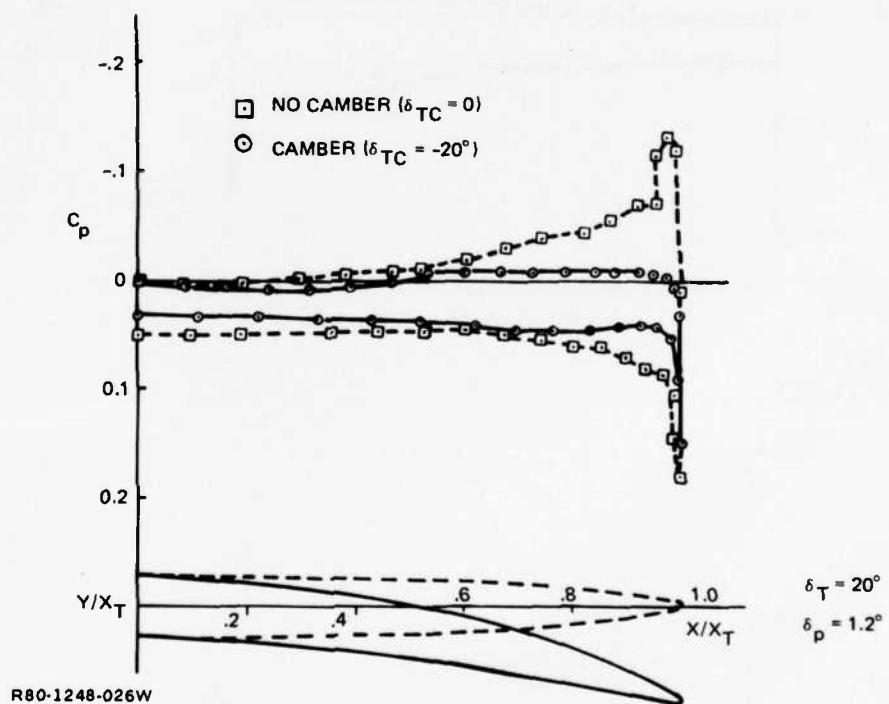
Figure 33 Comparison of Lifting Pressure Distribution with and without
Camber, $M_\infty = 2.0$, $\alpha = 2.50$

R80-1248-026W

67
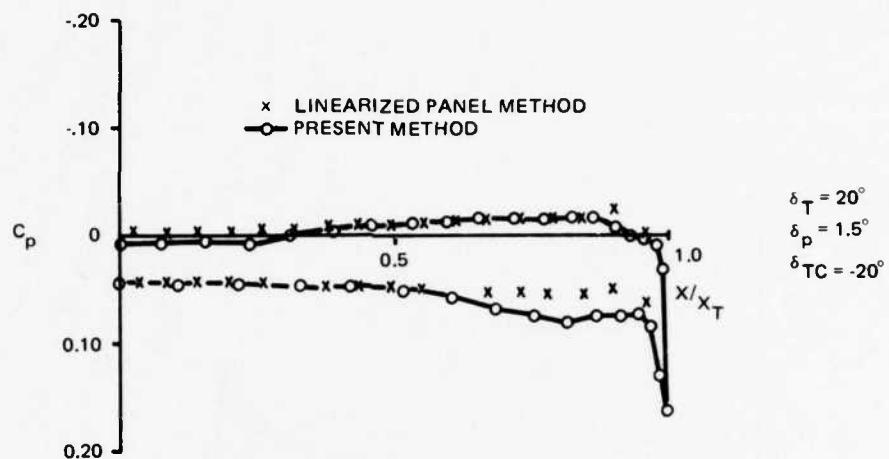
R80-1248-027W Figure 34 Spanwise Pressure Distribution Cambered
From Root, $M_\infty = 2.0$, $\alpha = 3°$
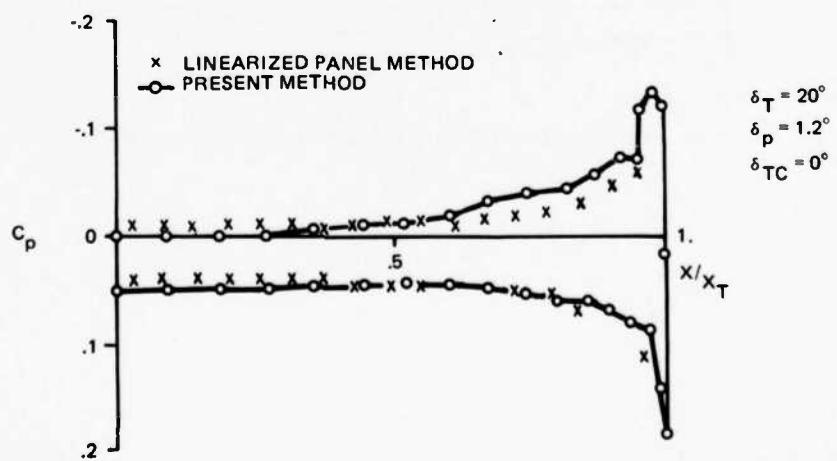
R80-1248-028W

Figure 35 Spanwise Pressure Distribution, No Camber, $M_\infty = 2$, $\alpha = 3°$
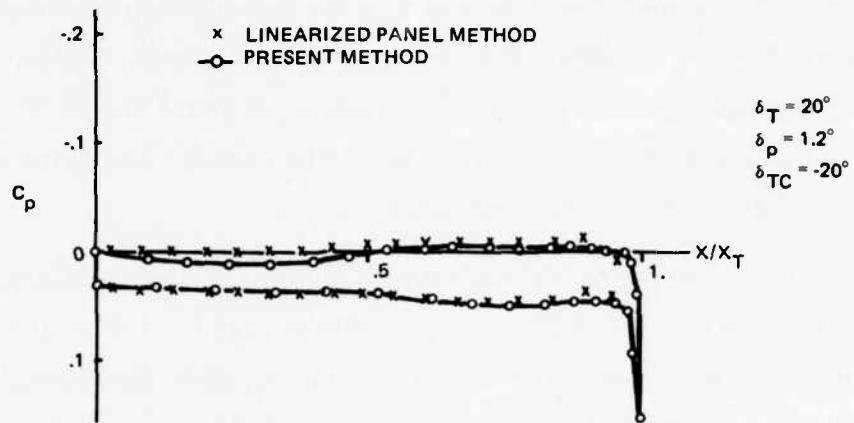
R80-1248-029W

Figure 36 Spanwise Pressure Distribution, Cambered from Root $M_\infty = 2$, $\alpha = 2.5°$
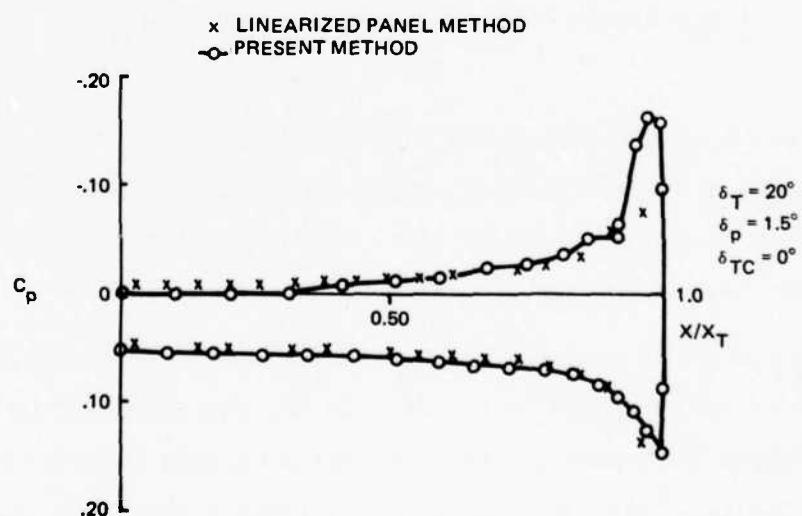
R80-1248-030W

Figure 37 Surface Pressure, No Camber, $M_\infty = 2.0$, $\alpha = 3°$

discrepancy in the lower surface pressure exists. Figure 38 shows a comparison of the two methods at 10° angle of attack for a symmetrical elliptic wing. Linearized theory breaks down completely in the region of supercritical flow. The upper surface or leeward pressures are in fair agreement between the shock and symmetry plane. The pressures on the windward side of the wing are underpredicted by the linearized method. The loading between the shock and the symmetry plane is also somewhat underpredicted.

From these comparisons it can be seen that the breakdown of linearized methods is primarily localized to the supercritical regions of these flows. Linearized methods cannot predict the existence of a crossflow shock because this effect is inherently nonlinear. Nonlinear prediction techniques can be used to evaluate the beneficial effects of aerodynamic devices like spanwise camber.

The lengthy process employed with the cone as a starting solution had the geometry first deform to the desired conical cross section. The flowfield then first converges on the body solution and eventually on the entire flow field. The linearized solution allows starting with the desired conical cross section with no geometrical deformation. The bow shock converges first and then the entire flowfield.

The useful aspect of employing a linearized starting solution is that lower free stream Mach numbers and larger delta angles can be achieved than were possible using the cone as a starting solution. Most of the following results were obtained using a modified linearized potential flow solution.

Figure 39 shows the converged shock shape, in comparison with the Mach cone, for a 30° delta wing at $M_\infty = 1.8$, $a/b = 22.05$. The computed bow shock shows the largest difference at the leading edge of the wing where the Mach cone is close to the tip. Figure 40 shows the convergence history of the bow shock and body pressures for a 20° delta at $M_\infty = 2.0$. The wing bow shock converges quite rapidly and the body pressure follows.

-x- LINEARIZED PANEL METHOD
-o- PRESENT METHOD
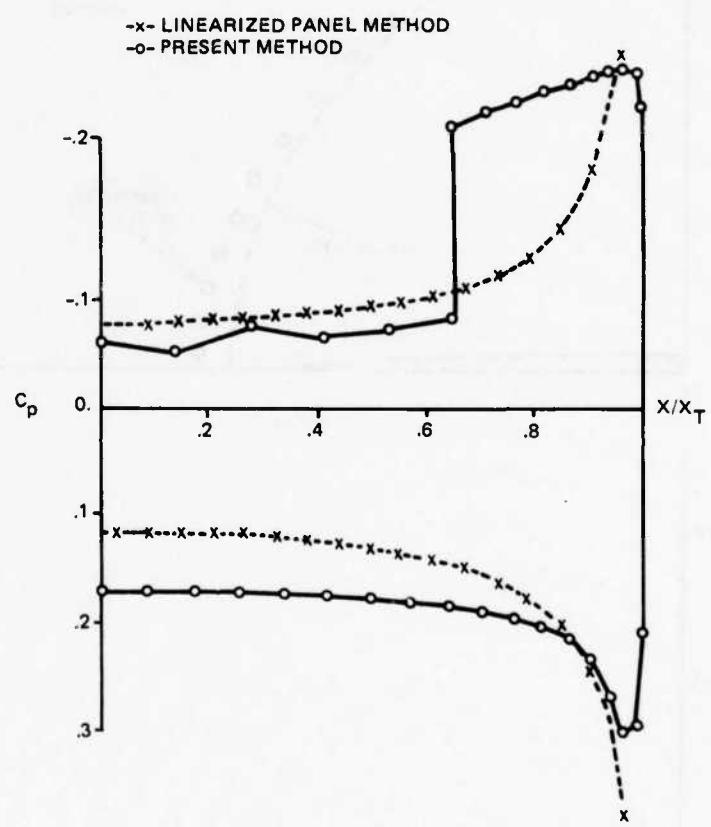
R80-1248-031W

Figure 38 Spanwise Pressure, No Camber, $M_\infty = 2$, $\alpha = 10°$

71

30° DELTA WING

$M_\infty = 1.8$, $\alpha = 0°$, $a/b \approx 22$

$a/b \sim 22$

Y/Y_{LE}

1.0

MACH CONE

COMPUTED SHOCK

0   .10

X/X_{LE}

SURFACE PRESSURE DISTRIBUTION, C_p

.30

.20

1.0

0   .20   .40   .60   .80   1.0

X/X_{LE}
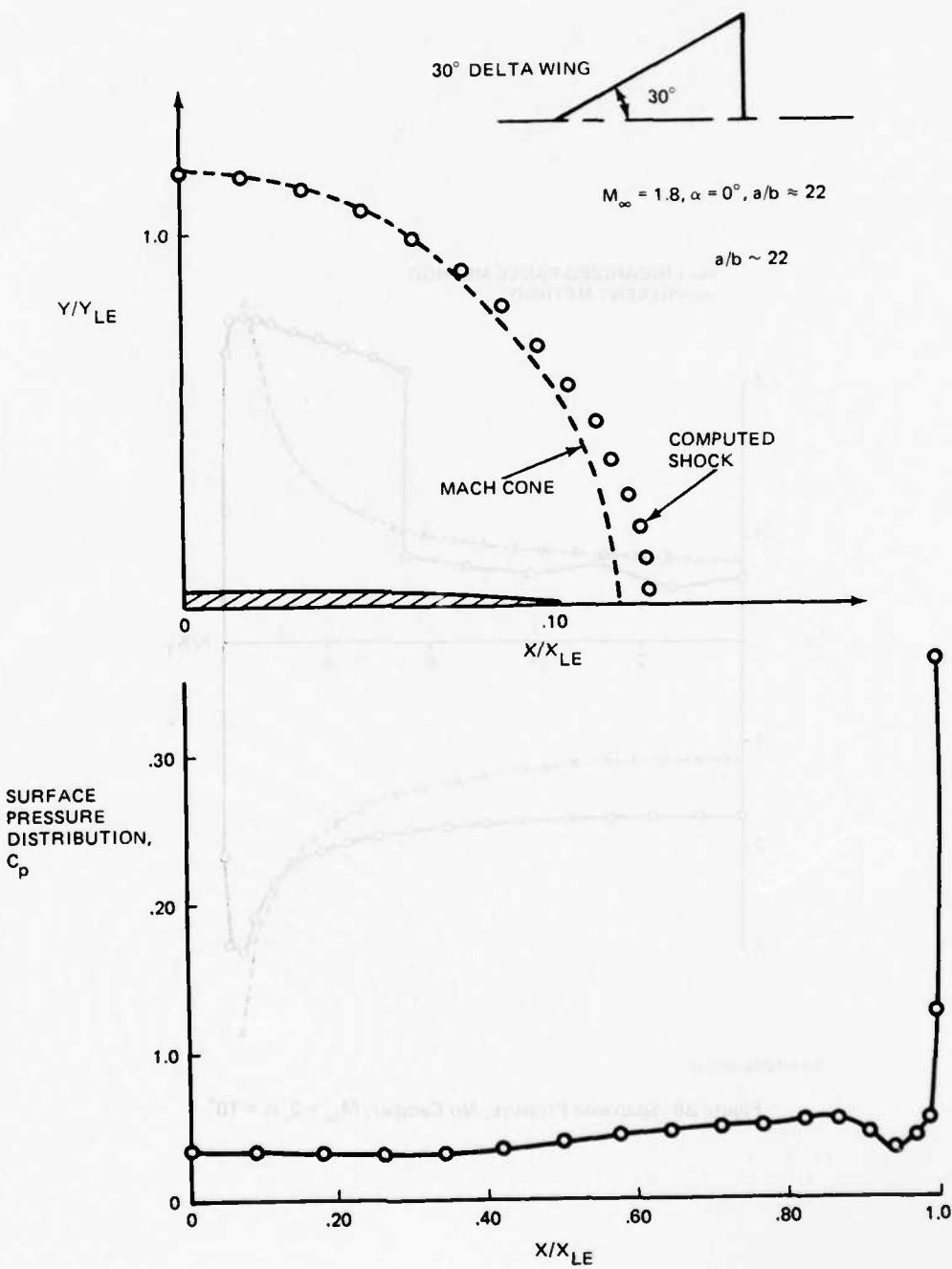
Figure 39 Converged Shock Shape

SURFACE
PRESSURE
DISTRIBUTION,
$C_{P_{BODY}}$

R80-1248-033W
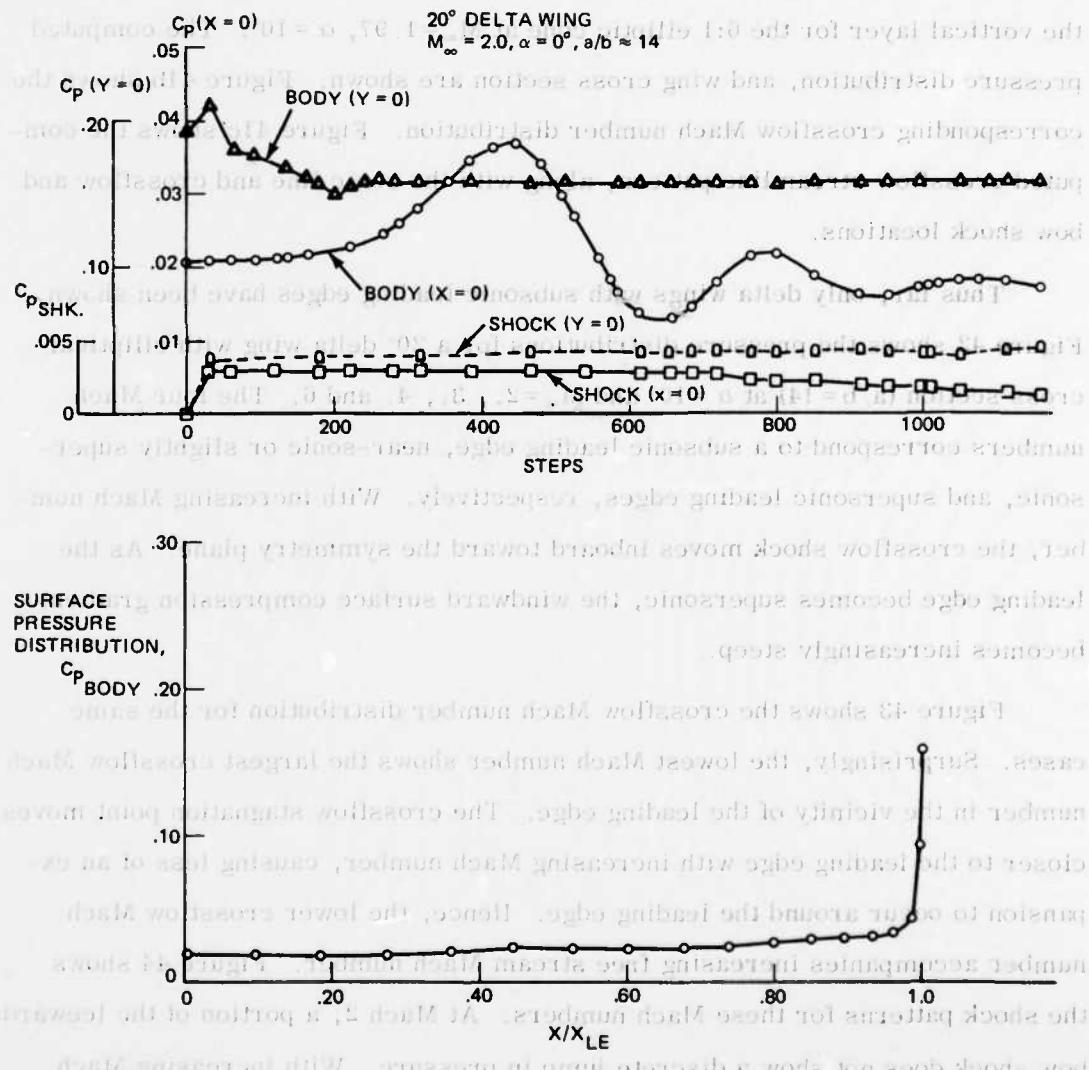
Figure 40 Convergence History of Bow Shock and Body Pressures

73

Using a linearized starting solution therefore seems plausible, and shows promise for the computation of flow about wings. The next step is to generate solutions at angle of attack using a similar linearized starting solution.

Figure 41a shows a previous case recomputed using a modified linearized potential flow starting solution and previously outlined techniques to resolve the vortical layer for the 6:1 elliptic cone at $M_\infty = 1.97$, $\alpha = 10°$. The computed pressure distribution, and wing cross section are shown. Figure 41b shows the corresponding crossflow Mach number distribution. Figure 41c shows the computed crossflow streamline pattern, along with the sonic line and crossflow and bow shock locations.

Thus far, only delta wings with subsonic leading edges have been shown. Figure 42 shows the pressure distributions for a 20° delta wing with elliptical cross section (a/b = 14) at $\alpha = 10°$ and $M_\infty = 2., 3., 4.$ and 6. The four Mach numbers correspond to a subsonic leading edge, near-sonic or slightly supersonic, and supersonic leading edges, respectively. With increasing Mach number, the crossflow shock moves inboard toward the symmetry plane. As the leading edge becomes supersonic, the windward surface compression gradient becomes increasingly steep..

Figure 43 shows the crossflow Mach number distribution for the same cases. Surprisingly, the lowest Mach number shows the largest crossflow Mach number in the vicinity of the leading edge. The crossflow stagnation point moves closer to the leading edge with increasing Mach number, causing less of an expansion to occur around the leading edge. Hence, the lower crossflow Mach number accompanies increasing free stream Mach number. Figure 44 shows the shock patterns for these Mach numbers. At Mach 2, a portion of the leeward bow shock does not show a discrete jump in pressure. With increasing Mach number, the bow shock differs significantly from the Mach wave, especially in the vicinity of the leading edge.

The Mach 2 solution was generated using a linearized potential flow starting solution and the rotated Mach wave as an initial guess for the bow shock shape. The Mach 3 solution was generated using the Mach 2 Euler solution as

74
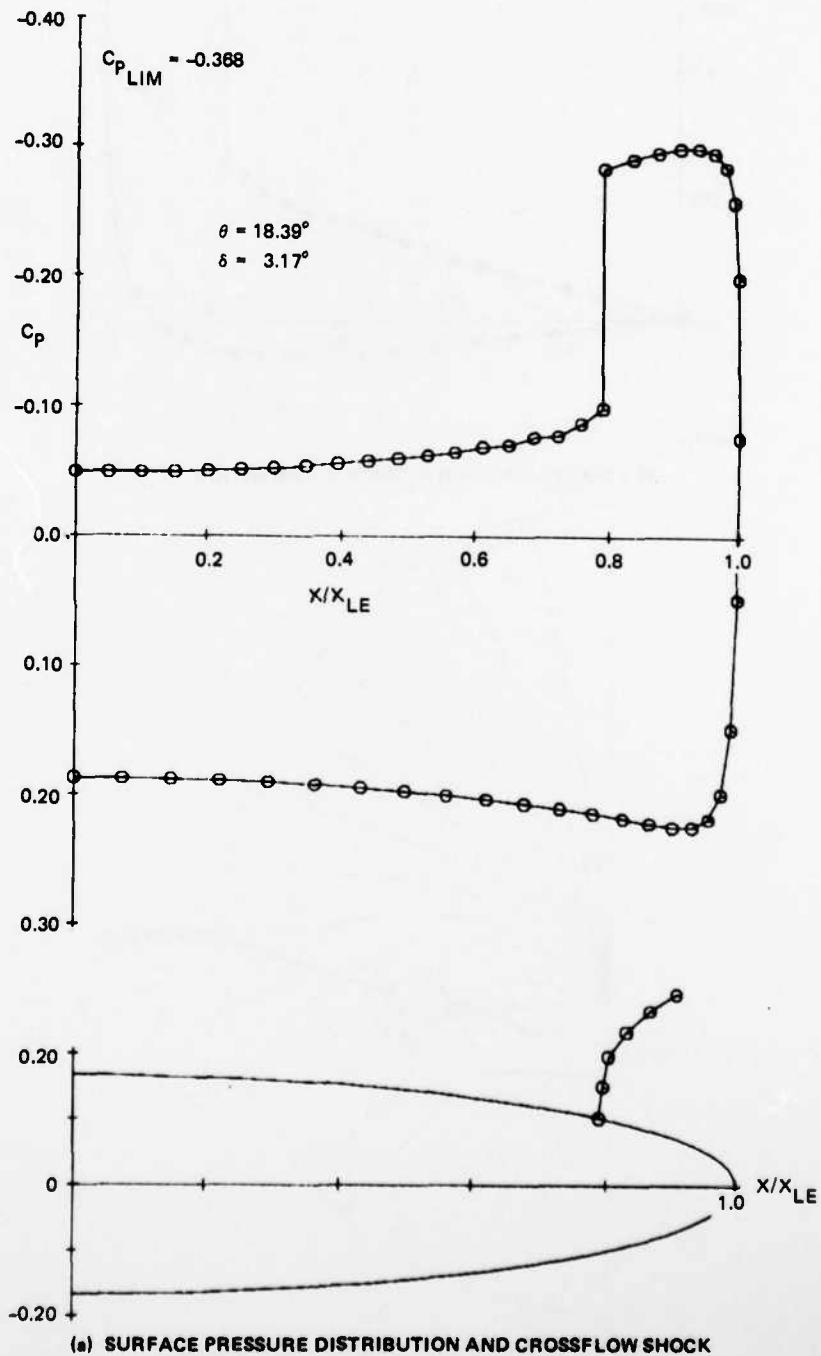
(a) SURFACE PRESSURE DISTRIBUTION AND CROSSFLOW SHOCK

R80-1248-034W

Figure 41 Improved Solution for 6:1 Elliptic Cone, M = 1.97, a = 10°

75
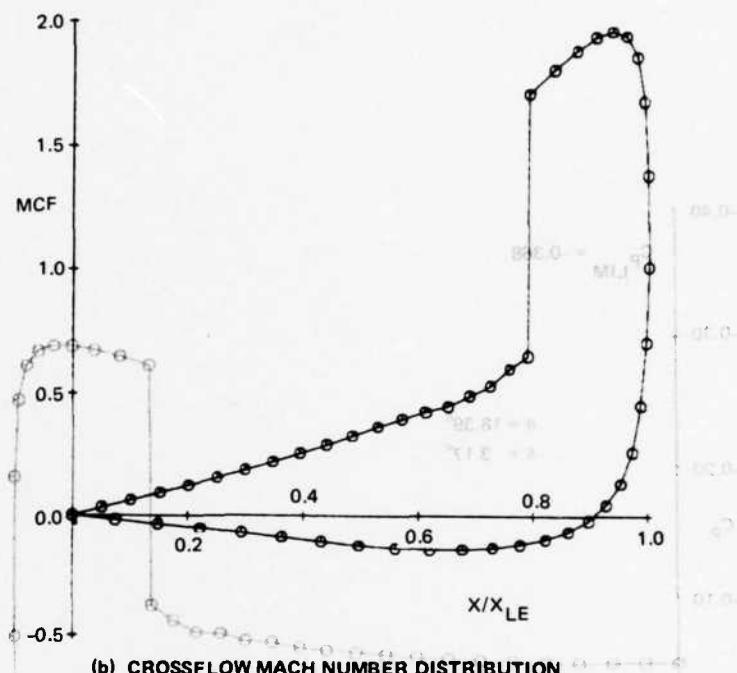
(b) CROSSFLOW MACH NUMBER DISTRIBUTION
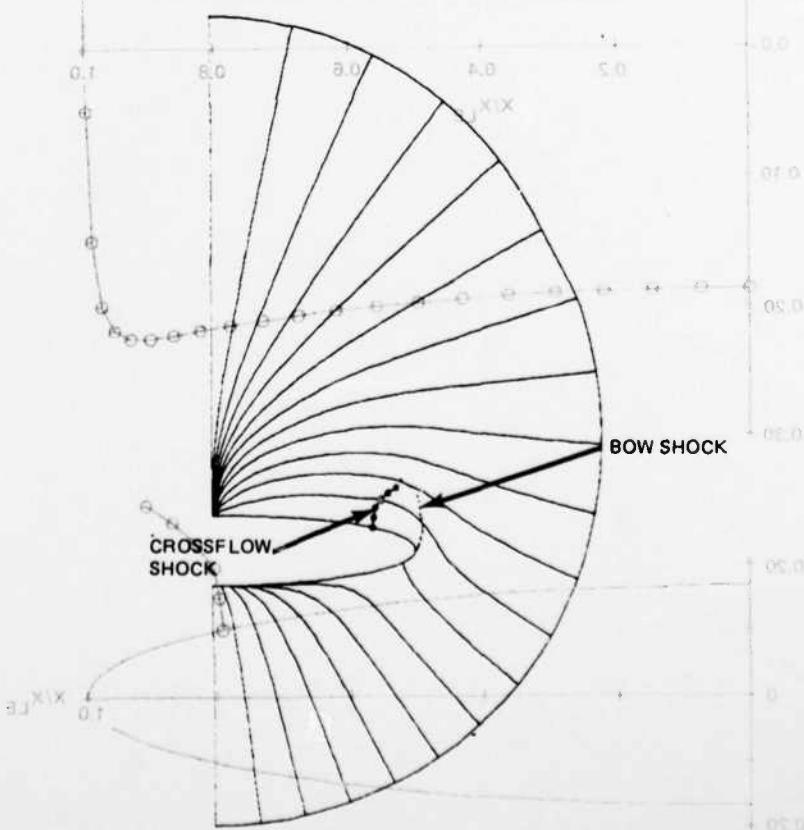
(c) COMPUTED CROSSFLOW STREAMLINE PATTERN

R80-1248-035W

Figure 41 Concluded

76
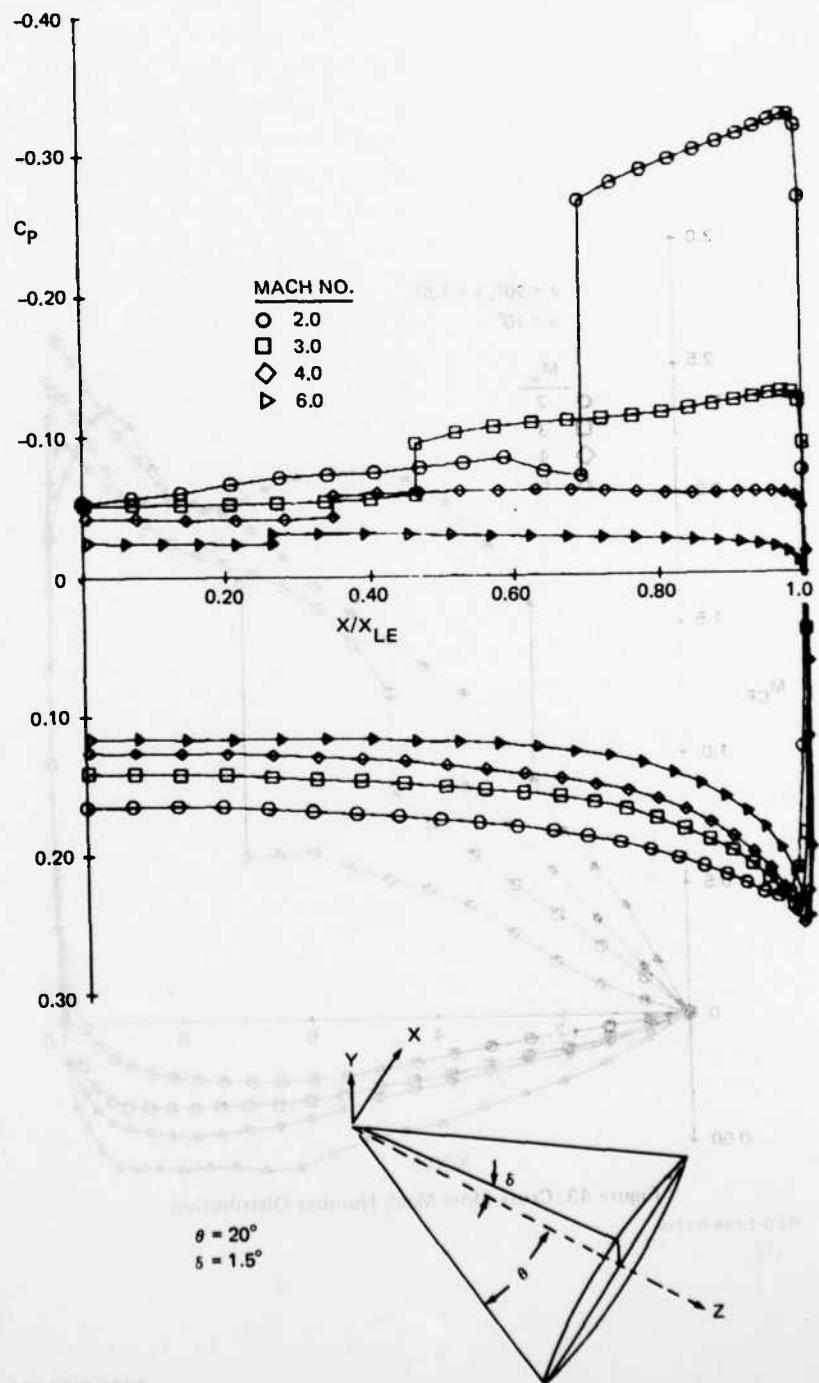
R80-1248-036W

Figure 42 Conical Pressure Distribution for 20° Delta Wing,
a/b = 14, α = 10°

77
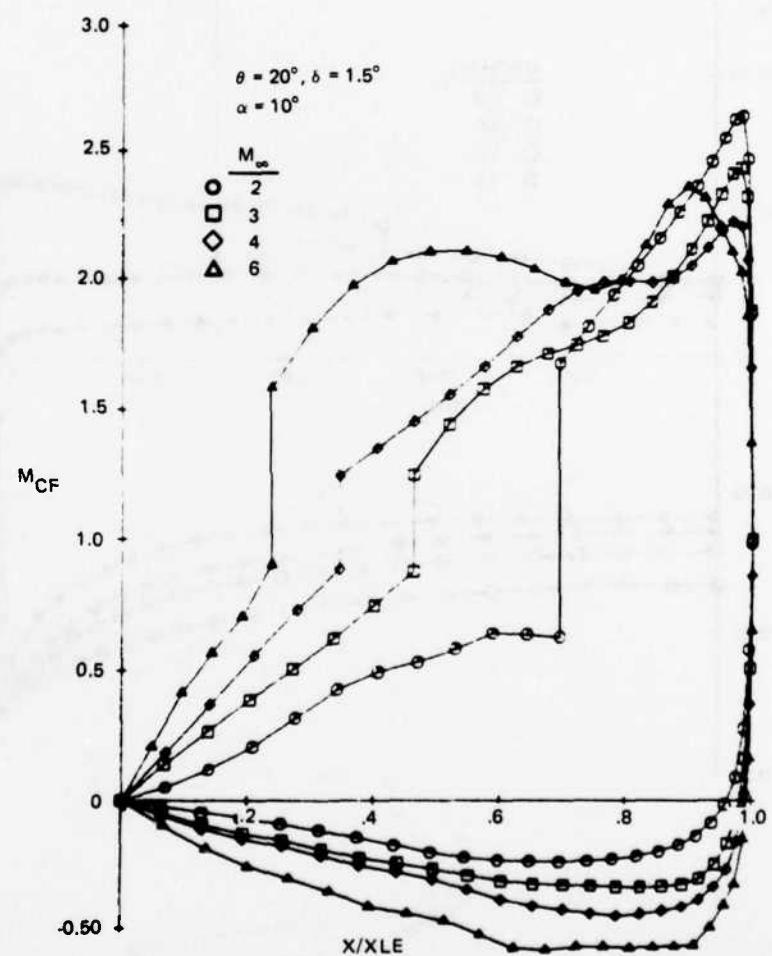
Figure 43 Cross Flow Mach Number Distribution

R80-1248-037W

78
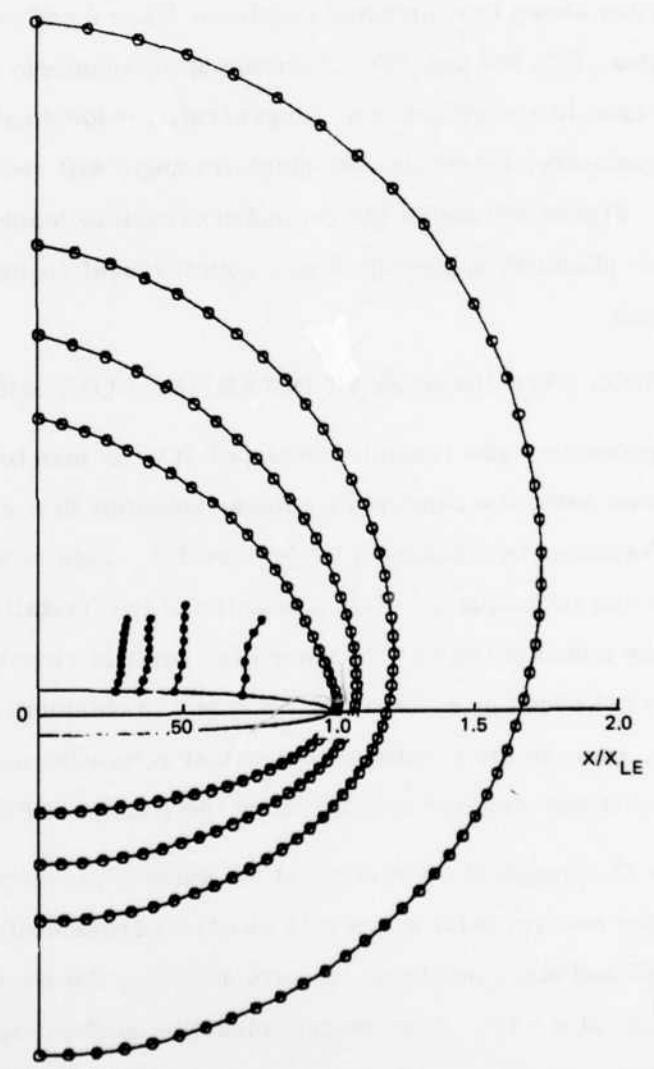
R80-1248-038W
Figure 44 Bow and Crossflow Shock Shapes

79

an initial guess for the flow directions and the bow and crossflow shock shapes. The entire flowfield was scaled to the Mach 3 enthalpy. The other solutions were started in a similar fashion, using the Mach 3 flowfield. Figure 45 shows the crossflow streamline patterns for these Mach numbers. Clearly, the flow angularity around the leading edge in the crossflow plane is greatest for the Mach 2 solution.

Figure 46a shows the computed results at Mach 2 and $\alpha = 5°$ for three planform angles, 15°, 20° and, 30°. Increasing the planform angle reduces the shock in this case to a compression. In general, for identical flow conditions and similar geometry, increasing the planform angle will reduce the strength of the shock. Figure 46b shows the computed crossflow Mach number distributions. The 30° planform angle indicates a supercritical region without a distinct crossflow shock.

4. COMPARISON WITH NONLINEAR POTENTIAL FLOW SOLUTIONS

A new procedure was recently developed at Grumman to compute conical supersonic flows using the complete nonlinear potential flow equation. The method was developed by Grossman (Reference 17). This procedure uses a conical relaxation technique to obtain a solution of the irrotational Euler equations. With the assumptions of irrotationality, vortical singularities and crossflow layers do not occur or present any problems in obtaining converged solutions. Hence, some of the results of the conical relaxation method were compared to the solutions obtained by integrating the rotational Euler equations.

Figures 47 through 51 show some of the surface pressure distribution comparisons for several delta wings with elliptical cross sections at various angles of attack and Mach numbers. Figure 47 shows the results for a Mach 1.97, 6:1 ellipse at $\alpha = 10°$. The conical relaxation method captures the shocks and the crossflow shock is usually smeared over two or three grid points. The comparison is quite good for both the location and pressure jump across the shock. The conical relaxation method predicts somewhat lower pressures on the expansion side of the leading edge as compared to the Euler solution. These

$\alpha = 10°$
$\theta = 20°$
$\delta = 1.5°$

(a) $M_\infty = 2.0$ (b) $M_\infty = 3.0$

VORTICAL "LIFT-OFF"
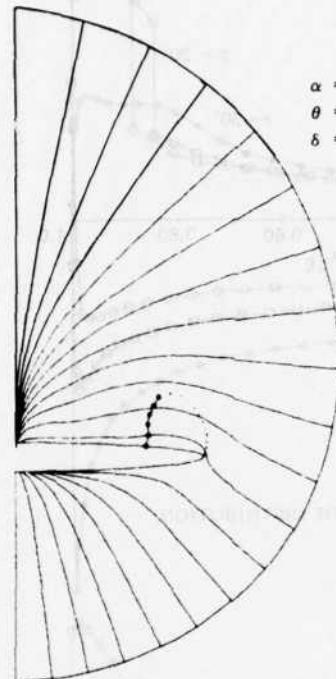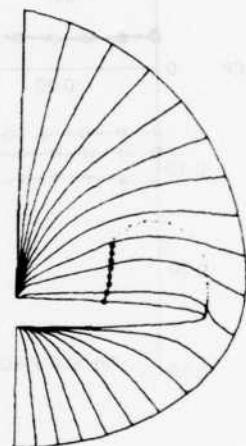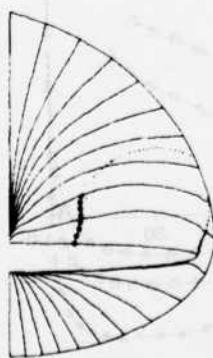
(c) $M_\infty = 4.0$ (d) $M_\infty = 6.0$

R80-1248-039W

Figure 45 Crossflow Streamline Patterns for M_∞ = 2.0, 3.0, 4.0 and 6.0

81

(a) SURFACE PRESSURE DISTRIBUTION

(b) CROSSFLOW MACH NUMBER DISTRIBUTION
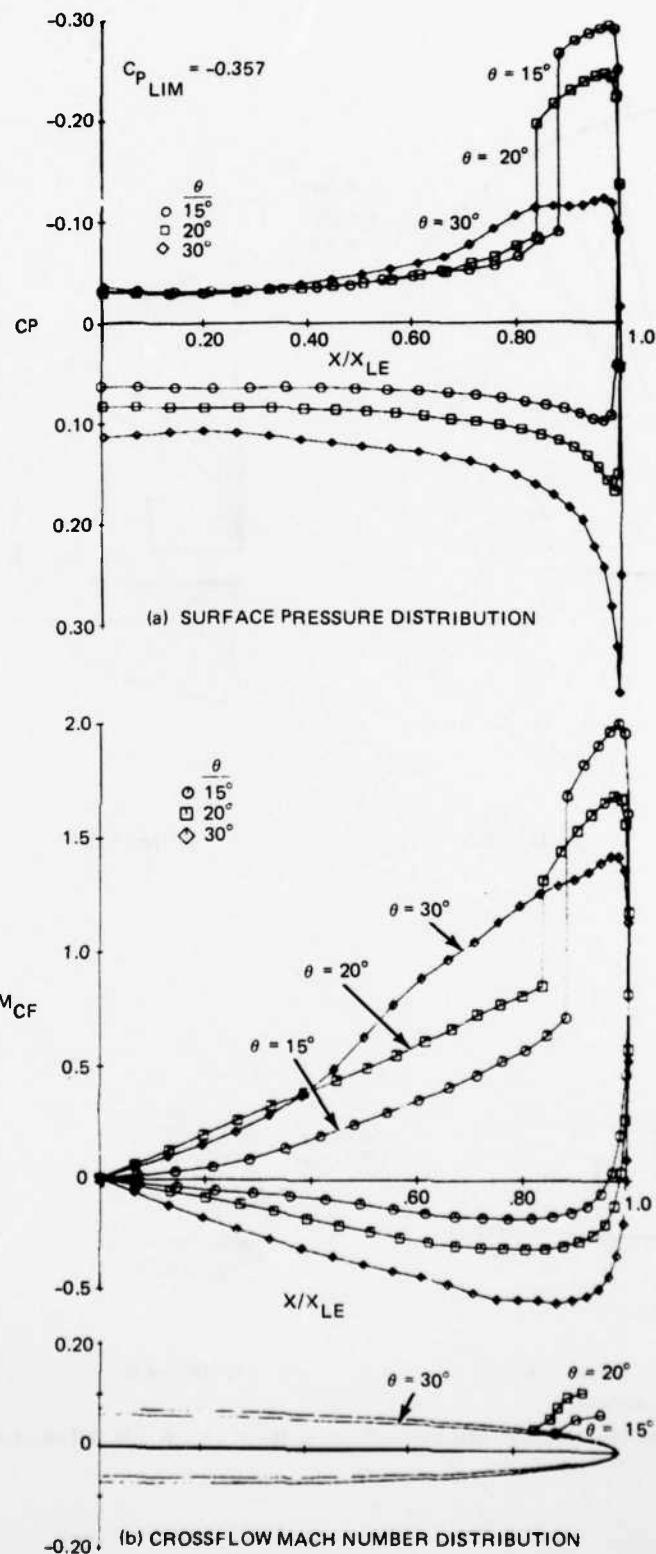
R80-1248-040W

Figure 46 Computed Results for Three Planform Angles at $M_\infty = 2.0$, $\alpha = 5°$

82
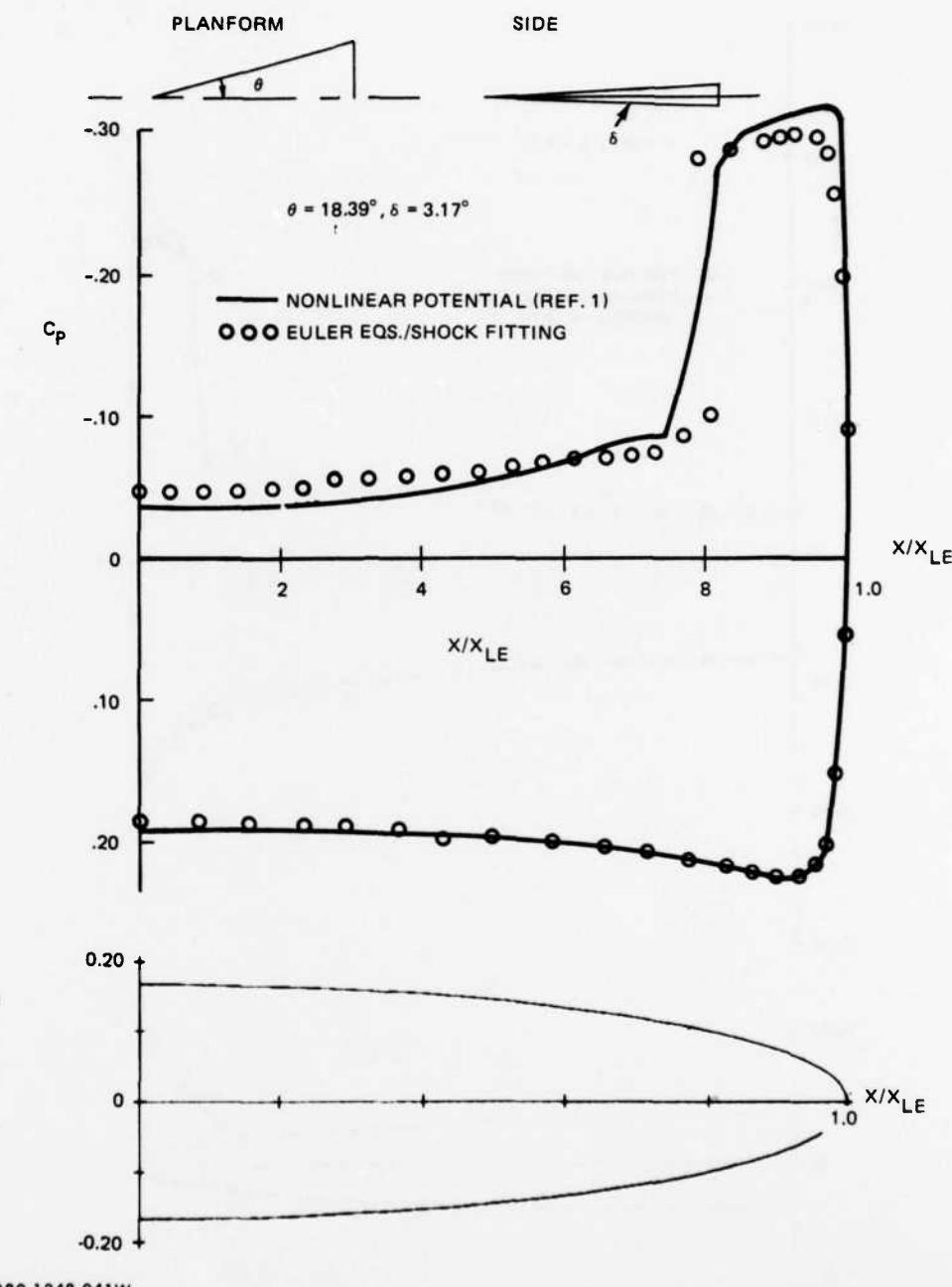
Figure 47 Comparison of Nonlinear Theories for 6:1 Ellipse, $M_\infty = 1.97$, $\alpha = 10°$

R80-1248-041W

83
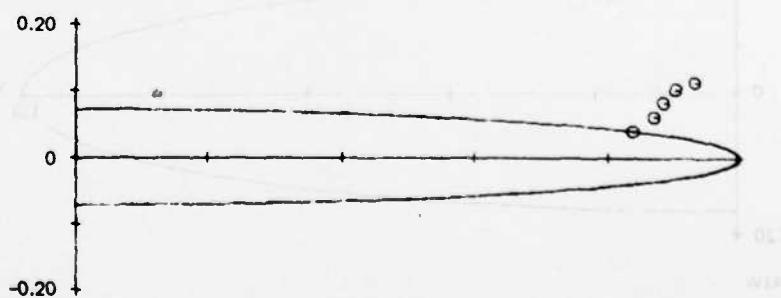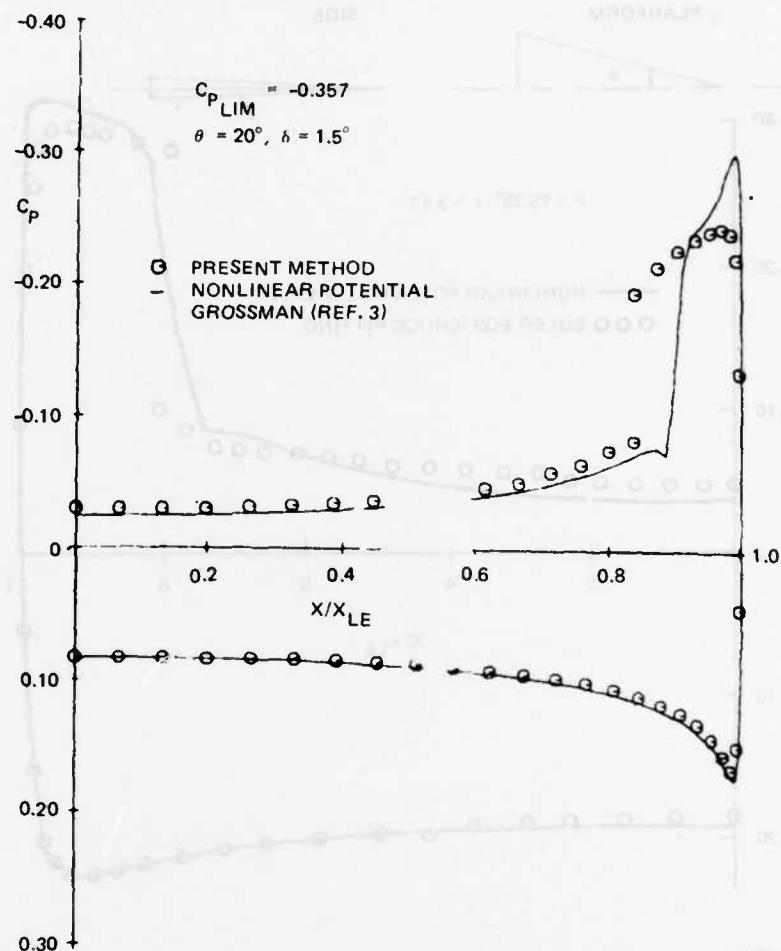
Figure 48 Comparison of Nonlinear Theories for 14:1 Ellipse, $M_\infty = 2.0$, $\alpha = 5°$

R80-1248-042W

84
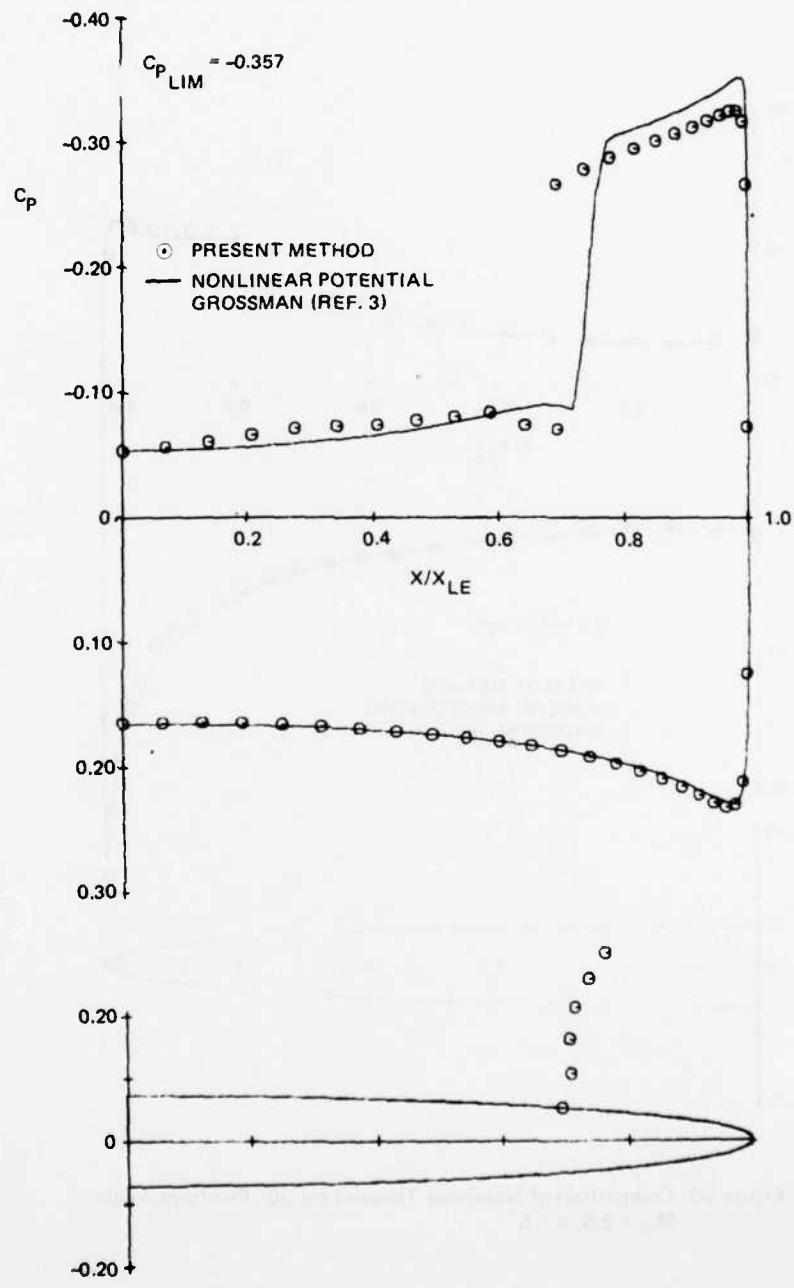
Figure 49 Comparison of Nonlinear Theories for 14:1 Ellipse, $M_\infty = 2.0$, $\alpha = 10°$

R80-1248-043W

85
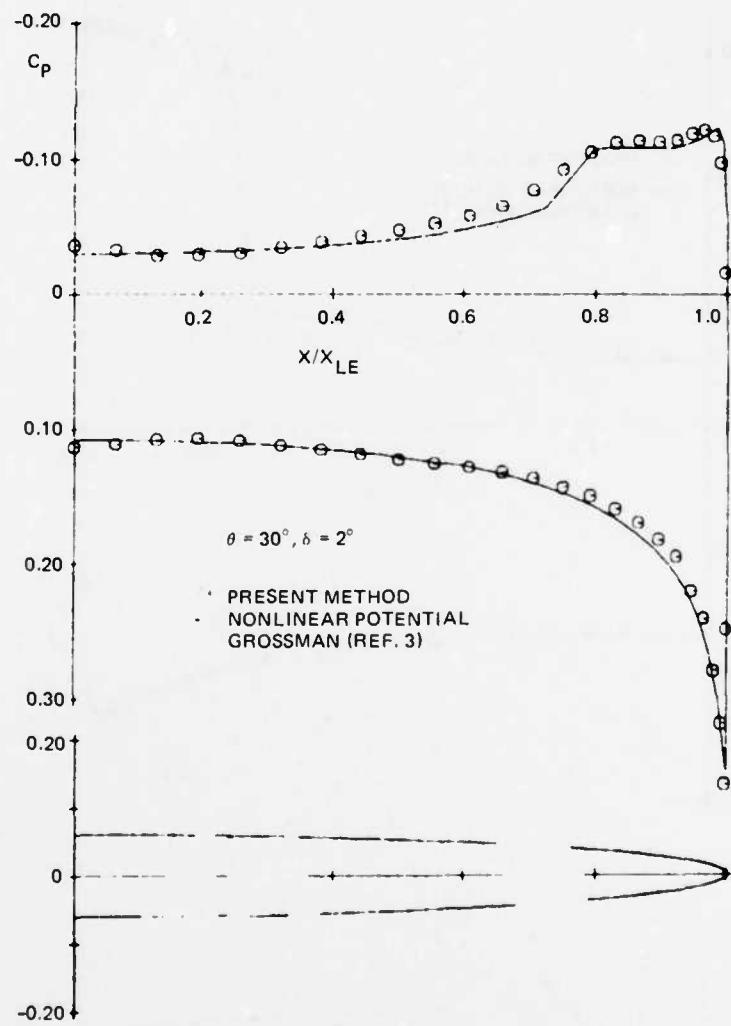
Figure 50 Comparison of Nonlinear Theories for 30° Planform Angle, $M_\infty = 2.0$, $a = 5°$

R80-1248-044W

86

UNCLAS

OF

34
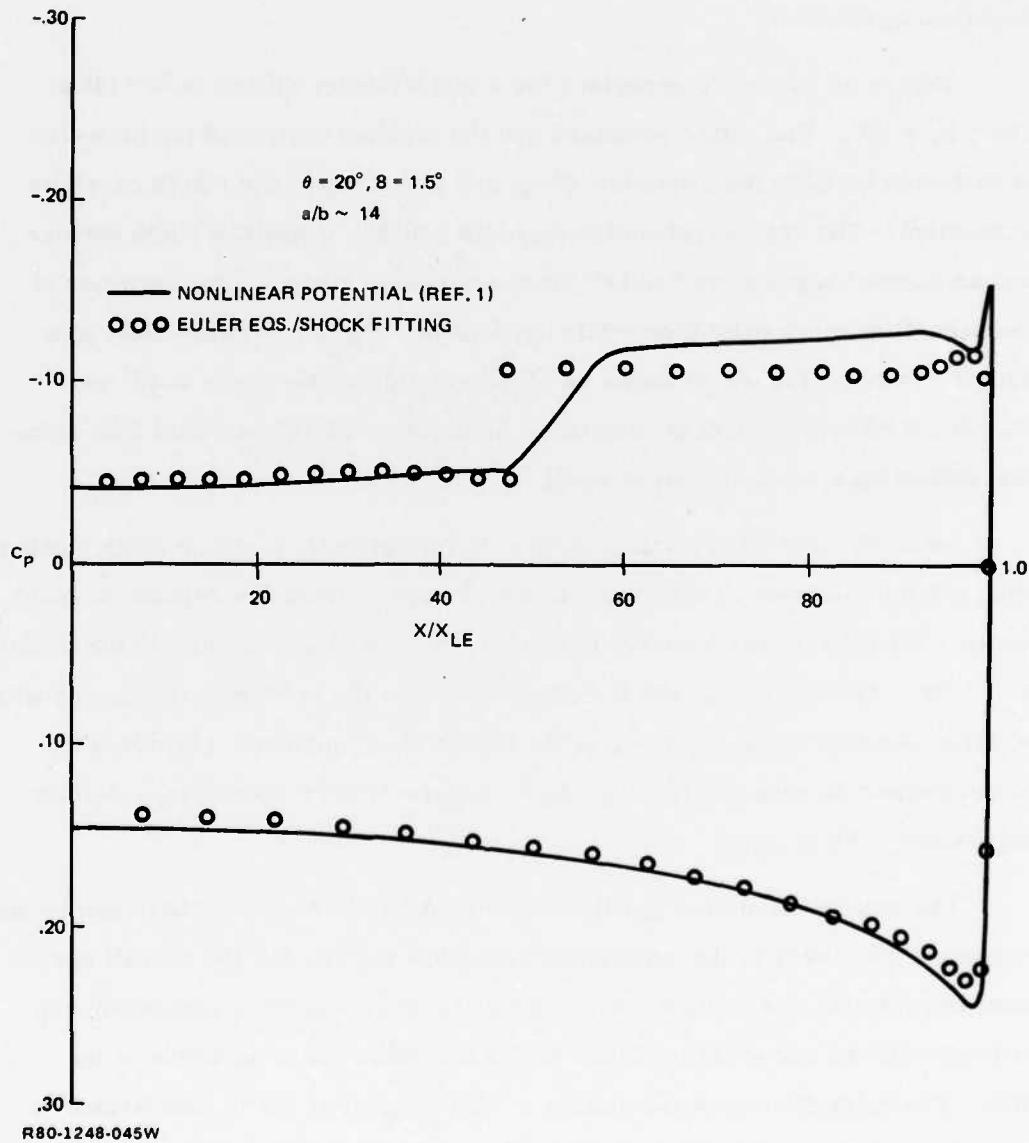
Figure 51 Comparison of Nonlinear Theories for 14:1 Ellipse, $M_\infty = 3.0$, $\alpha = 10°$

R80-1248-045W

87

lower pressures result in somewhat higher crossflow Mach numbers in the vicinity of the leading edge. A slight discrepancy in the leeward symmetry plane pressure is also apparent, while the windward pressure distribution is in excellent agreement.

Figure 48 shows a comparison for a much thinner ellipse ($a/b \sim 14$) at Mach 2, $\alpha = 5°$. The entire windward and the leeward portion of the pressure distribution between the crossflow shock and symmetry plane are in excellent agreement. The conical relaxation predicts a higher crossflow Mach number and an expansion pressure "spike" around the leading edge. The locations of the crossflow shock exhibit only fair agreement. Figure 49 shows the same wing at $\alpha = 10°$. Figure 50 shows an ellipse at a planform angle of $30°$ and $M_\infty = 20$, $\alpha = 5°$. Excellent agreement is achieved, with the potential flow solution indicating a weak crossflow shock.

Since the conical relaxation method is irrotational, a higher Mach number comparison was made to determine if any entropy-related discrepancies would occur. Figure 51 shows the comparison for the delta wing of Figure 49 but at Mach 3, $\alpha = 10°$. The figure exhibits the same trends as the previous comparison with no large discrepancies occurring at the higher Mach number. Figures 47 to 50 correspond to subsonic leading edges, Figure 51 corresponds to a slightly supersonic leading edge.

The relaxation method predicts somewhat higher Mach numbers and lower expansion pressures in the supersonic crossflow region, but the overall agreement in pressure is excellent. The conical relaxation method adequately captures the shocks and exhibits all the major nonlinear characteristics of the flow. The relaxation method requires a finer mesh (60×60) in comparison to the Euler solutions (50×35), but does not require shock fitting.

5. OTHER CONICAL SHAPES

a. Cones at High Incidence

Some examples of the flow generated by circular cones at high incidence were computed to determine if significant lift-off of the vortical singularity

could be achieved at low supersonic Mach numbers. Figure 52 shows the cross-flow streamline pattern computed for a 5° cone semi-apex angle at $M_\infty = 2.0$, $\alpha = 10°$. The streamlines clearly depict the lift-off of the vortical singularity. The circular cone streamline pattern is distinct from the elliptic cone in that only one nodal singularity occurs in the leeward symmetry plane. The stagnation streamline wetting the body lies in the windward symmetry plane. Hence, the body windward symmetry plane point is the saddle point. Numerical difficulties were not encountered in computing this case because of the small cone angle. A supersonic crossflow region does not occur and thus the absence of a crossflow shock. The bow shock is weak and thus the flow is not far from irrotational. Figure 53 shows the result for a 12.5° cone at $M_\infty = 1.8$, $\alpha = 25°$. This cone was computed in an attempt to achieve vortical lift-off with a cross-flow shock at a lower Mach number. The streamlines exhibit the normal coalescent behavior at the leeward vortical singularity that is typical of incipient lift-off. Lift-off was not achieved at the angle of attack corresponding to twice the cone angle. The crossflow shock exhibits large curvature in its radial shape. This may be an extreme case of the vortical and crossflow layer problems mentioned earlier. For circular cones, the radial density of streamlines is greater in the vicinity of the surface, thus indicating larger gradients in entropy and other flow variables. It was necessary to use 40 radial grid points to have enough resolution to fit the crossflow shock.

b. Wing-Body Effect

To determine the interference effect of a conical body on the wing flowfield, two conical wing-body geometries were computed. Both bodies were cubically faired to the wing at a specified conical location (see Figure 54). Both wing-body geometries were computed using a converged Euler solution for the wing as the initial starting solution. The geometry was then deformed continuously until the specified conical wing-body geometry was achieved, at which point in the marching technique, the wing-body geometry was held invariant and conical until convergence was achieved. Figures 55 through 57 show the results for a very

89

VORTICAL
"LIFT OFF"
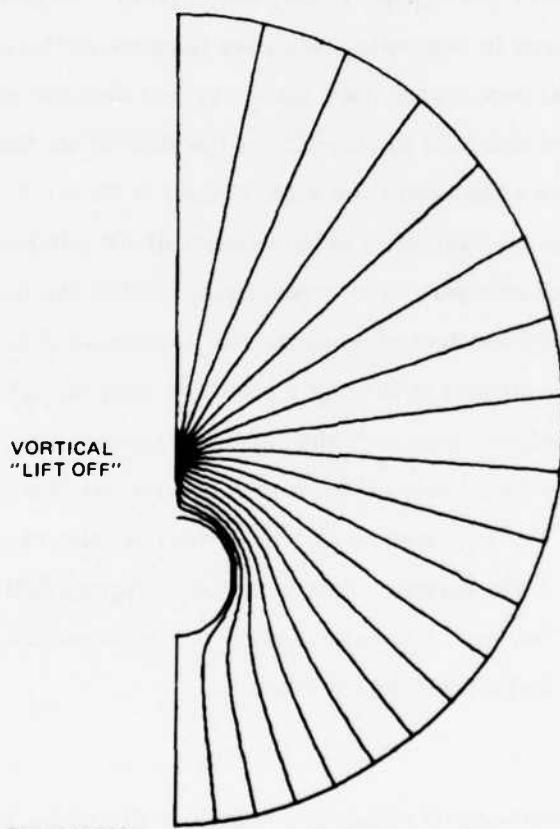
R80-1248-046W

Figure 52 Crossflow Streamline Pattern for 5° Semi-apex Angle
Cone at M_∞ = 2.0, α = 10°
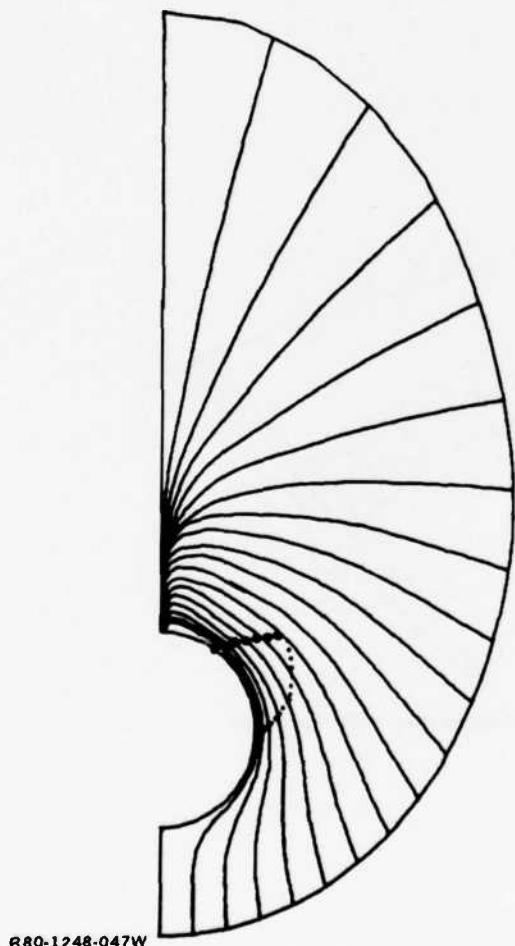
Figure 53   Crossflow Streamline Pattern for 12.5° Semi-apex
Angle Cone M_∞ = 1.8, α = 25°
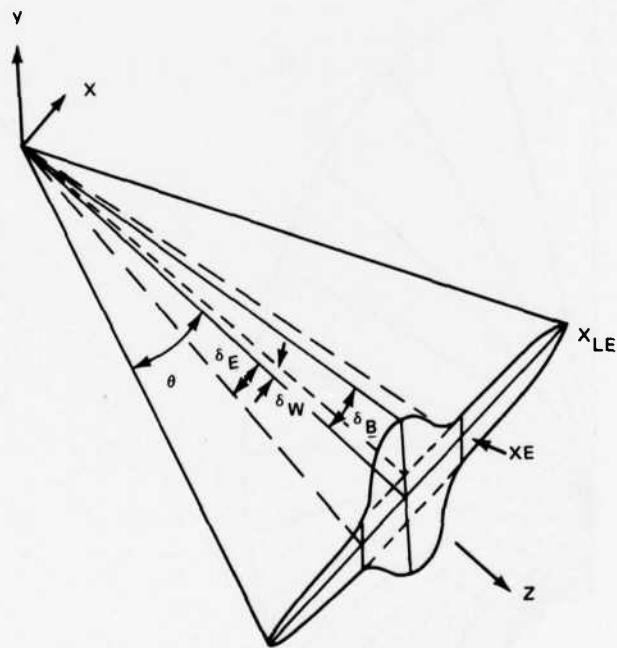
R80-1248-048W

Figure 54 Conical Wing-Body Geometry

92
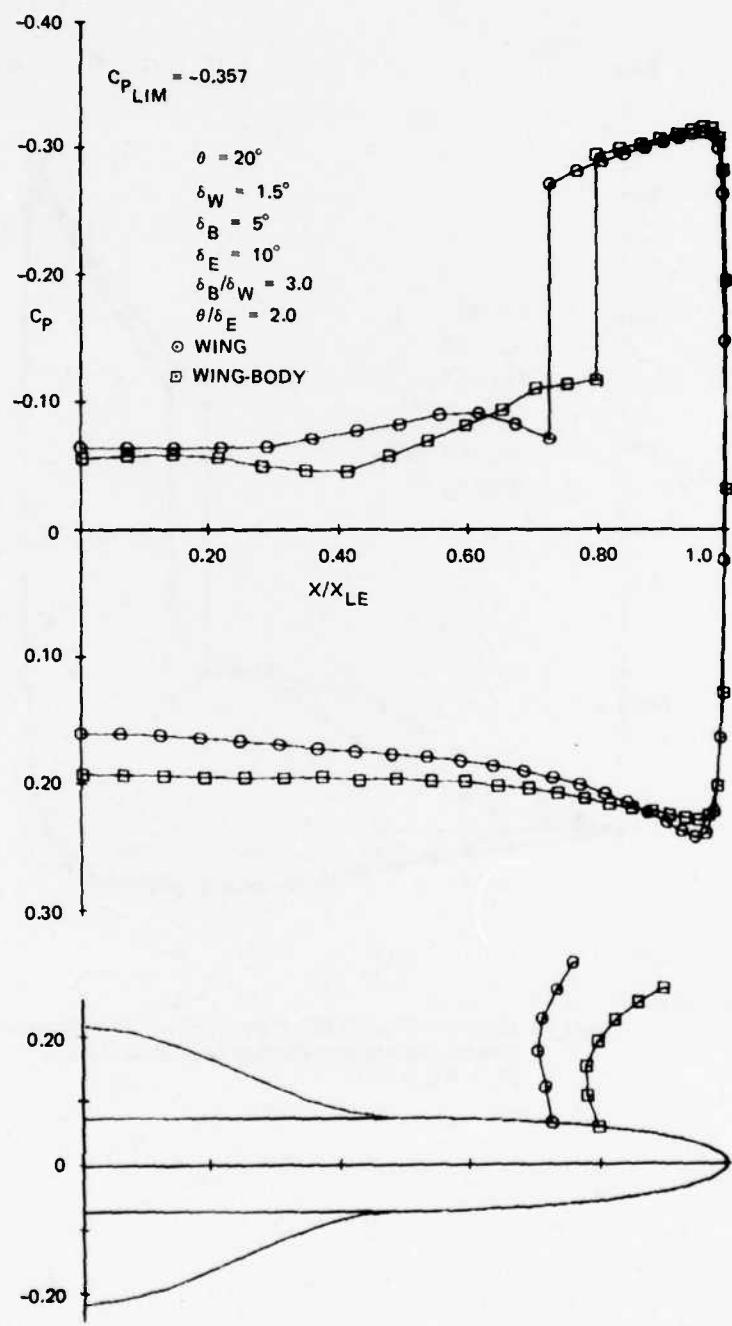
Figure 55 Body Interference Effect on Surface Pressure and Crossflow
Shock for Well-Blended Conical Geometry, M_∞ = 2.0, α = 10°

R80-1248-049W

93
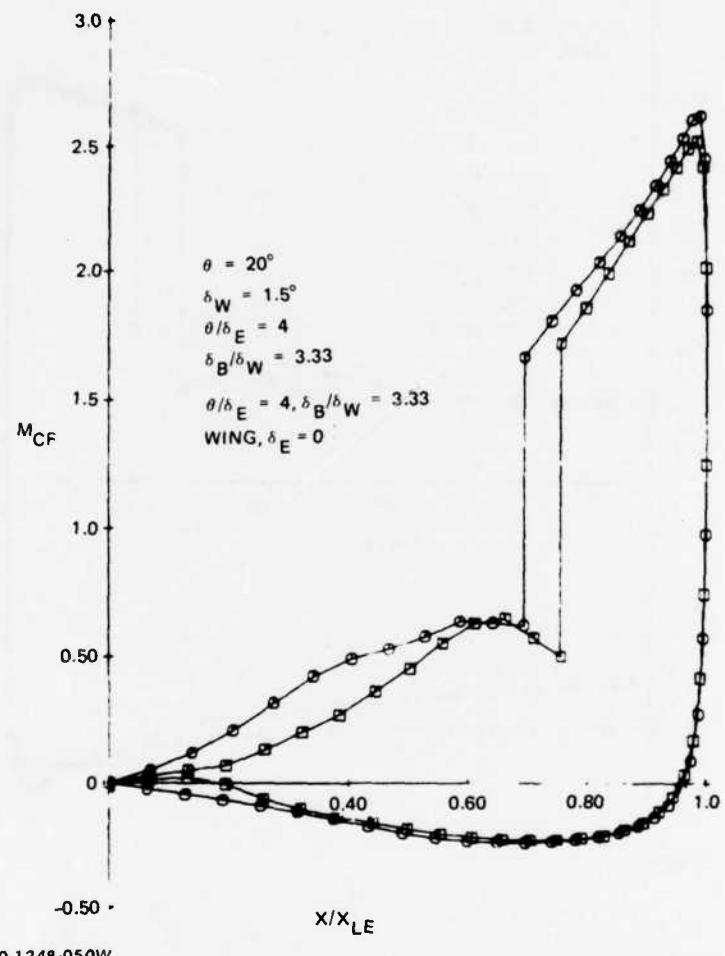
Figure 56 Body Interference Effect on Crossflow Mach Number
Distribution for Well-Blended Conical Geometry,
$M_\infty = 2.0, \alpha = 10°$

R80-1248-050W

94
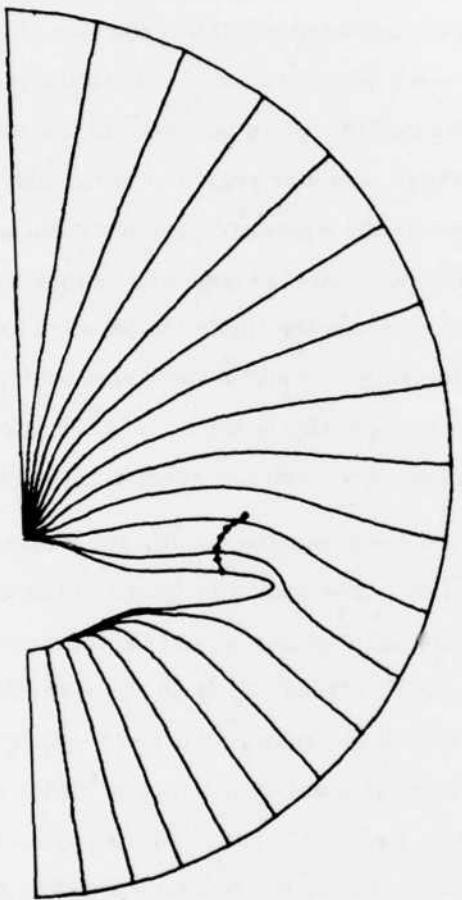
$\theta \approx 20°$
$\delta_W = 1.5°$
$\delta_E = 10°$
$\delta_B/\delta_W = 3.0$
$\theta/\delta_E = 2.0$

R80-1248-051W

Figure 57   Body Interference Effect on Wing-Body Crossflow
Streamline Pattern for Well-Blended Conical
Geometry, $M_\infty = 2.0$, $\alpha = 10°$

95

blended wing-body cross section where the body was faired to the wing at a position (denoted by δ_E) midway between the wing leading edge and the symmetry plane. The body symmetry plane angle was $4.5°$ (δ_B) and the extended center-line angle of the wing was $1.5°$ (δ_W). Figure 55 shows the resulting pressure distribution and crossflow shock shape in comparison with the converged wing solution that was used to start the calculation. The presence of the faired body pushes the location of the crossflow shock outboard toward the leading edge. The crossflow shock thus reacts earlier to the presence of the low values of crossflow that occur in the leeward shoulder region or wing-body juncture. The presence of the body increases the windward pressures but also somewhat increases the leeward pressures between the shock and symmetry plane. The outboard movement of the shock reduces the lift in the leeward expansion re-gion. The crossflow streamline pattern changes somewhat in that the leeward streamlines appear to coalesce tangentially to the body at the vortical singular-ity, whereas the wing alone appeared to coalesce normal to the body.

Figures 58 through 60 show the computed results for a more abrupt (not so blended) wing-body combination. The body was faired to the wing at a 5° angle (δ_E), with a body centerline angle of 5° (δ_B) and the wing thickness angle remaining at $1.5°$. The same general trends apply to these results except for one interesting aspect. The crossflow streamline pattern (Figure 60) shows that the windward nodal or vortical singularity has moved off the symmetry plane and occurs at the wing body juncture. The windward symmetry plane must remain a crossflow stagnation point, but becomes a saddle point instead of a nodal singularity. The crossflow Mach number distribution confirms the streamline pattern in that four instead of three crossflow stagnation points occur for this geometry. The leeward vortical singularity remains intact, and once again the streamlines appear to converge tangentially. The leeward streamlines thus locally behave in a similar fashion to the leeward streamlines on a circular cone at moderate incidence. Similar behavior of the leeward nodal singularity for conical wing-body configurations has been observed in the non-linear potential flow solutions, using the methods developed in Reference 17.

96

$C_{P_{LIM}} = -0.357$

$\theta = 20°$
$\delta_W = 1.5°$
$\delta_B = 5°$
$\delta_E = 10°$
$\theta/\delta_E = 4$
$\delta_B/\delta_W = 3.33$

○ WING,
□ WING-BODY

C_P

X/X_{LE}
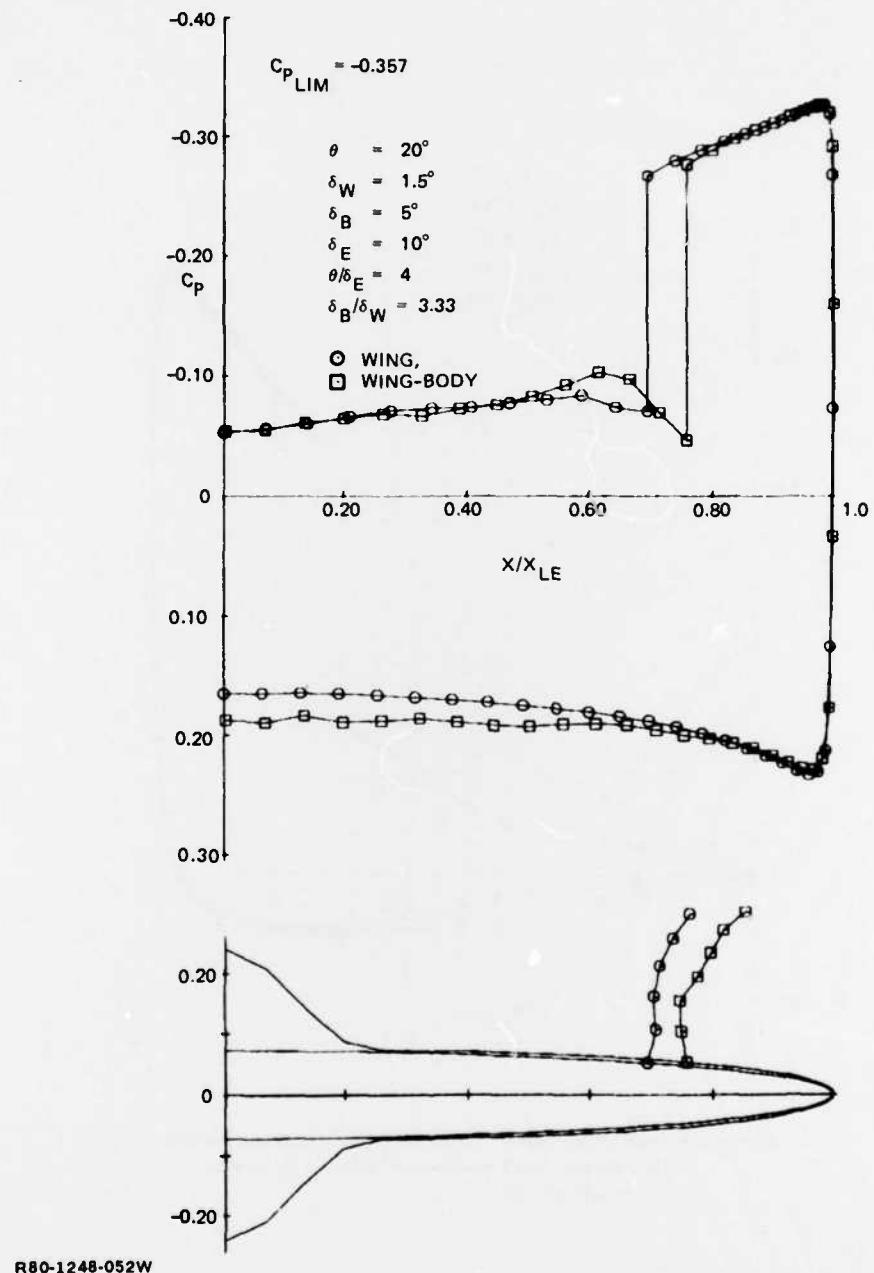
R80-1248-052W

Figure 58 Body Interference Effect on Surface Pressure and
Crossflow Shock for Less-Blended Conical Geometry,
$M_\infty = 2.0, \alpha = 10°$

97
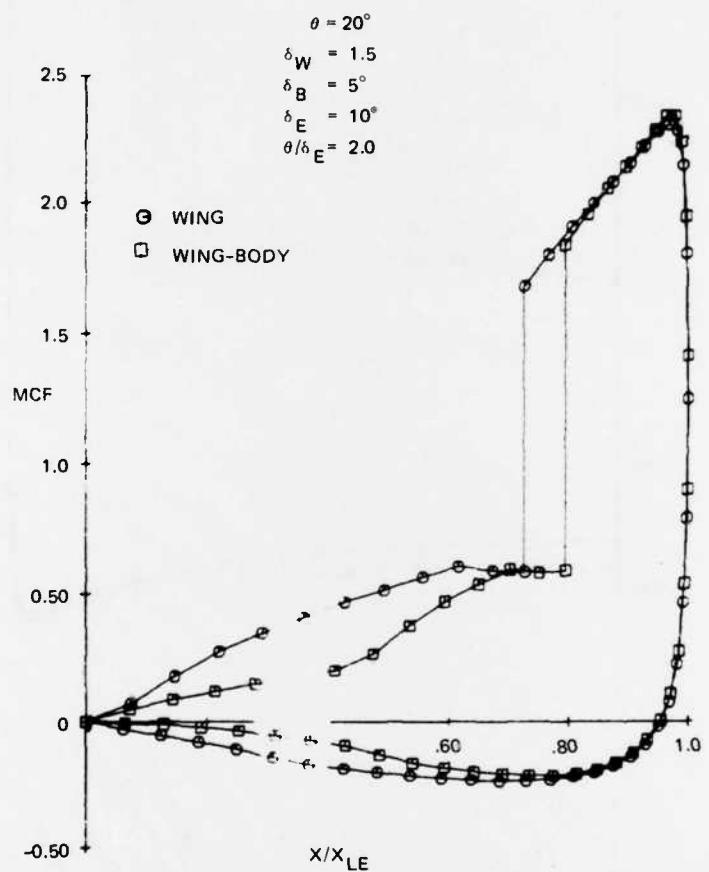
Figure 59 Body Interference Effect on Crossflow Mach Number
Distribution for Less-Blended Conical Geometry,
$M_\infty = 2.0, \alpha = 10°$

R80-1248-053W

98

$\theta = 20°$
$\delta_W = 1.5°$
$\delta_E = 10°$
$\delta_B = 5°$
$\delta_B/\delta_W = 3.33$
$\theta/\delta_E = 4$
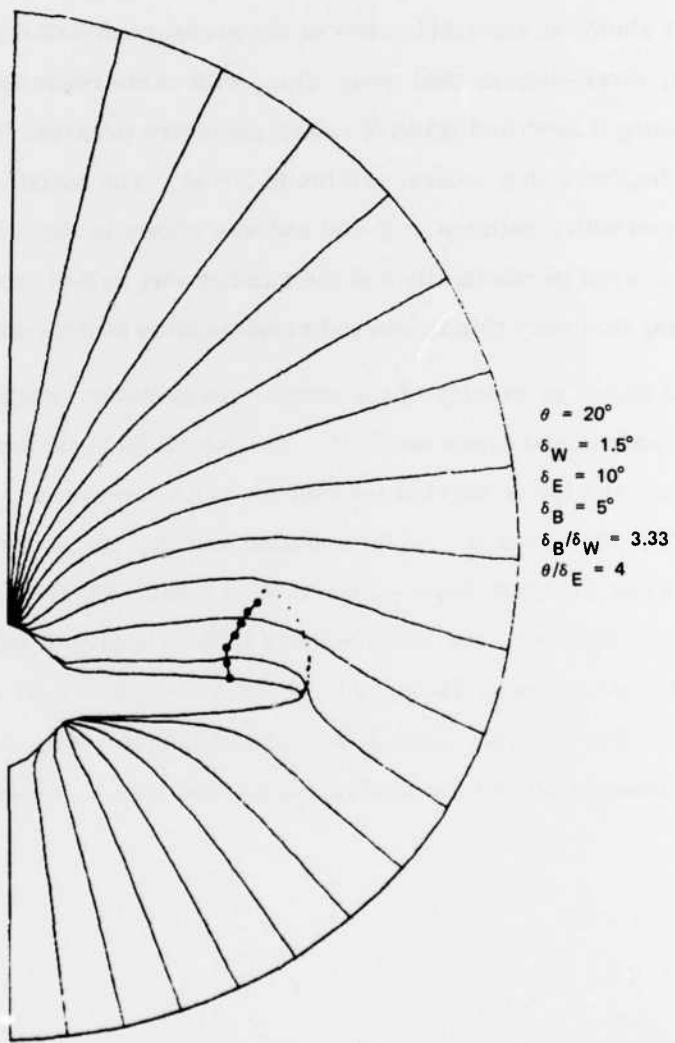
R80-1248-054W

Figure 60   Body Interference Effect on Crossflow Streamline Pattern
for Less-Blended Conical Geometry, $M_\infty = 2.0$, $\alpha = 10°$

99

It must be mentioned that the conformal mapping clusters points around the leading edge of the wing. Hence, minimal resolution was obtained in the wing-body juncture area with 50 circumferential points.

6. THREE-DIMENSIONAL WINGS

Figure 61 shows an isometric view of the pressure distributions computed for a fully three-dimensional wing, along with some representative spanwise sections using a modified NASA/Craidon geometry program (Reference 10). The wing begins with a conical section to $Z = 30$. The starting solution used was the converged Euler solution at $Z = 30$ and was shown in Figure 41. The thickness was tapered parabolically and the camber was varied from $Z = 30$ to $Z = 150$, resulting in a very thin cambered cross section at the trailing edge.

Figure 62 shows an overlay of the same representative nondimensional pressure distributions and cross sections. The longitudinal thickness variation expands the upper and lower surface pressures. The pressures in the vicinity of the leading edge also expand. At the thinnest section, the pressure begins to approach limiting pressure ($Cp = -.367$ at $M_\infty = 1.97$). Figure 63 demonstrates the development of the crossflow Mach number in the vicinity of leading edge for two of the thinner cross sections. At $Z = 144.5$, which is near the trailing edge of the wing, the crossflow approaches a Mach number of 7. Certainly, this extreme expansion around the leading edge would lead to boundary layer separation.
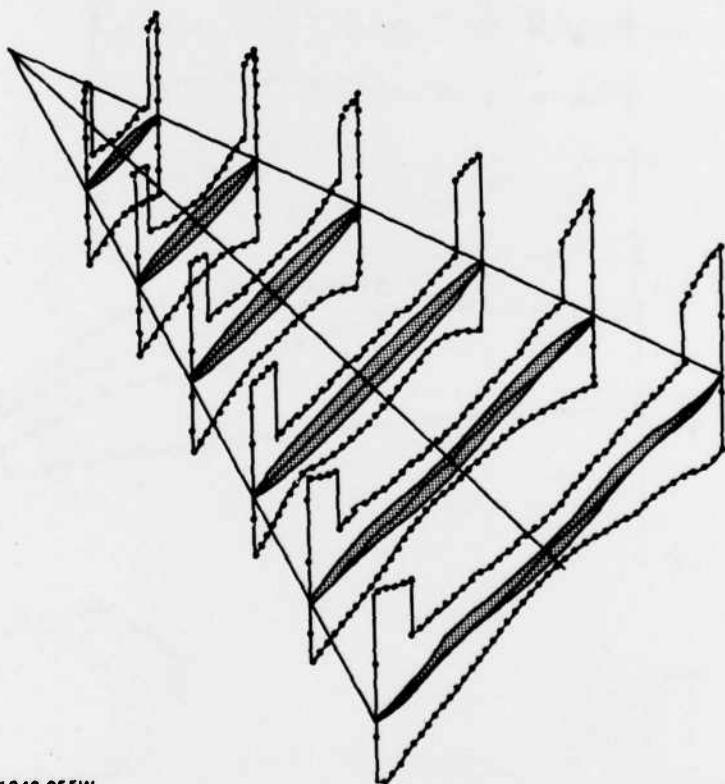
Figure 61 Pressure Distribution Computed for Fully Three-Dimensional
Wing, $M_\infty = 1.97$, $\alpha = 10°$
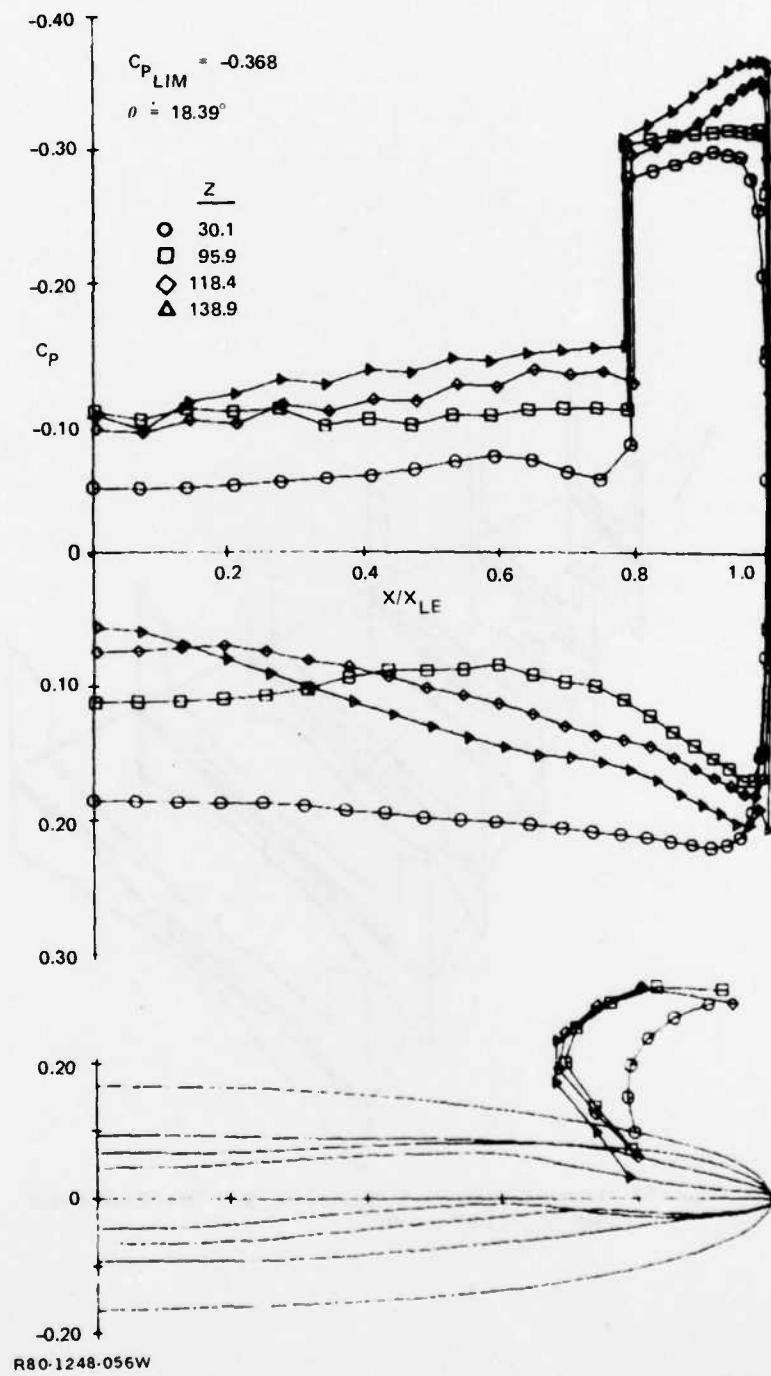
Figure 62 Pressure Distributions and Crossflow Shocks at Various Stations of Fully 3-D Wing, $M_\infty = 1.97$, $\alpha = 10°$

R80-1248-056W

102
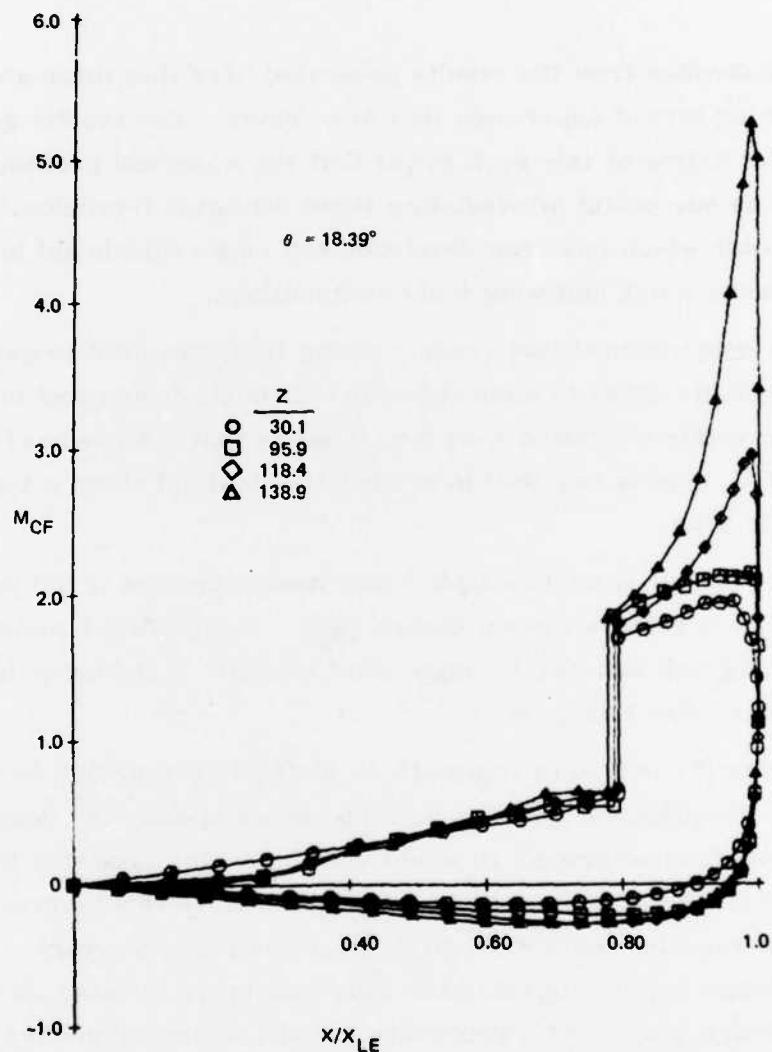
Figure 63   Crossflow Mach Number Distributions at Various Stations
of Fully 3-D Wing, $M_\infty = 1.97$, $\alpha = 10°$

R80-1248-057W

103

SECTION XI

CONCLUSIONS

It is obvious from the results presented here that there are important nonlinear aspects of supersonic flow over wings. The results generated during the course of this work prove that the numerical procedures used here can be successful in predicting these nonlinear flowfields. Therefore the code which has been developed can be a valuable aid in the design of supersonic wings and wing/body combinations.

The computational time (code running time) required to generate these flowfields seems to make the code a difficult design tool to use. From the results generated thus far, it seems that a minimum of about one hour C.P.U. time is required to predict the flowfield about a typical supersonic wing.

This number is unacceptable if the design process is to cycle through many wings to achieve certain design goals. A significant reduction of this running time will require significant changes in the computational technique used in this work.

During the course of this work an alternative approach has been considered. Specifically, the wing designer would specify the design goals and a computational procedure would develop a wing geometry to meet these goals. Computational procedures which solve this inverse problem have been reported quite extensively over the past few years. Most of these schemes involve iterating the wing geometry, for example, to achieve certain design goals. This procedure would necessarily involve a solution to the direct problem which, in this case, would be unacceptable because of the lengthy computational times involved in the direct problem.

For the simplest of the inverse problems (i.e. specify the surface pressure distribution and generate a wing geometry), a scheme has been studied during the course of this work which could have the same running time as the direct problem (1 hr. C.P.U.). It would involve inverting

the surface pressure equation (equation 42) to compute the surface geometry which corresponds to a given pressure distribution. This is a direct scheme for computing the inverse (i.e. design) problem and therefore the computational time would be reduced significantly over an iterative technique.

APPENDIX - COEFFICIENTS OF TRANSFORMED EULER EQUATIONS

$$A_1 = w^2 - \gamma T = w^2 - a^2$$

$$A_2 = \theta_z + (\theta_x u + \theta_y v)\, w/A_1$$

$$A_3 = \theta_z + \theta_x u/w + \theta_y v/w$$

$$A_4 = (\theta_x u + \theta_y v)/A_1$$

$$A_5 = \theta_z + (r_x u + r_y v)w/A_1$$

$$A_6 = r_z + r_x u/w + r_y v/w$$

$$A_7 = (r_x u + r_y v)/A_1$$

$$a_{11} = X_{\partial} + X_r A_5 + X_\theta A_2$$

$$a_{12} = X_x \gamma w/A_1$$

$$a_{13} = X_y \gamma w/A_1$$

$$a_{14} = -\gamma(X_r A_7 + X_\theta A_4)$$

$$b_{11} = Y_{\partial} + Y_r A_5 + Y_\theta A_2$$

$$b_{12} = \gamma w Y_x/A_1$$

$$b_{13} = \gamma w Y_y/A_1$$

$$b_{14} = -\gamma(Y_r A_7 + Y_\theta A_4)$$

$$a_{21} = X_x T/w$$

$$a_{22} = X_{\partial} + X_r A_6 + X_\theta A_3$$

REFERENCES

1. Brown, C., McLean, F. and Klunker, E., Theoretical and Experimental Studies of Cambered and Twisted Wings Optimized for Flight at Supersonic Speeds, International Congress of Aero. Sci., Madrid, Spain, 1960.

2. Moretti, G., Grossman, B., and Marconi, F., A Complete Numerical Technique for the Calculation of Three-Dimensional Inviscid Supersonic Flows, AIAA Paper No. 72-192, 1972.

3. Marconi, F., Salas, M. and Yaeger, L., Development of a Computer Code for Calculating the Steady Super/Hypersonic Inviscid Flow around Real Configurations, NASA CR 2675, 1976.

4. Skulsky, R.S., "A Conformal Mapping Method to Predict Low-Speed Aerodynamic Characteristics of Arbitrary Slender Re-Entry Shapes, J. Spacecraft, V3, No. 2, 1966.

5. Moretti, G. and Bleich, G., Three Dimensional Flow Around Blunt Bodies, AIAA J 5, 1966.

6. Sims, J.L., Tables for Supersonic Flow Around Right Circular Cones at Zero Angle of Attack, NASA SP-3004, 1964.

7. Jorgensen, L., Elliptic Cones Alone and with Wings at Supersonic Speeds, NACA TN 1376, 1958.

8. Moretti, G., Three-Dimensional, Supersonic, Steady Flows with any Number of Imbedded Shocks, AIAA Paper No. 74-10, 1974.

9. Moretti, G., Thoughts and Afterthoughts about Shock Computations, PIBAL Report No. 72-37, (1972).

10. Craidon, Charlotte B., A Computer Program for Fitting Smooth Surfaces to an Aircraft Configuration and Other Three-Dimensional Geometries, NASA TM X-3206, June 1975.

11. Jones, D.J., Tables of Inviscid Supersonic Flow about Circular Cones at Incidence, $\gamma = 1.4$, AGARD A6137, 1969.

12. Jones, R.T. and Cohen, D., High Speed Wing Theory, Princeton University Press, 1960.

13. Coons, Steven A., Surfaces for Computer-Aided Design of Space Forms, MAC-TR-41 (Contract No. AF-33 (600)-42859), Massachusetts Inst. Technology, June 1967.

14. Van Dyke, Milton D., "The Slender Elliptic Cone as a Model for Non-linear Supersonic Flow Theory," J. Fluid Mach., Vol. No. 1, 1956.

15. Rogers, E., Quincey, V. and Callinan, J., Experiments at $M = 1.41$ on a Thin Conically Cambered Elliptic Cone of 30° Semi-Vertex Angle, R&M. No. 3306, 1963.

16. Woodward, F., An Improved Method for the Aerodynamic Analysis of Wing-Body-Tail Configurations in Subsonic and Supersonic Flow, NASA CR-2228, 1973.

17. Grossman, B., A Numerical Procedure for the Computation of Supersonic Conical Flows, AIAA Paper No. 78-2114, 1978.

DAT
ILM

Figure 62 Pressure Distributions and Crossflow Shocks at Various Stations
of Fully 3-D Wing, $M_\infty = 1.97$, $\alpha = 10°$

-0.20

R80-1248-056W